HIGH-SPEED BROADBAND NANOMECHANICAL PROPERTY QUANTIFICATION AND IMAGING OF LIFE SCIENCE MATERIALS USING ATOMIC FORCE MICROSCOPE

BY JUAN REN

A dissertation submitted to the

Graduate School—New Brunswick

Rutgers, The State University of New Jersey

in partial fulfillment of the requirements

for the degree of

Doctor of Philosophy

Graduate Program in Physics and Astronomy

Written under the direction of

Prof. Qingze Zou

and approved by

_____

_____

_____

_____

New Brunswick, New Jersey

October, 2015

ABSTRACT OF THE DISSERTATION

HIGH-SPEED BROADBAND NANOMECHANICAL PROPERTY QUANTIFICATION AND IMAGING OF LIFE SCIENCE MATERIALS USING ATOMIC FORCE MICROSCOPE

by JUAN REN

Dissertation Director:

Prof. Qingze Zou

Nanoscale morphological characterization and mechanical properties quantification of soft and biological materials play an important role in areas ranging from nano-composite material synthesis and characterization, cellular mechanics to drug design. Frontier studies in these areas demand the coordination between nanoscale morphological evolution and mechanical behavior variations through simultaneous measurement of these two aspects of properties. Atomic force microscope (AFM) is very promising in achieving such simultaneous measurements at high-speed and broadband owing to its unique capability in applying force stimuli and then, measuring the response at specific locations in a physiologically friendly environment with pico-newton force and nanometer spatial resolution. Challenges, however, arise as current AFM systems are unable to account for the complex and coupled dynamics of the measurement system and probe-sample interaction during high-speed imaging and broadband measurements. In this dissertation, the creation of a set of dynamics and control tools to probe-based high-speed imaging and rapid broadband nanomechanical spectroscopy of soft and biological materials are presented. Firstly, advanced control-based approaches are presented to improve the imaging performance of AFM imaging both in air and in liquid. An adaptive contact mode (ACM)

imaging scheme is proposed to to replace the traditional contact mode (CM) imaging by addressing the major concerns in both the speed and the force exerted to the sample. In this work, the image distortion caused by the topography tracking error is accounted for in the topography quantification and the quantified sample topography is utilized in a gradient-based optimization method to adjust the cantilever deflection set-point for each scanline closely around the minimal level needed for maintaining a stable probe-sample contact, and a data-driven iterative feedforward control that utilizes a prediction of the next-line tracking is implemented to enhance the sample topography tracking. An adaptive multi-loop mode (AMLM) imaging approach is proposed to substantially increase the imaging speed of tapping mode (TM) while preserving the advantages of TM over CM by integrating an inner-outer feedback control loop to regulate the TM-deflection on top of the conventional TM-amplitude feedback control to improve the sample topography tracking. Experiments demonstrated that the proposed ACM and AMLM are capable of increasing the imaging speed by at least 20 times for conventional contact and tapping mode imaging, respectively, with no loss of imaging quality and well controlled tip-sample interaction force. In addition, an adaptive mode imaging for in-liquid topography quantification on live cells is presented. The experiment results demonstrated that instead of keeping constant scanning speed, the proposed speed optimization scheme is able to increase the imaging speed on live human prostate cancer cells by at least eight-fold with no loss of imaging quality. Secondly, control based approaches to accurate nanomechanical quantification on soft materials for both broadband and in-liquid force-curve measurements are proposed to address the adverse effects caused by the system coupling dynamics and the cantilever acceleration, which were not compensated for by the conventional AFM measurement approach. The proposed nanomechanical measurement approaches are demonstrated through experiments to measure the viscoelastic properties of different polymer samples in air and live human cells in liquid to study the variation of rate-dependent elastic modulus of cervix cancer cell during the epithelial-mesenchymal transition process.

DEDICATION

This dissertation is dedicated to my husband Jeffrey Willson, and my parents Wannian Ren and Xiuling Zhang, without whose endless trust, support, encouragement, and love it would not have been possible.

ACKNOWLEDGEMENTS

I would like to express my warmest gratitude to all those who helped me in the completion of this thesis and those who became a big part of my graduate study.

To my advisor, Dr. Qingze Zou, for his guidance, encouragement and his inspiring words to motivate me throughout my graduate study; for his undying support and patience; for his endless encouragement and inspiration which lightened me up towards the right direction.

To my committee members Dr. Jingang Yi, Dr. Liping Liu, and Dr. Nan Gao for their efforts and contributions to this work.

To my friends and colleagues Zhihua Wang, Jiangnbo Liu, Haiming Wang, Zhonghua Xu, and Yan Zhang, for their support, suggestion, and encouragement.

Grateful acknowledgement is to my husband, Jeffrey Willson and my parents, Wannian Ren and Xiuling Zhang, for their endless love, support, and encouragement; for always being there for me.

Table of Contents

List of Tables

List of Figures

Chapter 1

Introduction

Atomic Force microscopy (AFM) has found its unique application in high-speed nanoscale morphological characterization and mechanical properties quantification of soft and biological materials owing to its unique capability in applying force stimuli and then, measuring the response at specific locations in a physiologically friendly environment with pico-newton force and nanometer spatial resolution. Challenges, however, arise as current AFM systems are unable to account for the complex and coupled dynamics of the measurement system and probe-sample interaction during high-speed imaging and broadband measurements.

Probe-based topography imaging using AFM finds its applications in quantitatively measuring nanoscale sample topography of a wide variety of materials [1, 2, 3, 4], ranging from hard materials such as silicon [2] (e.g., contact mode (CM)) to relatively soft materials such as polymers [5, 3, 4] (tapping mode (TM)). However, current AFM imaging approaches are largely limited in both the imaging speed and the magnitude of the probe-sample interaction force. Specifically, high-speed CM-imaging is challenging as the dynamics of the piezoelectric actuator (along with the probe fixture) can be excited as the scanning speed increases, resulting in large positioning error of the probe relative to the sample, particularly when the imaging size is large and the hysteresis effect of the piezo actuator is pronounced [6, 7, 8]. Although efforts in both hardware improvements [1, 9, 7] and software/control algorithms [6, 10, 11] have been proposed to compensate for such dynamics-hysteresis caused probe positioning errors, substantial fluctuation of the cantilever deflection can still exist, resulting in significant image distortions and/or large normal force (exerted to the sample) [6, 7, 12]. Control of the normal force, although crucial, remains as a challenge when imaging at high speed and/or over large size. Although TM-imaging is the de facto most widely used imaging technique of AFM, thanks to its superior image quality and subdued sample distortion when compared

to CM-imaging [13, 14, 3, 4], the rather slow imaging speed has become the major limit and bottleneck of TM-imaging [1, 15]. High-speed TM-imaging is challenging as the increase of imaging speed can quickly lead to loss of probe-sample interaction and/or annihilated of cantilever tapping vibration, particularly when the imaging size is large. Current efforts to increase the speed of TM-imaging [14, 16], however, only lead to rather limited improvements as the speed increase is rather small (around 3 times), and accompanied with a substantial (over 5 times) increase of force applied. Thus, the challenges in and the needs for high-speed AFM imaging motivate the development of the proposed imaging techniques.

In AFM-based nanomechanical quantification, indentation-based approach has been utilized to measure mechanical properties of a wide variety of soft materials at nano scale, ranging from polymers [17, 18, 19, 20], live biomaterials [21, 22, 23] to food product [24]. By measuring the excitation force applied and the indentation generated in the sample, mechanical properties such as the elastic modulus and/or the complex modulus (for viscoelastic materials) of the sample can be quantified (through a contact model of the probe-sample interaction, e.g., the Hertzian model or the DMT model) [21, 1, 25]. As the force and the indentation serve as the input and output in the contact model, respectively, accuracy of the indentation quantification dictates that of the nanomechanical properties measured. Therefore, accurate indentation measurement is crucial to nanomechanical property measurement of materials.

However, the conventional indentation measurement is limited and erroneous in broadband and in-liquid nanomechanical property quantification. Currently on almost all commercial AFM systems, the indentation is obtained by comparing the force-distance curves [1] measured on the soft sample and that on a hard reference sample under a constant force load-unload rate [1, 26]. This method (to quantify the indentation) is adequate when the measurement is quasi static (with constant force load/unload rate) and the load/unload rate is low—so that the AFM instrument dynamics is not excited and the cantilever base displacement (i.e., the cantilever displacement at its fixed end) equals to the z-axis piezo actuator displacement (measured by the z-axis sensor). As the measurement load/unload rate increases towards the resonances of the AFM instrument dynamics, the dynamics of the cantilever fixture (connecting the cantilever to the piezo actuator) can be excited [1], and the lateral-vertical cross-axis dynamics coupling effect becomes pronounced [27, 28]. Consequently, large measurement errors are induced when

using the z-axis sensor to directly measure the cantilever base displacement, as the cantilever-base displacement is largely different from the z-axis sensor signal, and the cross-axis coupling dynamics induces extraneous motion of the cantilever in z-axis. For measurements in liquid, although the instrumental dynamics is not an issue, the relative acceleration of the cantilever probe (with respect to the fixed-end of the cantilever (called the *the relative probe acceleration*) becomes pronounced and substantially effects the indentation generated. The conventional indentation is also plagued by the uncertainty in determining the probe-sample contact point [29] and the hydrodynamic force effect [30, 31]. Although the contact-point uncertainty can be alleviated through the use of a reference sample [1], and the hydrodynamic force effect might be accounted for by quantifying it via experiment [31], these efforts are still limited to ultra-low force load rate, and the relative probe acceleration dominates over the hydrodynamic force (i.e., over an order of magnitude larger) when the force load rate is higher than $\sim$0.1 Hz for for most live cells. Therefore, techniques need to be developed to accurately measure the indentation to achieve rapid, broadband and in liquid nanomechanical properties quantification.

To address the issues discussed above in high-speed sample topography quantification and material nanomechanical property measurement, a suite of control based approaches are presented for improving the performance of high-speed AFM topography imaging and high-speed nanomechanical quantification using AFM, especially for soft and biological materials. The rest of this dissertation proposal is organized as follows.

In Chapter 2, an adaptive contact-mode (ACM) imaging approach is proposed to replace the traditional contact-mode imaging by addressing the major concerns in both the speed and the force exerted to the sample. The proposed approach substantially increases the CM-imaging speed, and maintains a near minimal interaction force. The improvements arise from the following three ingredients: (i) The sample topography is quantified using both the AFM z-axis piezo displacement and the cantilever deflection as opposed to using only the piezo displacement in the conventional CM-imaging; (ii) The deflection set-point is adjusted line-by-line closely around the minimal level needed for maintaining a stable probe-sample contact, as opposed to being *fixed* during the entire imaging process in the conventional CM-imaging; and (iii) The sample topography quantified in (i) is utilized in an iterative feedforward control scheme to track the sample topography as opposed to solely relying on the cantilever deflection in the

conventional CM-imaging. The ACM approach is demonstrated and evaluated by implementing it to image a calibration sample of square pitches at both high speeds (e.g., scan rate of 75 Hz and 130 Hz) and large sizes (e.g., scan size of 30 μm and 80 μm). The experimental results show that compared to the traditional constant-force contact-mode imaging, the imaging speed can be increased by over 30 folds (with the scanning speed reached 13 mm/sec.), and the probe-sample interaction force can be reduced by more than 15% while maintaining the same image quality.

In Chapter 3, an imaging mode (called the *adaptive multi-loop mode*) of AFM is proposed to substantially increase the speed of tapping mode (TM) imaging while preserving its advantages over CM-imaging. The proposed approach aims to not only substantially increase the TM-imaging speed without loss of image quality, but also maintain the probe tapping closely around the set-point and the tip-sample interaction force around the minimal (needed for maintaining a stable tapping) throughout the imaging process. Such an improvement in both the imaging speed and the interaction force control is achieved through the development of an adaptive multi-loop mode (AMLM) imaging scheme that regulates both the tapping amplitude and the mean cantilever deflection (called the *TM-deflection* later). Specifically, the proposed AMLM-imaging is composed of the following three ingredients: (i) Unlike the conventional TM-imaging that completely ignores the TM-deflection variation, it is proposed to take the variation of the cantilever TM-deflection into account when quantifying the sample topography. (ii) Unlike TM-imaging that only regulates the tapping-amplitude via the RMS-amplitude feedback control, the proposed AMLM-imaging explores an inner-outer feedback control loop to regulate the TM-deflection on top of the RMS-amplitude feedback. (iii) A data-driven online iterative feedforward controller is augmented to overcome the time-delay of the RMS-amplitude feedback loop, where the next-line sample topography and tracking error are predicted and utilized to further improve the topography tracking. The proposed AMLM-imaging is tested and demonstrated through imaging a poly(tert-butyl acrylate) sample in experiments.

In Chapter 4, we propose an adaptive mode of in-liquid topography imaging (AML) on live cells with scanning speed optimization in order to increase the scanning speed on live cells with minimum loss of imaging quality and minimized tip-sample interaction force. The improvements arise from the following four folds: (i) The imaging speed is optimized online based

on real-time estimation of the sample deformation, the tip-sample interaction force, as well as the sample topography variation rate, as opposed to being fixed during the entire imaging process in the conventional AFM imaging; (ii) The sample topography is quantified using both the AFM z-axis piezo placement and the cantilever deflection as opposed to using only the piezo displacement in the conventional CM imaging; (iii) The sample topography quantified in (ii) is utilized in an iterative feedforward control scheme to track the sample surface as opposed to solely relying on the cantilever deflection in the conventional CM imaging; (iv) The deflection set-point is adjusted line-by-line closely around the minimal level needed for maintaining a stable tip-sample interaction as opposed to being fixed during the entire imaging process in the conventional AFM CM imaging. The proposed AML technique was experimentally validated through imaging live human prostate cancer (PC-3) cells at the average scan rates of 0.41 Hz and 0.86 Hz. Compare to the conventional CM imaging, the AML technique was able to increase the imaging speed over four times while preserving the topography details of the live cells by accurate tracking of the sample topography.

In Chapter 5, control based approaches to achieve accurate nanomechanical property measurements on soft materials are proposed. Specifically, in Chapter 5.2, a control-based approach to accurately quantify the nanoindentation in broadband nanomechanical property measurements using AFM is proposed. First, based on the analysis of the adverse effects of the cantilever-fixture dynamics and the lateral-vertical cross-axis coupling dynamics, an approach to individually quantify these two adverse effects through experiments is proposed. Secondly, the cantilever dynamics during the broadband nanomechanical quantification is modeled and analyzed by taking into account the relationships between the measurement frequency range and the bandwidth of both the piezo actuator and the cantilever. Using the cantilever dynamics model, it is proposed to measure the indentation by accurately tracking the *same* broadband excitation force profile (i.e., the same cantilever vertical deflection) on the soft sample and on a hard reference sample, and obtaining the indentation from the difference of the cantilever base displacements obtained on both samples. Control techniques such as the recently developed modeling-free inversion-based iterative control (MIIC) technique [32] is utilized to quantify

both the cantilever-fixture dynamics and the cross-axis coupling dynamics, and to achieve accurate tracking of the excitation force of rich frequency spectrum. The proposed method is illustrated by implementing it to the broadband viscoelasticity measurement of a several polymer samples in experiment. In Chapter 5.3, a control-based approach to replace the conventional method to achieve accurate indentation quantification is proposed for nanomechanical measurement of live cell using AFM. Particularly, the cantilever dynamics during the force–indentation measurement is analyzed by taking into account both the cantilever–probe interaction and the measurement frequency range. Based on the analysis, it is proposed to track the *same* excitation force profile (i.e., the same cantilever deflection) on both the soft sample (e.g., the live cell) and a hard reference, and then quantify the indentation from the displacement difference of the cantilever base on the cell with respect to that on the hard reference. The proposed approach is then employed to study the rate–dependent elastic modulus of HeLa cell before and after the nutrient–deprivation process, with comparison to those of fibroblast cell.

Our conclusions are presented in Chapter 6.

Chapter 2

High-Speed Adaptive Contact-Mode Atomic Force Microscopy Imaging with Near-Minimum-Force

Abstract

In this chapter, an adaptive contact-mode imaging approach is proposed to replace the traditional contact-mode imaging by addressing the major concerns in both the speed and the force exerted to the sample. The speed of the traditional contact-mode imaging is largely limited by the need to maintain precision tracking of the sample topography over the entire imaged sample surface, and large image distortion and excessive probe-sample interaction force occur during high-speed imaging. In this work, first, the image distortion caused by the topography tracking error is accounted for in the topography quantification. Secondly, the quantified sample topography is utilized in a gradient-based optimization method to adjust the cantilever deflection set-point for each scanline closely around the minimal level needed for maintaining a stable probe-sample contact, and a data-driven iterative feedforward control that utilizes a prediction of the next-line tracking is integrated to the topography feeedback loop to enhance the sample topography tracking. The proposed approach is demonstrated and evaluated by implementing it to image a calibration sample of square pitches at both high speeds (e.g., scan rate of 75 Hz and 130 Hz) and large sizes (e.g., scan size of 30 μm and 80 μm). The experimental results show that compared to the traditional constant-force contact-mode imaging, the imaging speed can be increased by over 30 folds (with the scanning speed reached 13 mm/sec.), and the probe-sample interaction force can be reduced by more than 15% while maintaining the same image quality.

2.1 Introduction

In this chapter, we present an approach that addresses major concerns in large-size (e.g., lateral scan size over 25 μm) contact-mode imaging using atomic force microscope (AFM) in both the speed and the force exerted to the sample. Contact-mode (CM) imaging finds its applications in quantitatively measuring nanoscale sample topography of a wide variety of materials [1, 2], ranging from hard materials such as silicon [2] to relatively soft materials such as polymers [5, 33, 34]. Current CM-imaging, however, is largely limited in both the imaging speed and the magnitude of the normal force (i.e, the probe-sample interaction force). High-speed CM-imaging is challenging as the dynamics of the piezoelectric actuator (along with the probe fixture) can be excited as the scanning speed increases, resulting in large positioning error of the probe relative to the sample, particularly when the imaging size is large and the hysteresis effect of the piezo actuator is pronounced [6, 7, 8]. Although efforts in both hardware improvements [1, 9, 7] and software/control algorithms [6, 10, 11] have been proposed to compensate for such dynamics-hysteresis caused probe positioning errors, substantial fluctuation of the cantilever deflection can still exist, resulting in significant image distortions and/or large normal force (exerted to the sample) [6, 7, 12]. Control of the normal force, although crucial, remains as a challenge when imaging at high speed and/or over large size. The proposed approach aims to achieve large-size, high speed CM-imaging while keeping the normal force around the minimal level (for maintaining a stable probe-sample interaction).

The speed of constant-force CM (CF-CM) imaging mode [1, 2, 35]—the most commonly used CM-imaging—is constrained by the increasingly stringent precision positioning of the probe relative to the sample as the imaging speed increases. In CF-CM imaging, the x-y-z 3D positioning of the probe relative to the sample is needed to maintain the normal force at the set-point value so that the sample topography can be measured as the z-axis piezo displacement at each sample point [1, 2]. As the scanning speed and the imaging size increase, the dynamics and the hysteresis effect of the piezo actuators can be excited [36, 37, 8], resulting in large probe-sample positioning error—the sample topography cannot be measured as the displacement of the z-piezo actuator anymore. The imaging speed can be increased by using high bandwidth piezo actuators [38, 39]. The samples that can be imaged, however, are rather

small (< 5 μm [38, 39]) and flat (sample height < 50 nm). Imaging of large-size samples can be improved through the development of control techniques to compensate for the dynamics and the hysteresis effects of the piezo actuators [11, 40, 10] along with hardware improvements [41, 42]. However, the imaging speed increase is still rather limited due to the challenge in the vertical z-axis positioning of the probe with respect to the sample, as the sample topography profile, in general, is unknown and may contain large and rapid variations (e.g., the calibration sample of square pitches), thereby, is difficult to be tracked during high-speed imaging. As a result, substantial error in the vertical probe-sample positioning persists. Moreover, cross-axis dynamics coupling effect [2, 43, 44] exists and can induce extraneous vertical positioning error of the probe during large-size imaging. Such probe positioning errors translate directly to image distortions in CF-CM imaging. Therefore, techniques need to be developed to achieve high-speed, large-size CM imaging.

The imaging speed might be substantially increased through the developments in constant-height CM (CH-CM) imaging [45, 46, 43]. CH-CM imaging, however, is not preferred in applications due to the lack of force control. In CH-CM imaging, the sample topography is quantified from the cantilever deflection by keeping the position of the z-axis piezo actuator (instead of the cantilever probe) around a pre-chosen set-point value [45, 46, 47]. Unlike CF-CM imaging, the probe positioning in CH-CM is rather simplified as only lateral tracking of the probe during the scanning is needed. Lateral tracking control of the probe is much easier than z-axis tracking of the sample topography as the scanning trajectory is known a priori. Approaches such as the iterative learning control techniques [11, 32] have been developed recently that can account for both the dynamics and the hysteresis effects of the piezo actuators in high-speed, large-range scanning. Alternatively, excitation of the dynamics effect of the piezo actuator can be avoided through the design of scanning patterns [47]. However, as the normal force is *not controlled*, such a speed increase in CH-CM imaging is obtained at the cost of substantial increase of the force applied, resulting in severe sample and/or probe damages. These constraints largely limit the application of the high-speed CH-CM imaging.

The proposed approach substantially increases the CM-imaging speed, and maintains a near minimal interaction force. The improvements arise from the following three ingredients: (i) The sample topography is quantified using both the AFM z-axis piezo displacement and

the cantilever deflection as opposed to using only the piezo displacement in the conventional CM-imaging; (ii) The deflection set-point is adjusted line-by-line closely around the minimal level needed for maintaining a stable probe-sample contact, as opposed to being *fixed* during the entire imaging process in the conventional CM-imaging; and (iii) The sample topography quantified in (i) is utilized in an iterative feedforward control scheme to track the sample topography as opposed to solely relying on the cantilever deflection in the conventional CM-imaging.

The proposed ACM imaging systematically integrates the above three innovations together. To compute the sample topography accurately, both the cantilever behavior and the probe-sample interaction condition during the CM-imaging are accounted for even when there exists large sample profile tracking error (i.e., large fluctuation of the cantilever deflection). Then a gradient-based optimization is employed to minimize the force set-point. Finally, the sample topography is tracked through direct control of the z-axis piezo via a data-driven iterative feedforward control [32], thereby, the time-delay in tracking the sample topography (when only using the cantilever deflection feedback) is largely avoided. The experimental implementation of the proposed approach in imaging a calibration sample of square pitches (pitch height: 18 μm, pitch size: 10 μm by 10 μm) at both high speeds (75 Hz and 130 Hz) and large sizes (30 μm and 80 μm) demonstrated that compared to the CF-CM imaging, the proposed ACM imaging not only increased the imaging speed by over 30 folds (reached 13 mm/sec), but also reduced the maximum and the RMS amplitude of the interaction force by 23% and 30%, respectively. Therefore, the proposed ACM approach substantially improves over the CF-CM imaging in both the imaging speed and the interaction force control.

The remainder of this chapter is organized as follows. In Sec. 2.2, the proposed sample topography quantification is introduced and employed to reveal the drawbacks of the CF-CM imaging, followed by the presentation of the proposed ACM technique in Sec. III. The experimental implementation of the proposed ACM is described and discussed through comparison to the conventional CF-CM imaging in Sec. 2.4. Our conclusions are given in Sec. 2.5.

2.2 Accurate Sample Topography Estimation during AFM Contact-Mode Imaging

The proposed ACM approach is based on accurate estimation/quantification of the sample topography profile during the imaging process. We start by assuming that during the CM-imaging process:

Assumption 1 *The vibration modes of the cantilever are not excited;*

Assumption 2 *A continuous tip-sample contact is maintained in the repulsive region;*

Assumption 3 *The sample deformation (indentation) is negligible.*

Assumption 1 is reasonable as during the CM-imaging, the power spectrum of the AFM probe motion mostly resides in the frequency region several times lower than the first resonant frequency of the cantilever, e.g, even at the scanning rate of 150 Hz over a large scan size (e.g., 50 μm), the power spectrum of the cantilever motion is still concentrated in the frequency range 100 times lower than the first resonance of the cantilever usually used in CM-imaging. Excitation of the probe vibration is further avoided in the proposed ACM imaging by tracking the true sample topography accurately, even at high speeds. Assumption 2 also holds as the cantilever deflection is maintained around the set-point during the scanning by a feedback controller (see Fig. 2.1), and consequently, the probe-sample interaction force in the vertical direction (called the *normal force* below) is dominated by the repulsive electrostatic force, i.e., the repulsive normal force is proportional to the AFM cantilever deflection [1, 48],

$$F_z(t) = -k_c d(t), \tag{2.1}$$

where k_c and $d(t)$ are the spring constant of the cantilever and the cantilever deflection, respectively. Finally, Assumption 3 holds as large sample deformation directly results in not only imaging distortion, but also sample modification or damage, and probe contamination and/or wear [1, 49].

Current method to estimate/quantify the sample topography in CM-imaging becomes erroneous as the imaging speed increases. During the traditional CF-CM imaging, a feedback

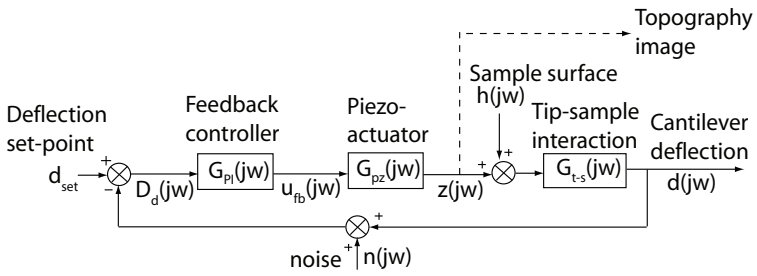

Figure 2.1: Schematic block diagram of the conventional CF-CM imaging, where $u_{fb}(j\omega)$ and $z(j\omega)$ denote the control input and the corresponding output (i.e., displacement) of the piezo actuator, respectively.

controller, as schematically depicted in Fig. 1, is employed to drive the piezoelectric actuator (called the z**-piezo** in the rest of this chapter) to maintain the cantilever deflection around the set-point, d_{set}, and the sample surface topography is quantified as the z-piezo displacement. Such a quantification, however, is only adequate when the scanning speed is slow enough [11, 40, 7]. At high scanning speed the low quality height images are accompanied with large deflection variations (i.e., dramatic deflection errors). Advanced control techniques [11, 40] have been proposed to increase the scan rate and mitigate the deflection variation during the scanning. The scan rate improvement achieved, however, is rather limited, and large deflection variation still persists during high-speed imaging [11, 40].

To be more concrete, consider the tip-sample interaction during CM-imaging at two different locations on the sample surface, point (x_0, y_0) and point (x_1, y_1), as shown in Fig. 2.2, and the z-piezo positions and the cantilever deflections at these two points as $z(x_0,\ y_0)$ and $z(x_1,\ y_1)$, and $d(x_0,\ y_0)$ and $d(x_1,\ y_1)$, respectively. Assumptions 2 and 3 imply that the height difference between these two points is given by

$$h_{1-0} = [z(x_1, y_1) - z(x_0, y_0)] + [d(x_1, y_1) - d(x_0, y_0)]. \tag{2.2}$$

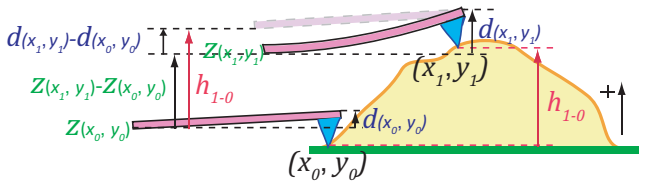

Figure 2.2: Height difference between two sample locations during AFM contact-mode imaging.

Thus, the above Eq. (2.2) implies that the variation of the sample topography of the entire imaged sample surface can be obtained with respect to one fixed reference point—point 0 (e.g., the first sample point imaged—for convenience). Without loss of generality, the height datum point 0 can be set as $z(x_0, y_0) = 0$ and $d(x_0, y_0) = d_{\text{set}}$. Thus, the sample surface topography can be quantified as

$$h(x, y) = z(x, y) + [d(x, y) - d_{\text{set}}]. \tag{2.3}$$

The above Eq. (2.3) clearly reveals the limit of and the errors introduced in the conventional CM-imaging. At slow imaging speeds, the cantilever probe can accurately track the sample topography when the feedback control system is fast enough, i.e., the cantilever deflection fluctuation is small enough, and hence, the sample topography can be adequately quantified as the z-piezo displacement measured at each sample point—the conventional CF-CM imaging, i.e., as $d(x, y) \approx d_{\text{set}}$, $h(x, y) \approx z(x, y)$ in Eq. (2.3). However, as the imaging speed increases it is challenging to maintain such a stringent condition ($d(x, y) \approx d_{\text{set}}$), especially upon samples with dramatic topography features (e.g., the calibration sample of large square pitches employed in this work). For those samples, large fluctuations ("spikes") of the cantilever deflection are inevitable and the amplitude of the "spikes" increases with the scan rate, as the topography features act as step (force) inputs to the cantilever probe and the cantilever dynamics is rather lightly damped (with damping coefficient $\xi \approx 0.002$ [50, 51]). For example, for the calibration sample employed in this work, the cantilever deflection error becomes not negligible (i.e., larger than the thermal-fluctuation of the cantilever) when the scan rate increases to merely 5 Hz when using the CF-CM imaging (with a carefully-tuned PI controller). Therefore, the conventional sample topography estimation of the CF-CM imaging substantially limits the imaging speed.

Similar idea of utilizing the cantilever deflection to improve the topography quantification has also been recently explored [52]. However, no systematic analysis is discussed [52]. Moreover, even though the imaging speed can be improved by using Eq. (2.3), such a modification does not improve the control of the normal force, thereby, is rather limited for high-speed imaging —It is crucial to control the normal force during high-speed CM-imaging.

2.3 Adaptive Contact-Mode Imaging with Near-minimum Force

The above sample topography quantification (Eq. (2.3)) is utilized to develop the proposed ACM imaging.

2.3.1 Gradient-based Minimization of the Normal Force

We first show that the normal force can be reduced by allowing the deflection set-point to vary during the imaging–The proposed topography quantification (Eq. (2.3)) implies that the deflection set-point does not need to be *fixed* during the imaging process! With cantilever deflection set-point being fixed, the conventional CM-imaging has little room to reduce the normal force—at best the normal force is at the *a priori* chosen set-point, which might be too large or too small, and not optimal for the sample to be imaged and the chosen imaging conditions (e.g., the chosen scanning speed and imaging size), particularly when the sample properties are unknown. Moreover, when the same deflection set-point is used throughout the entire imaging process, the force applied may be exceedingly large for areas where the sample is relatively flat and the topography variation is small, whereas not large enough to maintain the image quality at areas where the sample topography variation is large. Thus, the use of a fixed force set-point limits the optimization of CM-imaging.

As depicted in Fig. 2.3, we propose a gradient-based optimization scheme to adaptively adjust the deflection set-point line-by-line. Specifically, the deflection set-point of the $k+1^{th}$

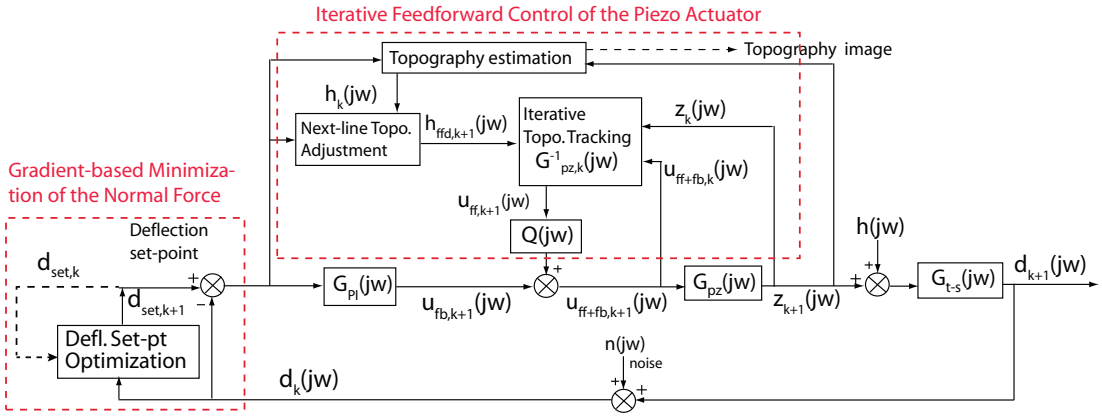

Figure 2.3: Schematic block diagram of the proposed adaptive contact-mode.

scanline, $d_{\text{set,k+1}}$, is updated/adjusted from that of the previous line, $d_{\text{set,k}}$, by using the difference between minimum of the predicted deflection at the $k+1^{th}$ scanline, $\min(\hat{d}_{k+1}(t))$, and the minimum deflection/force needed to maintain the stable repulsive tip-sample interaction, D^*_{min} (i.e., the threshold value),

$$\begin{aligned} d_{\text{set,0}} &= d_{\text{set,org}}, \\ d_{\text{set,k+1}} &= d_{\text{set,k}} - [\min(\hat{d}_{\text{k+1}}(t)) - D^*_{\text{min}}], \quad k \geq 1 \\ \text{with} \quad \hat{d}_{\text{k+1}}(t) &\triangleq d_{\text{k}}(t) + \rho[(d_{\text{k}}(t) - d_{\text{k-1}}(t))], \quad \text{for} \quad t \in [0,\ T_{\text{scan}}], \end{aligned} \tag{2.4}$$

where T_{scan} is the scanning period, $d_{\text{set,org}}$ is the original deflection set-point chosen *a priori* to the imaging process, and $\rho \in [0, 1]$ is the gradient factor, and sand can be tuned to improve the imaging quality. As shown in Eq. (2.4), the line-to-line topography variation is accounted for in the predicted next-line deflection, $\hat{d}_{\text{k+1}}(\cdot)$ using the topography gradient , and then utilized to adjust the deflection set-point for the next scan line, $d_{\text{set,k+1}}$, i.e., the current-line deflection set-point ($d_{\text{set,k}}$) is adjusted such that $d_{\text{set,k+1}}$ will ensure that the deflection on the next-line will be above the required minimal deflection level across the entire scan line (through the use of the minimal value of the predicted next-line deflection, $\min(\hat{d}_{k+1}(t))$). Precision tracking of the sample topography by the proposed iterative feedforward control scheme next ensures that the line-to-line deflection variation, $d_k(t) - d_{k-1}(t)$, is rather small. Therefore, the normal force is maintained around the minimal level D^*_{min} throughout the entire imaging process, arriving at the near-minimum-force scan.

Moreover, to avoid the transient response of the cantilever due to the potential sudden jump of the deflection set-point, the deflection set-point is smoothly transited over a few sample instants from the previous-line set-point value to the optimal value obtained from Eq. (2.4) through, for example, a filtered ramp trajectory over (more advanced control techniques like the optimal tracking-transition technique [53] can be utilized for generating the smooth transition trajectory).

Note that the sample surface topography image is obtained according to Eq. (2.3)—the line-to-line update of the deflection set-point doesn't affect the quantified sample topography by choosing a universal height datum for the entire image, e.g., $d_{\text{set}} = d_{\text{set,org}}$ in Eq. (2.3), as the change of the deflection set-point is canceled.

2.3.2 True-Topography Tracking via Iterative Feedforward Control of the Piezo Actuator

Next, an online iterative feedforward control approach is integrated to the sample topography tracking system to enhance the sample topography tracking performance by: (i) estimating both the sample topography profile and the profile tracking error at the next scan line, and (ii) using the estimation to control the z-axis piezo actuator in the sample topography tracking.

First, at the end of the k^{th} line scanning, the sample topography profile of this line, $h_{\mathrm{k}}(t)$, is quantified via Eq. (2.3) and then used to approximate the profile of the $k + 1^{th}$ line, i.e., $h_{\mathrm{k+1}}(t) \approx h_{\mathrm{k}}(t)$. Such an approximation is reasonable as with enough scanlines, the line-to-line topography variations are small. To further reduce the amplitude of the normal force on samples of large and sudden topography changes, the estimated next-line topography profile is modified by using the k^{th} line deflection error as

$$h_{\mathrm{ffd,k+1}}(t) = h_{\mathrm{k}}(t) + \alpha[d_{\mathrm{k}}(t) - d_{\mathrm{set,k}}], \quad \text{for} \quad t \in [0,\ T_{\mathrm{scan}}], \tag{2.5}$$

where α is the correction factor. Due to the compliance of the cantilever and the cantilever fixture (connecting the cantilever to the piezo actuator), time delay exists in the response of the cantilever deflection to the sample topography change. As the scanning speed increases, such a time delay, albeit small, becomes more crucial and as a result, the sample-topography-caused spikes (in the cantilever's response– deflection) reach their (local) peaks *after* the probe already passes those locations. Even with advanced feedback control, such deflection spikes still exist [43, 11]. The above modified desired trajectory—for the feedforward control input to track—helps the z-piezo to drive the cantilever to respond in advance (i.e., pre-actuate) to the topography variation, thereby reducing the amplitude of the deflection spikes. The correction factor α can be tuned based on the estimated height of the sample surface features.

Next, we propose to track the modified next-line sample topography profile, $h_{\mathrm{ffd,k+1}}(t)$, using a data-driven iterative feedforward control augmented to the z-axis feedback control (see Fig. 2.3). Particularly, the feedforward control input is obtained by implementing the following

modeling-free inversion-based iterative learning control (MIIC) technique [32] online,

$$\begin{aligned} U_{\text{ff,0}}(j\omega) &= 0, \\ U_{\text{ff,k+1}}(j\omega) &= \frac{U_{\text{ff+fb,k}}(j\omega)}{Z_{\text{k}}(j\omega)} H_{\text{ffd,k+1}}(j\omega), \end{aligned} \tag{2.6}$$

where '$j\omega$' denotes the Fourier transform of the corresponding signal, $U_{\text{ff+fb,k}}(\cdot)$ and $Z_{\text{k}}(\cdot)$ are the total control input (feedback+feedforward) applied to the z-piezo actuator (i.e., $U_{\text{ff+fb,k}}(j\omega) = U_{\text{ff,k}}(j\omega) + U_{\text{fb,k}}(j\omega)$, see Fig. 2.3), and the z-piezo displacement measured on the k^{th} scan line, respectively. Note that the ratio in the above control law, $U_{\text{ff+fb,k}}(j\omega)/Z_{\text{k}}(j\omega)$, essentially equals the inverse of the frequency response of the z-piezo actuator (shown as $G_{pz,k}(j\omega)$ in Fig. 2.3), and are updated line-by-line iteratively throughout the whole imaging process. Such a data-driven online-updated inverse is preferred over a priori obtained fixed model in the iterative scheme [9, 37] for better robustness and tracking performance [32]. Then the feedforward output in the time domain, $u_{\text{ff+fb,k+1}}(t)$, is obtained via the inverse Fourier transform and applied during the $k + 1^{th}$ line scanning.

At the beginning of the imaging process, the above iterative scheme is applied to scan the first line repetitively until the convergence is reached (i.e., in practices until the difference of the z-piezo displacement between two consecutive iterations is small enough, e.g., close to the noise level), and then the converged input is used as the initial input for the iteration on the next scanline. Provided that the convergence of the iterative control input is faster than the line-to-line sample topography variation, then the iterative control input for each new scan line only needs to be updated once, i.e., the rest of the sample can be imaged without repetitive scanning! Similar idea of repeating on the first line and then updating the control input using the preceding-line input has been explored recently in Ref. [11], where the amount of allowed line-to-line sample topography variation has been quantified. However, unlike the work in Ref. [11, 34], we propose here to use the measured data to update the dynamics model along with the iteration, and more importantly, use the frequency response of the z-axis piezo actuator itself—instead of the closed-loop dynamics attenuated by the closed-loop sensitivity [54, 11]—when computing the iterative control input. The use of the z-piezo dynamics itself provides a larger "working" bandwidth—thereby better tracking performance at high-speed—the feedback controller tends to reduce the open-loop bandwidth. Such an improvement is demonstrated in our

experiment implementation (See Sec. IV later).

Finally, to avoid the noise being fed into the closed-loop via the feedforward channel and then amplified, the feedforward control input, $U_{\text{ff,k+1}}(\cdot)$, is passed through a zero-phase low-pass filter $Q(j\omega)$,

$$\hat{U}_{\text{ff,k+1}}(j\omega) = Q(j\omega)U_{\text{ff,k+1}}(j\omega) = Q_b(j\omega)C_{\text{lead}}(j\omega)U_{\text{ff,k+1}}(j\omega), \tag{2.7}$$

where $Q_b(j\omega)$ and $C_{\text{lead}}(j\omega)$ are a low-pass filter and a phase-lead compensator, respectively. As the entire next-line feedforward control input is known a priori, the above noncausal zero-phase filter can be implemented online.

2.4 Experimental Demonstration and Evaluation of the ACM

The experiment is to validate and demonstrate that by using the ACM technique, the imaging speed is substantially increased in large-size (e.g., 50 μm and 80 μm) imaging while the normal force is minimized.

2.4.1 Experimental implementation

The experiments were conducted on a commercial AFM (Dimension Icon, Bruker AXS Inc.) with direct access to the drive of the piezo actuators, the cantilever deflection and the piezo displacement. All of the signals were acquired through a data acquisition system under the Matlab xPC-target environment. A calibration sample with nominal pitch size of 10 μm and step height of $\sim$180 nm was used in all of the imaging processes. As the first resonant frequency of the cantilever used (cantilever type: DNP-10, Bruker AXS Inc.) (over 60 kHz) was over 300 times higher than the scan rate ($\leq$ 200 Hz) tested in the experiment, and calibration sample used is made of silicon, Assumptions 1-3 held.

The experimental results and discussion presented below are to validate and demonstrate the three major components of the proposed ACM approach in the order of these components in Sec. II: First, the proposed method of topography quantification (Eq. (2.3)) was validated by comparing the topography image obtained by Eq. (2.3) using the data measured under the conventional CF-CM imaging at a relatively high speed with that obtained at low speed. Secondly, to validate and evaluate the proposed line-by-line adjustment of the cantilever deflection

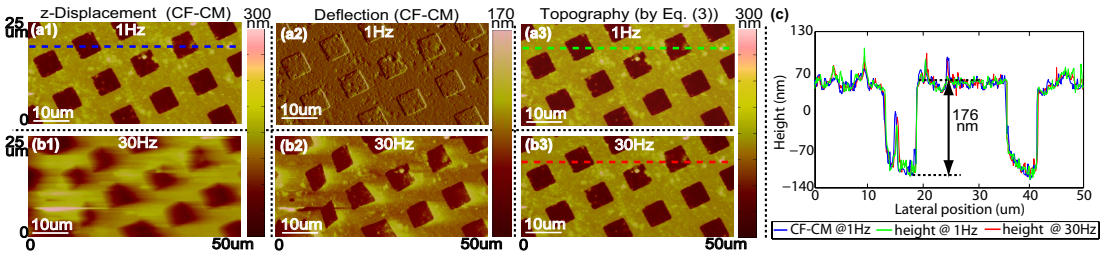

Figure 2.4: Sample topography images (scan area: 50 μm $\times$ 25 μm, scan direction: 50 μm) obtained by using the conventional CM-imaging at the scan rate of (a1) 1 Hz and (b1) 30 Hz; The corresponding cantilever deflection error, $d(x, y) - d_{\text{set}}$, measured at (a2) 1 Hz and (b2) 30 Hz; The sample true topography computed using Eq. (2.3) at (a3) 1 Hz and (b3) 30 Hz; And (c) comparison of the cross-sections at the same scan line on the three images as marked out in images (a1), (a3) and (b3).

set-point in maintaining a near-minimal normal force, and the proposed iterative feedforward control scheme in tracking the sample topography, the normal force and the sample topography tracking results obtained using the ACM imaging at high speeds and large imaging sizes were compared to those obtained by using the CF-CM imaging at much lower speeds. The efficacy of the use of the modified topography in reducing the cantilever deflection fluctuation was also examined. Finally, the sample topography images were compared.

Throughout the imaging experiments, the MIIC technique was employed to achieve precise positioning in the lateral x-y axes scanning [32]. The lateral tracking error was maintained below 1% during all imaging processes. Moreover, the cross-axis dynamics coupling (mainly the coupling from the lateral x-y axes to the vertical z-axis [55]) was compensated for by subtracting it from the z-piezo displacement measured during the imaging processes. Therefore, the differences in the topography tracking, the normal force amplitude, and the image quality presented below reflected the effects of the proposed sample topography quantification and the proposed ACM imaging approach.

2.4.2 Accurate sample topography quantification

The experimental results to validate the proposed sample topography quantification (Eq. (2.3)) are presented in Fig. 2.4 for the scan rates of 1 Hz and 30 Hz and the imaging area of 50 μm $\times$ 25 μm. The z-piezo displacement images (i.e., the sample "topography" obtained in the CF-CM), the cantilever deflection error, and the sample topography images quantified by using

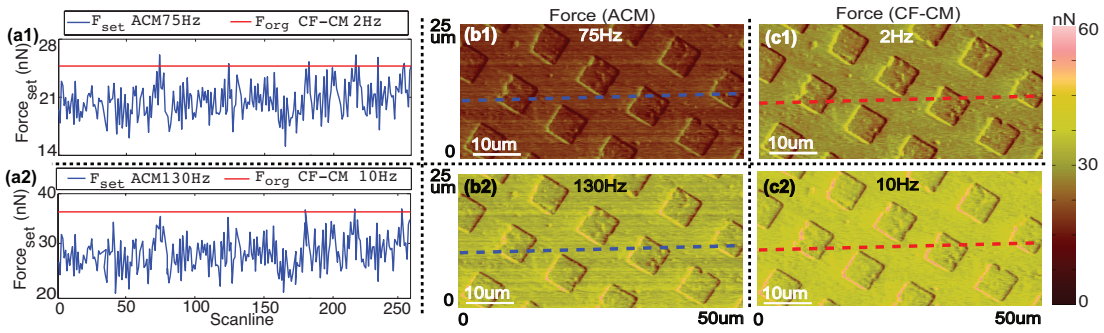

Figure 2.5: The force (i.e., deflection) set-point vs. scanlines adjusted by the proposed gradient-based minimization method in the proposed ACM approach at the scan rate of (a1) 75 Hz and 130 Hz, compared to the fixed a priori chosen set-point used in the CF-CM imaging at the scan rate of (a1) 2 Hz and (a2) 10 Hz, respectively; And (b1, c1, b2, c2) the comparison of the images of the corresponding normal force measured by using these two methods at these four scan rates.

Eq. (2.3) are compared in Fig. 2.4 (a1), (a2), and (a3) for the scan rate of 1 Hz, respectively, and Fig. 4 (b1), (b2), and (b3) for 30 Hz, respectively. At the low imaging speed (1 Hz), the sample topography can be adequately quantified by using the conventional CF-CM imaging, i.e., by using the z-piezo displacement (see Fig. 2.4 (a1)). The RMS-difference between the CF-CM image (Fig. 2.4(a1)) and the quantified topography image (Fig. 2.4 (a3)) was only $\sim$6%. As the imaging speed increased to 30 Hz, however, the sample topography could not be accurately tracked by the z-axis feedback control, the sample with square-pitches of large height acted as an input with repeated large amplitude steps to the z-axis feedback loop, thereby, challenging to be tracked. As a result, the image generated was significantly distorted (Fig. 2.4 (b1)). By using the proposed topography quantification (Eq. (2.3)), however, the image quality was restored, as shown in Fig. 2.4 (b3). The RMS-difference between the low speed and the high speed images was less than 10% (compare Fig. 2.4 (a3) with Fig. 2.4 (b3)). We also observed that the image quality can be largely restored even when the scan rate was increased to 100 Hz, however, at the price of dramatically increased normal force (over 6 times of that in 1 Hz imaging). Therefore, the experimental results demonstrated that the sample topography profile in the CM-imaging can be accurately quantified by using the proposed method (Eq. (2.3)). Moreover, the substantial increase of the force applied during the imaging (over 5 times from 1 Hz to 30 Hz) clearly manifested the limits of the conventional CM-imaging, including those high-speed CH-CM imaging techniques [43, 56, 47].

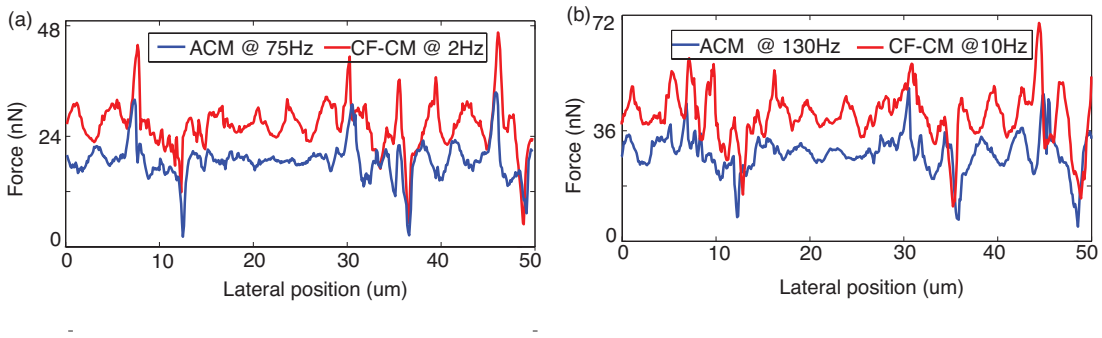

Figure 2.6: Comparison of the normal force at the cross-section marked in Fig. 2.5 when using the ACM technique at the scan rate of (a) 75 Hz and (b) 130 Hz to that when using the CF-CM imaging at (a) 2 Hz and (b) 10 Hz.

2.4.3 High-speed ACM imaging with Near Minimum Force

With the sample topography quantified using the proposed method, the quantified sample topography was utilized to implement the proposed ACM imaging. We first validated and evaluated the proposed gradient-based online optimization of the force (i.e., deflection) set-point to minimize the normal force in the ACM imaging. The calibration sample was imaged at two different high scanning rates of 75 Hz and 130 Hz (tip velocity: 7.5 mm/sec and 13 mm/sec, respectively) using the proposed ACM imaging, and then compared to the results obtained by the CF-CM imaging at 2 Hz and 10 Hz, respectively. The deflection set-point was updated line-by-line according to Eq. (2.4). The set-point of each scanline measured in the ACM imaging at the scan rates of 75 Hz and 130 Hz are shown in Figs. 2.5 (a1) and (a2), respectively, and the normal force (i.e., the cantilever deflection) measured during these two imaging processes are shown in Figs. 2.5 (b1) and (b2) as a 2-D force image, respectively, with comparison to those obtained by using the conventional CF-CM imaging at the scan rates of 2 Hz and 10 Hz in Figs. 2.5 (c1) and (c2), respectively. The initial force set-points of the ACM imaging at the scan rates of 75 Hz and 130 Hz (25 nN and 36 nN, respectively) were chosen the same as those used in the corresponding CF-CM imaging at the scan rates of 2 Hz and 10 Hz, respectively.

The experiment results clearly showed that the normal force was substantially reduced by using the gradient-based set-point optimization in the proposed ACM imaging. As shown in Figs. 2.5 (a1) and (a2), the adjusted force set-point was substantially lower than the corresponding a priori chosen value—the average force set-point was 21% and 24% lower than the

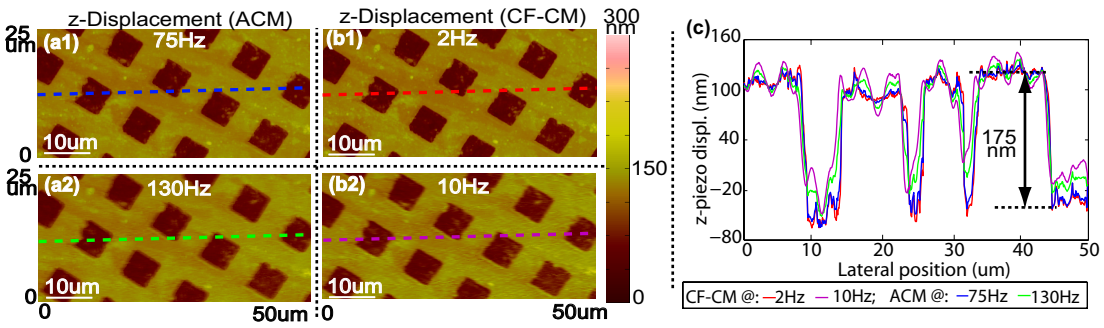

Figure 2.7: 2-D plot (i.e., image) of the z-piezo displacement measured during the imaging process by using the proposed ACM technique at the scan rate of (a1) 75 Hz and (a2) 130 Hz; And the CF-CM imaging at the scan rate of (b1) 2 Hz and (b2) 10 Hz; And (c) comparison of the cross-sections in each z-piezo displacement image at the same scan line (as marked out in (a1)-(b2)).

initial chosen value for the scan rate of 75 Hz and 130 Hz, respectively. As a result, the average and the maximum normal force of the ACM imaging at the scan rate of 75 Hz were 21% and 19% lower than those of the CF-CM imaging at 2 Hz, respectively. When comparing the ACM imaging at 130 Hz to the CF-CM imaging at 10 Hz, the reduction of the averaged and the maximum force were at 24% and 25%, respectively (compare Figs. 2.5 (b1) and (b2) to Figs. 2.5 (c1) and (c2)). such a significant force reduction can also be seen from the cross-section plot of the normal force in Fig. 2.6. Therefore, the near-minimum-force scan was achieved in the proposed ACM approach.

Secondly, we demonstrate the improvement of the sample topography tracking using the ACM technique. As shown in Figs. 2.7 (a1) and (b1), the z-piezo displacement image obtained using the ACM at 75 Hz was comparable with that from the CF-CM imaging at the scan rate of 2 Hz. For example, the RMS-difference between these two z-piezo displacements at the (randomly) selected cross-section (marked by the blue and red straight lines in Figs. 2.7 (a1) and (b1), respectively) was less than 6% (See Fig. 2.7 (c)). Moreover, the z-piezo displacement in the ACM imaging at 130 Hz scan was $\sim$ 12% more accurate than that in the CF-CM imaging at 10 Hz scan, both respect to the z-piezo displacement in the CF-CM imaging at 2 Hz. Therefore, the experimental results demonstrated that the proposed ACM imaging can substantially improve the sample topography tracking. Such an improvement in sample topography tracking provided the opportunity to further minimize the normal force.

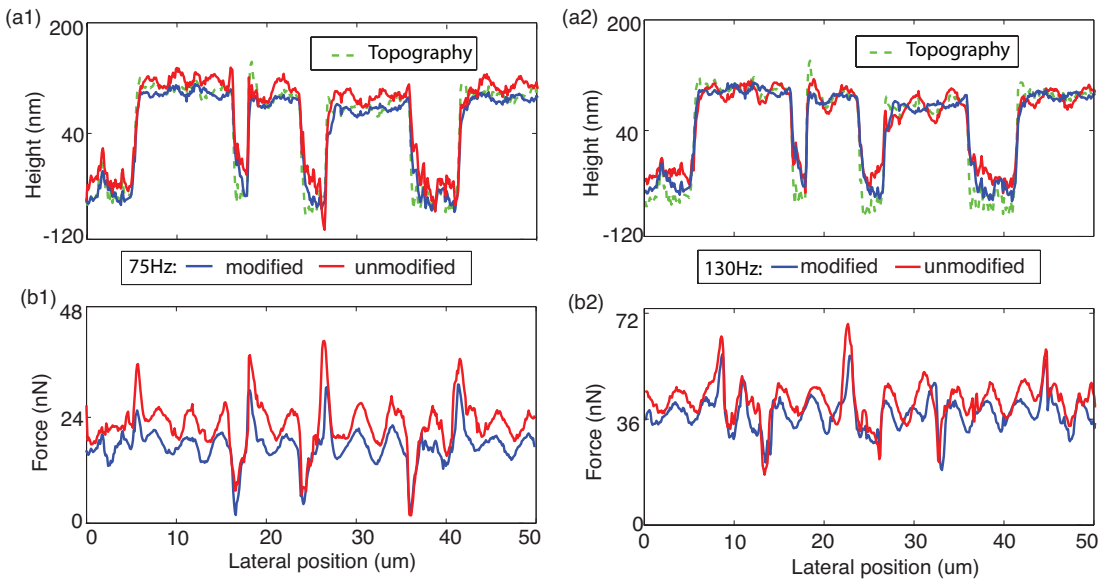

Figure 2.8: Cross-section comparison of the topography tracking performance (z-piezo displacement) (randomly chosen) measured using the modified topography profile (see Eq. (2.5)) in the proposed ACM approach at the scan rate of (a1) 75 Hz and (a2) 130 Hz to that measured when using the unmodified topography at these two scan rates, respectively, and the comparison of the corresponding normal force at the scan rate of (b1) 75 Hz and (b2) 130 Hz.

We also further evaluated the efficacy of the use of the modified sample topography in the feedforward control (see Eq. (2.5)) in improving the sample topography tracking and reducing the normal force, i.e., in reducing the amplitude of the "spikes" in the cantilever deflection. The modification coefficient α in Eq. (2.5) was experimentally tuned and set at 0.6. As an example, the z-piezo displacement on one scan line randomly picked from the topography image obtained by using the modified topography trajectory is compared to that obtained by using the original topography trajectory in the ACM technique in Figs. 2.8 (a1) and (a2) for the scan rate of 75 Hz and 130 Hz, respectively, and the corresponding normal force are compared in Figs. 2.8 (b1) and (b2), respectively. The efficacy of the modified topography profile in improving the sample topography tracking is evident from Figs. 2.8 (a1) and (a2): the overall difference (i.e., RMS-difference) between the z-piezo displacement and the topography profile was reduced from 18% to 7% and 32% to 21% at the scan rate of 75 Hz and 130 Hz, respectively. Such an improvement in sample topography tracking was also accompanied with a reduction of the normal force: the maximum (i.e., the amplitude of the largest force "spike") and the average force amplitudes were reduced by 24% and 19%, respectively, at 75 Hz scan,

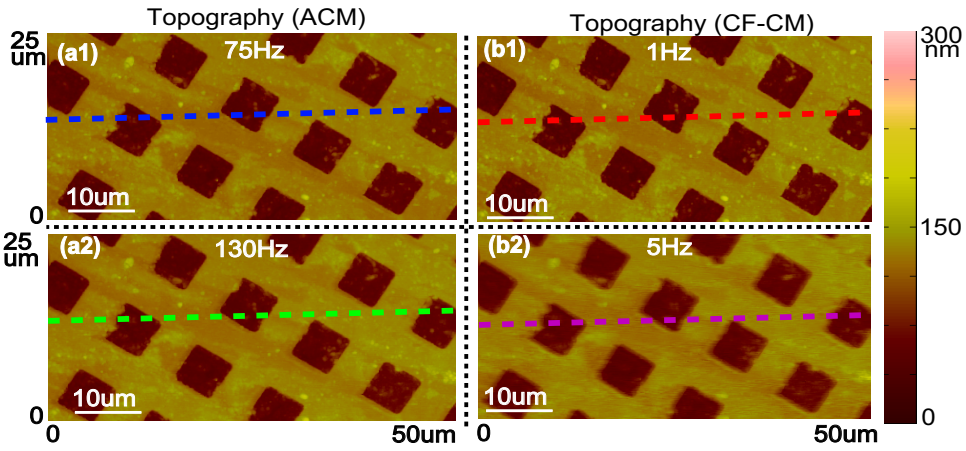

Figure 2.9: Images of sample topography obtained by using the proposed ACM technique at the scan rate of (a1) 75 Hz and (a2) 130 Hz, compared to those obtained by using the CF-CM at the scan rate of (b1) 1 Hz and (b2) 5 Hz.

and 18% and 15% at 130 Hz scan, respectively. Therefore, the experiment results demonstrated that the proposed modification of the topography profile in the feedforward control is efficient in reducing the normal force and improving the topography tracking during the ACM imaging.

Finally, the sample topography images using the proposed ACM technique were compared with the images obtained using the CF-CM. First, it can be seen that the quality of the topography image obtained by using the ACM technique at the scan rate of 75 Hz is almost the same as that obtained by the CF-CM imaging at 1 Hz—Both images presented almost the same details of the surface, e.g., the edges of the pitches and the particles ("dusts", compare Fig. 2.9 (a1) to Fig. 2.9 (b1)). Those details of the sample surface were well preserved when the scan rate was increased to 130 Hz when using the proposed ACM technique (see Fig. 2.9 (a2)), whereas lost in the CF-CM imaging at the scan rate of 5 Hz: As shown in Fig. 2.9 (b2), the pitch edges were blurry, so were those particles. The topography cross-section further confirmed these observations—the topography error (with respect to the topography of 1 Hz scan obtained by using Eq. (2.3)) of the image obtained by using the CF-CM at 5 Hz scan was 19% and 14% larger than that obtained by using the ACM technique at 75 Hz and 130 Hz scan, respectively (see Fig. 2.10).

Moreover, to further evaluate and demonstrate the proposed ACM, images of a smaller size (30 μm $\times$ 15 μm) and a larger size (80 μm $\times$ 40 μm) were also obtained using the ACM technique at the scan rates of 130 Hz and 200 Hz (for the smaller size imaging, with tip velocity

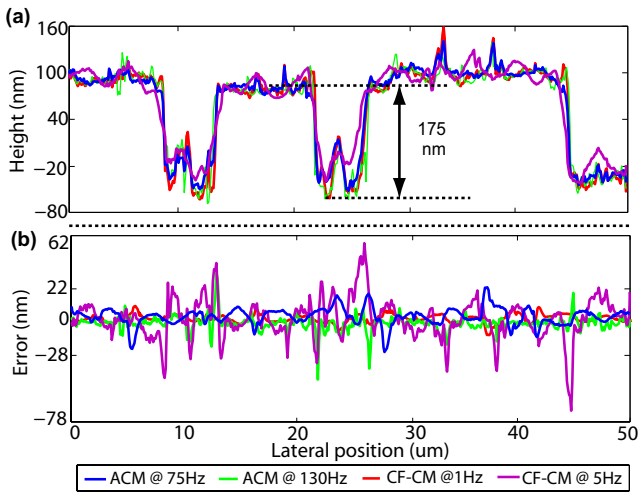

Figure 2.10: (a) Comparison of the corresponding topography profile cross-sections at the scan line as marked in Fig. 2.9; (b) Error of the sample topography obtained by using the proposed ACM technique at the scan rate of 75 Hz and 130 Hz with respect to the sample topography at 1 Hz scan (quantified via Eq. (2.3)), compared to those obtained by using the CF-CM imaging at 1 Hz and 5 Hz.

at 7.8 mm/s and 12 mm/s, respectively) and 40 Hz and 75 Hz (for the larger size imaging, with tip velocity at 6.4 mm/s and 12 mm/s, respectively), as shown in Figs. 2.11 and 2.12, respectively. The topography images (Figs. 2.11(a1)-(a2) and Figs. 2.12(a1)-(a2)) showed that the sample surface topography was consistently accurately quantified, and the normal force was consistently maintained closely around the minimal required level in both lower and larger size imaging across all scan rates. Particularly, the amplitude of the normal force during both the 130 Hz, 30μm imaging and the 40 Hz, 80μm imaging was mostly maintained below 25 nN across the entire image, substantially lower than that of the normal force exerted in the CF-CM imaging at much lower scan rate of 2 Hz at around 35 nN (Compare Figs. 2.11 (b1) and 2.12 (b1) with Fig. 2.5(c1)). Finally, the slightly loss of image quality in Fig. 2.11 (a2) was caused by the reduction of the imaging resolution by half (due to the sampling rate limit of the data acquisition-computation system), and the wear of the sample shown in Fig. 2.12 were caused by the wear of the calibration sample during the storage/transfer.

In summary, the experimental results demonstrated that the proposed ACM imaging technique increased the imaging speed by over 30 folds while substantially lowering the normal force during the imaging closely around the minimal needed force level.

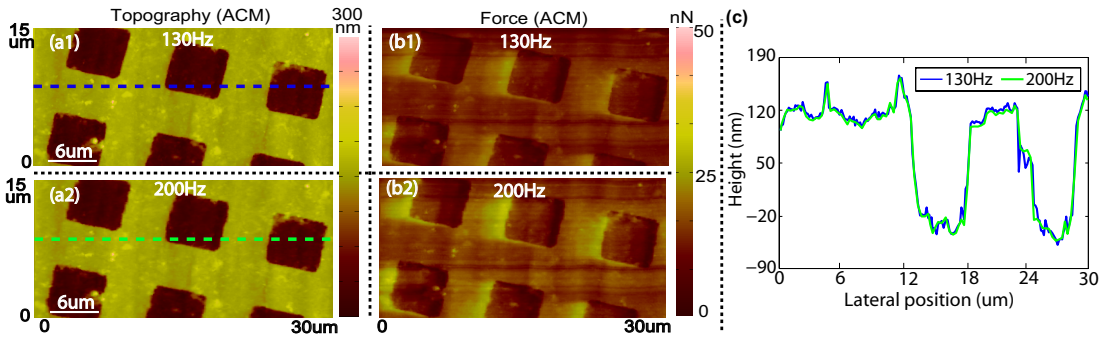

Figure 2.11: Images of sample topography obtained by using the proposed ACM technique at the scan rate of (a1) 130 Hz and (a2) 200 Hz, and images of the corresponding normal force (b1) and (b2) at the same scan rates, respectively, and (c) comparison of the topography profile cross-sections at the scan line as marked in (a1) and (a2).

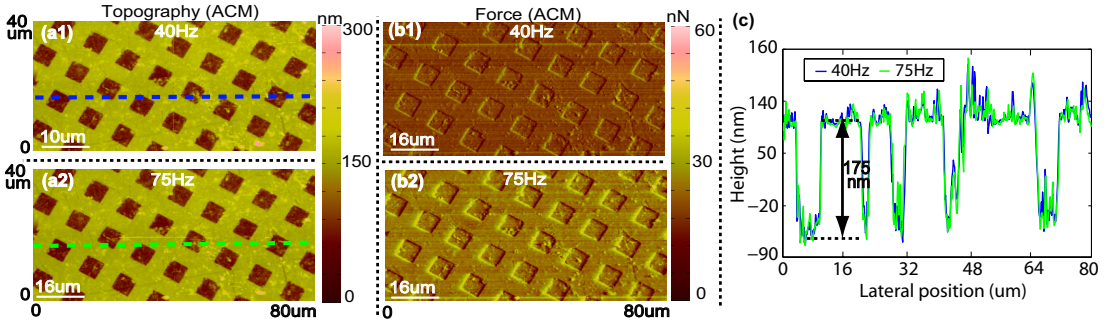

Figure 2.12: Images of sample topography obtained by using the proposed ACM technique at the scan rate of (a1) 40 Hz and (a2) 75 Hz, and images of the corresponding normal force (b1) and (b2) at the same scan rates, respectively, and (c) comparison of the topography profile cross-sections at the scan line as marked in (a1) and (a2).

2.5 Conclusion

An ACM imaging technique was proposed to achieve high-speed CM-imaging with near minimal contact force. The sample topography during CM-imaging was accurately quantified using both the z-piezo displacement and the cantilever deflection, and then the quantified sample topography was utilized in an iterative feedforward control scheme to achieve precision tracking of the sample topography during high-speed scanning, and in a gradient-based optimization scheme to adjust the deflection set-point line-by-line around the minimal level. The efficacy of the proposed ACM was demonstrated by imaging a silicon calibration sample at varies scan sizes and speed. The comparisons of the sample topography tracking performances and the normal forces between the proposed ACM imaging data and the CF-CM imaging results clearly

showed that the imaging speed was significantly increased by 30 folds over large-size imaging, and the normal force was substantially reduced by using the proposed ACM technique.

Chapter 3

High-Speed Atomic Force Microscope Imaging: Adaptive Multi-loop Mode

Abstract

In this chapter, an imaging mode (called the adaptive multi-loop mode) of atomic force microscope is proposed to substantially increase the speed of tapping mode (TM) imaging while preserving the advantages of TM-imaging over contact mode (CM) imaging. Due to its superior image quality and less sample disturbances over CM-imaging, particularly for soft materials such as polymers, TM-imaging is currently the de facto most widely used imaging technique. The speed of TM-imaging, however, is substantially (over an order of magnitude) lower than that of CM-imaging, becoming the major bottleneck of this technique. Increasing the speed of TM-imaging is challenging as a stable probe tapping on the sample surface must be maintained to preserve the image quality, whereas the probe tapping is rather sensitive to the sample topography variation. As a result, the increase of imaging speed can quickly lead to loss of the probe-sample contact and/or annihilation of the probe tapping, resulting in image distortion and/or sample deformation. The proposed adaptive multi-loop mode (AMLM) imaging overcomes these limits of TM-imaging through the following three efforts integrated together: First, it is proposed to account for the variation of the TM-deflection when quantifying the sample topography; Secondly, an inner-outer feedback control loop to regulate the TM-deflection is added on top of the tapping-feedback control loop to improve the sample topography tracking; And thirdly, an online iterative feedforward controller is augmented to the whole control system to further enhance the topography tracking, where the next-line sample topography is predicted and utilized to reduce the tracking error. The added feedback regulation of the TM-deflection ensures the probe-sample interaction force remains near the minimum for maintaining a stable

probe-sample interaction. The proposed AMLM-imaging is tested and demonstrated by imaging a poly(tert-butyl acrylate) sample in experiments. The experiment results demonstrated that the image quality achieved using the proposed AMLM-imaging at the scan rate of 25 Hz and over a large-size imaging (50 μm by 25 μm) is at the same level of that obtained using TM-imaging at 1 Hz, while the probe-sample interaction force is noticeably reduced from that achieved using the TM-imaging at 2.5 Hz.

3.1 Introduction

In this chapter, an imaging mode (called the *adaptive multi-loop mode*) of atomic force microscope (AFM) is proposed to substantially increase the speed of tapping mode (TM) imaging while preserving its advantages over contact mode (CM) imaging. TM-imaging is the de facto most widely used imaging technique of AFM–thanks to its superior image quality and subdued sample distortion when compared to CM-imaging [13, 14, 3, 4]. The rather slow imaging speed, however, has become the major limit and bottleneck of TM-imaging [1, 15]. High-speed TM-imaging is challenging as the increase of imaging speed can quickly lead to loss of probe-sample interaction and/or annihilated of cantilever tapping vibration, particularly when the imaging size is large. Current efforts to increase the speed of TM-imaging [14, 16], however, only lead to rather limited improvements as the speed increase is rather small (around 3 times), and accompanied with a substantial (over 5 times) increase of force applied. Thus, the challenges in and the needs for high-speed TM-imaging motivate the development of the proposed imaging technique. Although it has been reported that choosing a larger free vibration amplitude and a smaller tapping-amplitude set-point can avoid tip-sample interaction loss as the increase of the scanning speed [14, 16], large tip-sample interaction force is generated as a consequence of this effort [57, 58]. Control of the tip-sample interaction force remains as a challenge when imaging at high-speed and/or large size. The proposed approach aims to achieve large-size, high-speed hybrid mode imaging with the tip-sample interaction force regulated at the minimal level and the cantilever tapping vibration motion steadily maintained.

As been widely acknowledged, it is challenging to increase the speed of TM-imaging. The

speed of the TM-imaging is constrained by the time-delay existed in the z-axis feedback control in maintaining the *same* cantilever vibration amplitude throughout the imaging (scanning) process. In TM-imaging, the x-y-z 3D positioning of the probe relative to the sample is needed to maintain RMS-tapping amplitude at the set-point value so that the sample topography can be measured as the z-axis piezo displacement at each scanned sample point [1, 16]. As multiple periods of the tapping vibration needs to be acquired by the lock-in amplifier to measure the RMS-tapping-amplitude, time-delay is inevitably induced into the z-axis feedback loop, i.e., the measured RMS-tapping-amplitude differs from and lags behind the instant tapping-amplitude, especially when the tapping-amplitude varies along with the sample topography variation. At low speed imaging, such a time-delay is relatively small and can be compensated for by the z-axis feedback control, and the z-axis piezo displacement can closely track the sample topography throughout the imaging process. However, the time-delay becomes more pronounced as the scan speed increases, and adversely affects the z-axis control in tracking the sample profile, leading to a larger variation in the probe-sample distance as the cantilever tapping is very sensitive to the change of the probe-sample distance [58, 16]. As a consequence of the probe-sample distance change, loss of sample-probe contact and/or annihilation of tapping occurs when the imaging speed increases. Specifically, loss of probe-sample contact tends to occur around the sample regions where, e.g., sudden topography drop appears, and the tapping of the cantilever approaches the free oscillation gradually with a relatively large settling time proportional to the high-Q factor of the cantilever [1, 15]. On the contrary, the tapping can be completely annihilated around the sample regions where, e.g., sudden topography increase occurs, resulting in the sliding of the probe on the sample surface during the scanning and further sample distortion. However, these issues cannot be compensated for due to the nature of the TM-imaging in utilizing the RMS-tapping-amplitude as the z-axis control objective.

Current efforts to improve the imaging speed of TM-imaging only results in rather limited improvements. For example, it has been proposed to utilize high bandwidth piezo actuators and cantilevers with high resonant frequencies [59, 38] to increase the TM-imaging speed up to $\sim$2mm/sec [60]. The lateral size and the sample height that can be imaged, however, are both substantially reduced (from around 100 μm by 100 μm to 30 μm by 30 μm, and from 10 μm to 3 μm, respectively). Alternative to such a hardware-based approach that is accompanied

with instrument/material cost increase, control techniques [16, 61] such as the observer-based approach [40] have been developed to increase TM-imaging speed with minor or no additional cost. The speed increase achieved, however, is rather limited (e.g, $<$1.8 mm/sec [61, 40]), or the speed is increased at the cost of image quality, and more seriously, without adequate control in the interaction force as in the observer-based approach [40]. Therefore, it still remains as a challenge to achieve high-speed, large-size imaging of tapping-mode with the interaction force well controlled.

The proposed approach aims to not only substantially increase the TM-imaging speed without loss of image quality, but also maintain the probe tapping closely around the set-point and the tip-sample interaction force around the minimal (needed for maintaining a stable tapping) throughout the imaging process. Such an improvement in both the imaging speed and the interaction force control is achieved through the development of an adaptive multi-loop mode (AMLM) imaging scheme that regulates both the tapping amplitude and the mean cantilever deflection (called the *TM-deflection* later). Specifically, the proposed AMLM-imaging is composed of the following three ingredients: (i) Unlike the conventional TM-imaging that completely ignores the TM-deflection variation, it is proposed to take the variation of the cantilever TM-deflection into account when quantifying the sample topography. (ii) Unlike TM-imaging that only regulates the tapping-amplitude via the RMS-amplitude feedback control, the proposed AMLM-imaging explores an inner-outer feedback control loop to regulate the TM-deflection on top of the RMS-amplitude feedback. (iii) A data-driven online iterative feedforward controller is augmented to overcome the time-delay of the RMS-amplitude feedback loop, where the next-line sample topography and tracking error are predicted and utilized to further improve the topography tracking.

The experimental implementation of the proposed approach demonstrated that compared to TM-imaging, the proposed AMLM-imaging not only increased the imaging speed by over 10 folds, but at the same time, also reduced the tip-sample interaction force by 35%. Using the proposed AMLM-imaging the average lateral scanning speed reached 2.5 mm/sec when imaging a poly(tert-butyl acrylate) (PtBA) sample (scan rate: 25 Hz, scan size: 50 μm). Even at such a high speed, the image quality was maintained as that when using TM-imaging at over 20 folds slower (1 Hz), with the tip-sample interaction force maintained around the minimal

level.

The remainder of this chapter is organized as follows. In Sec. 3.2, the new sample topography quantification is proposed and employed to reveal the drawbacks of the AMLM-imaging, followed by the proposed AMLM technique in Sec. III. The experimental implementation of the proposed AMLM-imaging is described and discussed with comparison to the conventional TM imaging in Sec. 3.4. The conclusions are given in Sec. 3.5.

3.2 Issues of the Conventional Tapping Mode Imaging

TM-imaging was developed to address the issues of contact-mode imaging (CM-imaging) caused by probe sliding [1, 58] in imaging resolution and sample distortion [13, 14], particularly for soft samples. Unlike in CM-imaging, during TM-imaging the cantilever probe is excited (usually using a small piezo stack actuator, called dither piezo see Fig. 3.1) to vibrate around its resonance and intermittently interact with the sample, i.e., tap on the sample surface. Then the RMS-amplitude of the cantilever vibration (RMS-A_{def}) is measured using a lock-in amplifier, and maintained around the set-point value, A_{set}, through a feedback control system (see Fig. 3.1) using a piezoelectric actuator (called the **z-piezo** below). Provided that the sample topography profile is closely tracked by the cantilever probe during the scanning, signaling by the RMS-amplitude being close enough to the set-point value, the sample surface topography can be quantified as the z-piezo displacement. As virtually no probe sliding on the sample surface occurs during TM-imaging, the sliding-related sample damage is largely avoided, and higher imaging resolution can be achieved [1, 62].

3.2.1 Limits of the RMS-Tapping Feedback Control System

Speed of TM-imaging, however, is inherently hindered by the limits of the z-axis feedback control system (called *the RMS-z-feedback* below). As multiple periods of the tapping are needed to measure the RMS-tapping-amplitude, time-delay is inevitably induced into the RMS-z-feedback loop, i.e., the measured RMS-tapping-amplitude differs from and lags behind the instantaneous tapping-amplitude, $A_{\text{def}}(t)$, especially when the tapping-amplitude varies with the sample topography variation. Such a time-delay, although is relatively small and can be

compensated for by the RMS-z-feedback control when imaging at slow speeds, becomes more pronounced as the scan speed increases, and adversely affects the RMS-z-feedback control in the sample profile tracking, leading to a large variation in the probe-sample distance.

The cantilever tapping, however, is sensitive to the change of the probe-sample distance [58, 16] as in TM-imaging the probe-sample interaction force is highly nonlinear w.r.t. the probe-sample distance (see Fig. 3.2). The probe-sample distance change due to the imaging speed increase can result in loss of sample-probe contact and/or annihilation of tapping. Specifically, loss of probe-sample contact tends to occur around the sample regions where, e.g., sudden topography drops appear, and the cantilever tapping approaches free oscillation gradually with a relatively long settling time (due to high-Q factor of the cantilever) [1, 15]. Contrarily, tapping can be completely annihilated around the sample regions where, e.g., sharp topography increases exist, resulting in the probe sliding on the sample surface. Due to the time-delay, it is, however, challenging to avoid the loss of probe-sample contact and annihilation of tapping during high-speed imaging. The time-delay limits the use of a high feedback gain in the RMS-z-feedback, as a high feedback gain tends to result in overshoot in the response [63, 64], which, in turn, leads to the cantilever motion bouncing back and forth between the loss of contact and the annihilation of tapping. A small feedback gain, however, is also incapable of accounting for the loss of contact and/or annihilation of tapping as the imaging speed increases. Therefore, the control mechanism employed in TM-imaging is not adequate for high-speed TM-imaging.

Current efforts to improve the speed of TM-imaging result in rather limited progresses. We

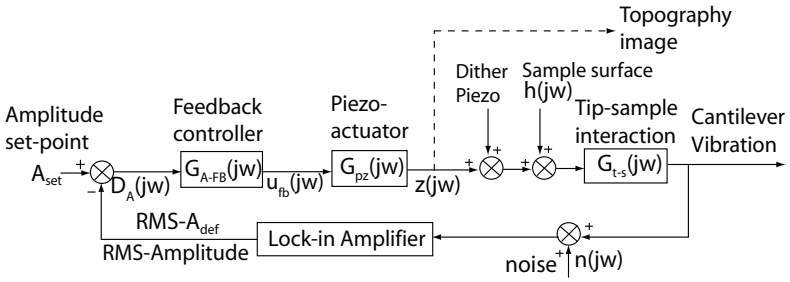

Figure 3.1: Schematic block diagram of the RMS-z-feedback control in the conventional TM-imaging.

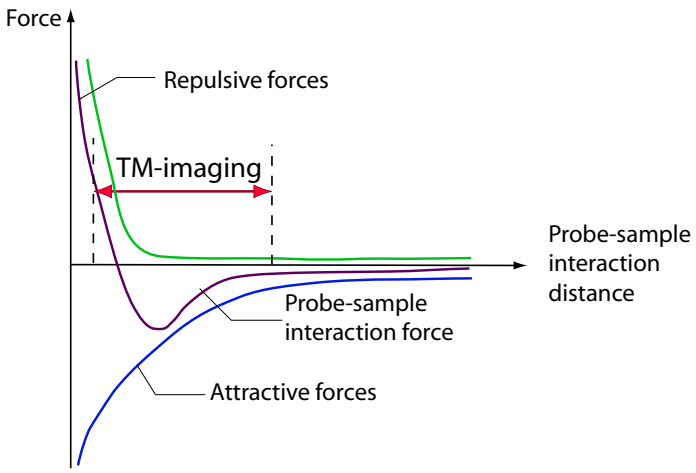

Figure 3.2: A schematic plot of probe-sample interaction distance vs. the probe sample interaction force.

note that the speed of TM-imaging can be increased by choosing a larger free vibration amplitude and a smaller tapping-amplitude set-point [14, 16]. Such a choice, however, results in much larger probe-sample interaction force. Given a cantilever probe with mass m, quality factor Q, and spring constant k_c, the probe-sample interaction force, $F_{t-s}(t)$, during TM-imaging can be estimated as [57, 58]

$$\begin{aligned} F_{t-s}(t) &= m\ddot{d}_{tot}(t) + \frac{m\omega_0}{Q}\dot{d}_{tot}(t) + k_c d_{tot}(t) \\ \text{with} \quad d_{tot}(t) &= d_{TM}(t) + [A_{\text{def}}\cos(\omega_0 t + \phi) - A_{\text{free}}\cos(\omega_0 t)], \end{aligned} \tag{3.1}$$

where $d_{tot}(t)$, $d_{TM}(t)$, and iA_{free} are the total deflection, the mean deflection per vibration period (called *TM-deflection*), and the free vibration amplitude of the cantilever, respectively. ϕ denotes the phase shift of the cantilever's response to the excitation. Thus, Eq. (3.1) clearly implies that the combination of a larger A_{free} and a smaller A_{def} increases the total probe-sample interaction force, $F_{t-s}(t)$. Furthermore, this combination also implies a smaller probe-sample separation distance, resulting in a larger TM-deflection, thereby, a larger average probe-sample interaction force per vibration period, i.e., [57, 58]

$$< F_{t-s} >= (1/T)\oint F_{t-s}(t)dt = k_c d_{TM}, \quad \text{with} \quad T = 2\pi/\omega_0, \tag{3.2}$$

To overcome this constraint, it has been proposed to employ a high bandwidth z-piezo with active Q control to increase the TM-imaging speed [15, 16]. The speed increase achieved, however, is rather limited ($\leq$ 300 μm/s at the scan size of 50 μm) as the time-delay of the

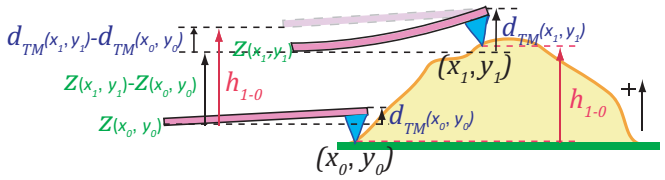

Figure 3.3: Height difference between two points on the sample surface during TM-imaging.

RMS-amplitude feedback is still the bottleneck—even though the loss of contact and the annihilation of tapping can be largely avoided, $d_{TM}(t)$ still varies substantially as the imaging speed increases, directly resulting in large image distortion.

3.2.2 Topography Quantification in TM-Imaging

We propose to quantify the sample topography by taking the TM-deflection into account. Consider, during TM-imaging, the probe-sample interaction at two different locations on the sample surface, point $(x_0,\, y_0)$ and point $(x_1,\, y_1)$ (see Fig. 3.3), and the z-piezo positions and the TM-deflections at these two points are denoted as $z(x_0,\ y_0)$ and $z(x_1,\ y_1)$, and $d_{TM}(x_0,\ y_0)$ and $d_{TM}(x_1,\ y_1)$, respectively, then the height difference between these two points is given as

$$h_{1-0} = [z(x_1, y_1) - z(x_0, y_0)] + \varepsilon[d_{TM}(x_1, y_1) - d_{TM}(x_0, y_0)], \tag{3.3}$$

where ε is the contact constant that depends on the probe-sample interaction regime: $\varepsilon = -1$ when the probe-sample interaction is dominated by the long range attractive force (e.g., $A_{def}/A_{\text{free}} \in (0.5, 0.8)$), $\varepsilon = 1$ when the repulsive probe-sample interaction force appears, and $-1 \ll \varepsilon < 0$ when the tapping amplitude is close to the free vibration amplitude, i.e., $A_{def} \approx A_{\text{free}}$. Thus, the above Eq. (3.3) implies that the sample topography of the entire imaged area can be obtained with respect to one fixed reference point, e.g., the first sample point imaged—for convenience. Without loss of generality, the height and deflection datum point can be set as $z(x_0, y_0) = 0$ and $d_{TM}(x_0, y_0) = d_{TM-d}$ (i.e., the TM-deflection corresponding to the tapping amplitude at the set-point value), respectively, and the sample surface topography can be quantified as

$$h(x, y) = z(x, y) + \varepsilon[d_{TM}(x, y) - d_{TM-d}] = z(x, y) + \varepsilon\Delta d_{TM}(x, y). \tag{3.4}$$

The above Eq. (3.4) clearly reveals the imaging errors in high-speed TM-imaging. At slow imaging speeds, the cantilever probe can accurately follow the sample topography under the

RMS-z-feedback control, i.e., A_{def} is closely around the set-point value and the TM-deflection variation $\Delta d_{TM}(t)$ is small enough, hence, the sample topography can be adequately quantified as the z-piezo displacement, i.e., as $d_{TM}(x,y) \approx d_{TM-d}$, $h(x,y) \approx z(x,y)$ in Eq. (3.4). However, with the imaging speed increase it is challenging to maintain such a stringent condition ($A_{\text{def}} \approx A_{\text{set}}$). Even when the scanning speed increases slightly and no loss of contact nor annihilation of tapping occurs, i.e., when the variation of the RMS-tapping-amplitude is small (the variation of the instantaneous tapping-amplitude, A_{def}, however, may not be negligible), variations of the TM-deflection can still be pronounced, specially in the so called *soft tapping mode* imaging [14, 65] (where the tapping-amplitude of the cantilever is less than 50% of the free vibration amplitude), i.e., $d_{TM}(x,y) \neq d_{TM-d}$. The variation of TM-deflection, not accounted for in the conventional TM-imaging, thereby directly leads to image distortion. Therefore, the conventional sample topography quantification also limits the TM-imaging.

We note that although Eq. (3.4) implies the speed of TM-imaging might be increased by accounting for the TM-deflection in the sample topography quantification, such a modification does nothing to improve the sample topography tracking, i.e., as the imaging speed increases, the probe-sample interaction force, $< F_{t-s} >$, can vary dramatically and quickly leads to loss of contact and/or annihilation of tapping. Thus, maintaining the sample topography tracking is essential to high-speed TM-imaging.

3.3 Adaptive Multi-loop Mode Imaging

We propose the adaptive multi-loop mode imaging (AMLM-imaging) to address the above issues. In essence, in the proposed imaging mode, control of the z-axis motion of the probe combines the RMS-z-feedback loop in TM-imaging with the deflection feedback loop in CM-imaging, while maintaining the tapping amplitude of the probe as in TM-imaging—the adaptive multi-loop mode.

As depicted in Fig. 3.4, the proposed AMLM-imaging introduces two major components on top of the RMS-z-feedback loop to control the z-axis motion of the probe: (i) A feedback control in the inner-outer loop structure to regulate the TM-deflection, and (ii) an online iterative feedforward controller to overcome the time-delay of the RMS-z-feedback loop in tracking

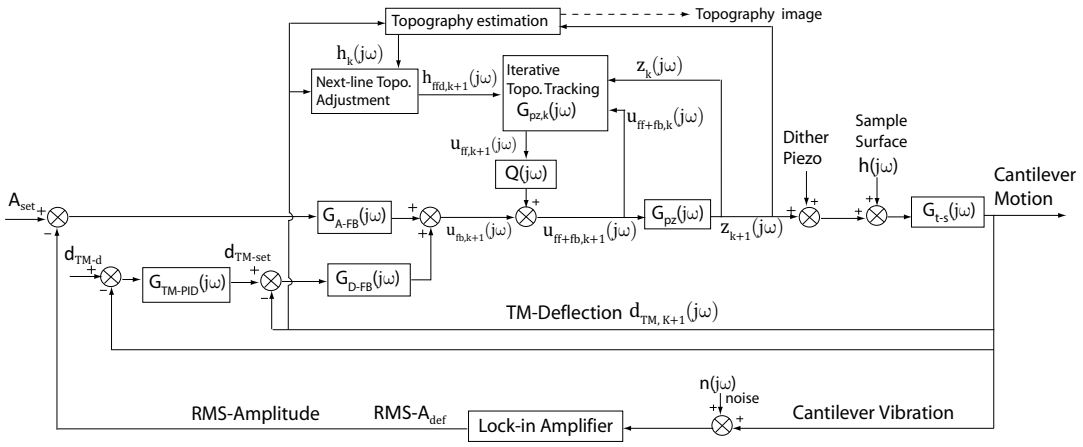

Figure 3.4: Schematic block diagram of the proposed AMLM-imaging.

the sample topography.

3.3.1 TM-deflection Regulation: An Inner-Outer Feedback Control Approach

The TM-deflection inner-outer feedback loop regulates the averaged (vertical) position of the cantilever in each tapping period closely around the desired value for maintaining a stable tapping. Specifically, the outer-loop regulates the TM-deflection set-point, $d_{\text{TM-set}}(\cdot)$, while the inner-loop tracks the regulated TM-deflection set-point. The outer-loop employs the following PID-type of control,

$$\begin{aligned} d_{\text{TM-set}}(j+1) &= k_I d_{\text{TM-set}}(j) + k_P e_{\text{TM}}(j) + k_D[e_{\text{TM}}(j-1) - e_{\text{TM}}(j)] \qquad (3.5) \\ \text{with} \quad e_{\text{TM}}(j) &= d_{TM-d} - d_{\text{TM}}(j), \quad \text{and} \quad j = 2...N-1, \end{aligned}$$

where N is the total number of sampling periods per image, and k_P, k_I, and k_D are the proportional, integral, and derivative coefficients, respectively. The desired TM-deflection, d_{TM-d}, is determined by the ratio of the chosen tapping-amplitude set-point to the free amplitude, $A_{\text{set}}/A_{\text{free}}$. To choose A_{set} and d_{TM}, the d_{TM} vs. $(A_{\text{def}}/A_{\text{free}})$ relation is needed and can be measured a priori. Previous study [58] showed that the d_{TM} vs. $(A_{\text{def}}/A_{\text{free}})$ relation resembles a parabolic curve centering around $A_{\text{def}}/A_{\text{free}}$ at $\sim 50\%$. As can be seen from the exemplary d_{TM} vs. $(A_{\text{def}}/A_{\text{free}})$ plot measured in this work shown in Fig. 3.5, the tip-sample interaction force increases significantly when the tapping ratio $A_{\text{def}}/A_{\text{free}} < 10\%$, whereas when $A_{\text{def}}/A_{\text{free}}$ is larger than 80%, the increase of the scanning speed can quickly lead to the loss

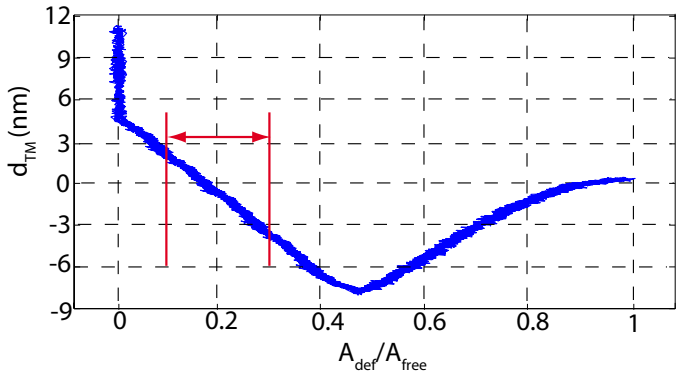

Figure 3.5: d_{TM} vs. $A_{\text{def}}/A_{\text{free}}$.

of contact. Thus, for the d_{TM} vs. $(A_{\text{def}}/A_{\text{free}})$ plot shown in Fig. 3.5, the A_{set} shall be chosen around 10%-30%A_{free} (since the corresponding tip-sample interaction force is small), and the desired TM-deflection is then picked according to Fig. 3.5.

3.3.2 Online Iterative Feedforward Control for Sample-Topography Tracking

To further enhance the tracking of the sample topography, and thereby, the imaging speed, an online iterative feedforward controller of the piezo actuator is integrated to the RMS-z-feedback loop (see Fig. 3.4), by implementing the following the high-order modeling-free difference-inversion-based iterative-control (HOMDIIC) algorithm [66] online,

$$\begin{aligned} U_{\text{ff,0}}(j\omega) &= 0, \\ U_{\text{ff,1}}(j\omega) &= \frac{U_{\text{ff+fb,0}}(j\omega)}{Z_0(j\omega)} H_{\text{ffd,1}}(j\omega), \\ U_{\text{ff,k+1}}(j\omega) &= U_{\text{ff,k}} + \lambda \frac{U_{\text{ff+fb,k}}(j\omega) - U_{\text{ff+fb,k-1}}(j\omega)}{Z_{\text{k}}(j\omega) - Z_{\text{k-1}}(j\omega)} e_{\text{k}}(j\omega), \quad k \geq 1 \\ e_{\text{k}}(j\omega) &= H_{\text{ffd,k+1}}(j\omega) - Z_{\text{k}}(j\omega) \end{aligned} \tag{3.6}$$

where '$j\omega$' denotes the Fourier transform of the corresponding signal, λ is a pre-chosen constant to ensure the convergence of the iteration, and $U_{\text{ff+fb,k}}(\cdot)$ and $Z_{\text{k}}(\cdot)$ are the total control input (feedback+feedforward) applied to the z-piezo actuator (i.e., $U_{\text{ff+fb,k}}(j\omega) = U_{\text{ff,k}}(j\omega) + U_{\text{fb,k}}(j\omega)$, see Fig. 3.4) and the z-piezo displacement measured on the k^{th} scan line, respectively, and $H_{\text{ffd,k+1}}(\cdot)$ denotes the desired trajectory that the z-piezo needs to track at the $k+1^{th}$ scanline. Note that the ratios in the above control law, $U_{\text{ff+fb,0}}(j\omega)/Z_0(j\omega)$ and

$(U_{\text{ff+fb,k}}(j\omega) - U_{\text{ff+fb,k-1}}(j\omega))/(Z_{\text{k}}(j\omega) - Z_{\text{k-1}}(j\omega))$, essentially equal the inverse of the frequency response of the z-piezo actuator, and are updated line-by-line iteratively throughout the imaging process. Such a data-driven online-updated inverse is preferred over a priori-obtained fixed model in the iterative scheme [9, 37] for better robustness and tracking performance [32]. The feedforward input for the next scanline, $U_{\text{ff,k+1}}(j)$ for $j = 1, ..., N_l$ (N_l: total number of sampling points per scanline), was computed during the sampling period between the last sampling point of the current scanline and the first sampling point of the next scanline by using the HOMDIIC algorithm (Eq. (6)) in frequency domain directly via discrete Fourier transform and discrete inverse Fourier transform. The computed $U_{\text{ff,k+1}}(\cdot)$ was then applied one point a (sampling) time during the next line imaging.

The other feature of the above feedforward controller is that the desired trajectory to track in Eq. (3.6), $H_{\text{ffd,k}}(\cdot)$, accounts for both the predicted sample topography and the predicted next-line TM-deflection tracking error. Specifically, at the end of the k^{th} line scanning, the sample topography profile of the $k + 1^{th}$ scanline, $h_{\text{k+1}}(t)$, is approximated as that of the k^{th} scanline (quantified via Eq. (3.4)), i.e., $h_{\text{k+1}}(t) \approx h_{\text{k}}(t)$. Such an approximation is reasonable as with enough scanlines, the line-to-line topography variations are small. Similarly, the TM-deflection tracking error on the $(k + 1)^{th}$ scanline is predicted (approximated) as that on the k^{th}, $d_{TM,k}(\cdot) - d_{TM-d}$, if the same control were applied. Then, the next-line desired trajectory, $h_{\text{ffd,k+1}}(t)$, is obtained by combining the above two predictions as follows,

$$h_{\text{ffd,k+1}}(j) = h_{\text{k}}(j) + \alpha[d_{\text{TM,k}}(j) - d_{TM-d}], \quad j = 1, ...N_l. \tag{3.7}$$

where N_l and α are the total sampling points per scanline and the correction factor, respectively.

The TM-deflection is introduced in the above iterative algorithm (Eq. (3.7)) to reduce the amplitude of the interaction force when imaging sample areas of rapid and large topography changes (vertically). Note that the TM-deflection responds faster to the sample topography changes than the tapping amplitude.However, due to the compliance of the cantilever and the cantilever fixture (connecting the cantilever to the piezo actuator), time delay still exists between the cantilever deflection change and that of the topography profile. As the scanning speed increases, such a time delay, albeit small, becomes crucial and as a result, the spikes in

the TM-deflection reach their (local) peaks *after* the probe already passes these sample locations. Even with advanced feedback control, such deflection spikes still exist [43, 11]. The above modified desired trajectory—for the feedforward control input to track—enables the z-piezo to drive the cantilever to respond in advance (i.e., pre-actuate) to the topography change, thereby reducing the amplitude of the deflection spikes. The correction factor α can be tuned based on the estimated height of the sample surface features.

During the imaging process, the above iterative scheme is applied repetitively to scan on the first line until the convergence is reached, i.e., until the difference of the z-piezo displacement between two consecutive iterations is small enough, e.g., close to the noise level (our experiments below showed that only a couple of repetitive scans on the first line were needed). Then the converged input is used as the initial input for the iteration on the next scanline. Provided that the correction rate of the iterative input (i.e., the convergence rate) is faster than line-to-line the input change caused by the sample topography change, the iterative control input only needs to be updated once, i.e., the rest of the sample can be imaged without iteration! Similar idea has been explored recently [54, 11]. However, unlike the work in [54, 11] that used an a *fixed* model of the closed-loop dynamics, we propose here to use and update (using the measured input-output data) the frequency response of the z-axis piezo actuator itself. The use of the z-piezo dynamics itself provides a larger "working" bandwidth, i.e., a better tracking performance at high-speed, as the feedback controller tends to reduce the open-loop bandwidth. Our experiment implementation below (See Sec. IV) demonstrated such an improvement .

Finally, to avoid noise being fed back into the closed-loops via the feedforward channel, the feedforward control input, $U_{\text{ff,k+1}}(\cdot)$, is passed through a zero-phase low-pass filter $Q(j\omega)$,

$$\hat{U}_{\text{ff,k+1}}(j\omega) = Q(j\omega)U_{\text{ff,k+1}}(j\omega) = Q_b(j\omega)C_{\text{lead}}(j\omega)U_{\text{ff,k+1}}(j\omega), \tag{3.8}$$

where $Q_b(j\omega)$ and $C_{\text{lead}}(j\omega)$ are a low-pass filter and a phase-lead compensator, respectively. As the entire next-line feedforward control input is known a priori, the above noncausal zero-phase filter can be implemented online.

The added TM-deflection feedback loop along with the feedforward controller substantially accelerates the tracking of the sample topography during imaging. Maintaining the TM-deflection around the desired value helps to maintain the RMS tapping amplitude around the

set-point, particularly, around the set-point at which the corresponding TM-deflection is minimal, resulting in the averaged probe-sample interaction force, $< F_{t-s} >$, being minimized. In this experiment, $A_{\text{def}}/A_{\text{free}} = 20\%$ was chosen so that $d_{TM-d} \approx 0$ (see Fig. 3.5). Moreover, the feedforward controller, by tracking the optimal predicted sample topography profile with rapid convergence, further reduces the tapping amplitude oscillations upon sudden sample topography variation when the scanning speed increases. Therefore, the proposed TM-deflection loop along with the data-driven iterative feedforward control play a major role in improving the quality and interaction force control of TM-imaging.

3.4 Experimental Implementation and Discussion

A sample of random and irregular pattern of poly(tert-butyl acrylate) (PtBA) on a silicon substrate was imaged at both small and large size imaging (20 μm and 50 μm, respectively) to validate and demonstrate the proposed technique, by comparing to TM-imaging at much lower speed. The sample was prepared by quickly evaporating a droplet of 20 μL PtBA solution at 1 mg/ml concentration on a hot silicon substrate. Under both the "coffee-ring" effect [67] and the fingering instability [68] during the evaporation, a sample topography of large-scale (vertically and horizontally) PtBA aggregation and randomly distributed nanometer-size dots co-existing side by side was produced, well suited for evaluating and demonstrating the proposed AMLM-imaging technique.

3.4.1 Implementation of the AMLM-Imaging Technique

The experiments were conducted on a commercial AFM (Dimension Icon, Bruker AXS Inc.) on which both the drive of the piezo actuators and all of the sensor signals including the TM-deflection and the piezo displacement sensor signals can be directly accessed. All of the signals were acquired through a computer-based data acquisition system (NI-6259) under the Matlab xPC-target environment.

Throughout the imaging experiments, the HODMIIC technique was employed to achieve precise tracking in the lateral x-y axes scanning [69] by maintaining the tracking error below 1%. Moreover, the cross-axis dynamics coupling (mainly from the lateral x-y axes to the

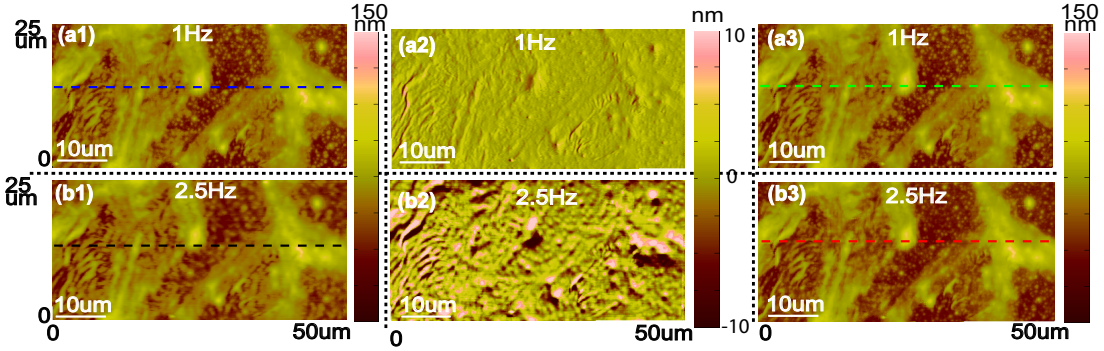

Figure 3.6: Sample topography images (scan area: 50 μm $\times$ 25 μm, scan direction: 50 μm) obtained by using the TM imaging at the scan rate of (a1) 1 Hz and (b1) 2.5 Hz; the corresponding TM-deflection measured at (a2) 1 Hz and (b2) 2.5 Hz; and the corresponding sample topography quantified using Eq. (3.4) at (a3) 1 Hz and (b3) 2.5 Hz.

vertical z-axis [55]) was compensated for by subtracting it from the z-piezo displacement measured. The PID controller parameters in Eq. (3.5) were set at $k_P = 1$, $k_I = 1$, and $k_D = \rho$, where ρ was a constant chosen a priori—the sample point-to-point gradient factor. Therefore, the differences in topography tracking, the tip-sample interaction force, the tapping amplitude, and the image quality presented below reflect the effects of the proposed sample topography quantification and the proposed AMLM-imaging approach over the conventional TM-imaging.

3.4.2 Sample topography quantification comparison

Experiments were conducted to validate the proposed topography quantification (Eq. (3.4)) first. As an example, results obtained at the scan rates of 1 Hz and 2.5 Hz over an imaging area of 50 μm$\times$25 μm are compared for the z-piezo displacement images (i.e., the sample "topography" obtained in TM-imaging) in Figs. 3.6(a1) and (b1), the TM-deflection $d_{TM}(x, y)$ in Figs. 3.6(a2) and (b2), and the true sample topography images quantified by Eq. (3.4) in Figs. 3.6(a3) and (b3), respectively. Moreover, the cross-section z-piezo displacement and the sample topography profile quantified by using Eq. (3.4) at a randomly-selected location are also compared in Fig. 3.7 for these two scan rates.

At the low imaging speed of 1 Hz, the sample topography can be quantified by using the

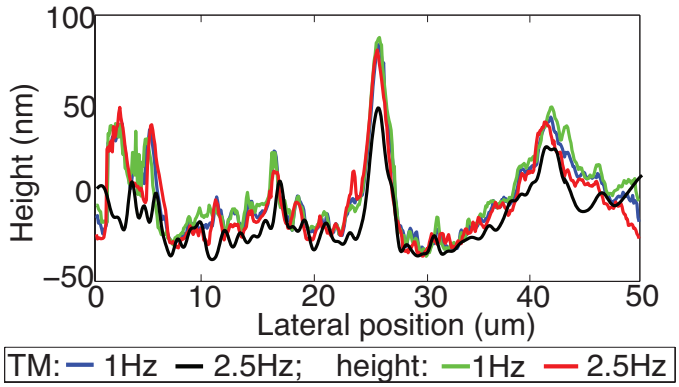

Figure 3.7: Comparison of the cross-sections at the same scan line of the three images as marked out in Figs. 3.6 (a1), (a3) and (b3).

TM imaging, i.e., the z-piezo displacement (see Fig. 3.6 (a1)). The averaged relative difference between the TM image (Fig. 3.6(a1)) and the topography image (Fig. 3.6 (a3)) by using Eq. (3.4) was only $\sim$4% (see Fig. 3.7). As the imaging speed increased to 2.5 Hz, however, the sample topography cannot be accurately tracked by the RMS-z-axis feedback control alone. As a result, the average tip-sample interaction force was increased by over 3 folds compared to that obtained during the 1 Hz TM imaging (compare Fig. 3.6 (a2) to Fig. 3.6 (b2)). With such a significant tip-sample interaction force increase, the TM image (the z-piezo displacement) at the scan rate of 2.5 Hz was 23% less accurate than the sample topography at the scan rate of 1 Hz quantified using Eq. (3.4). The image quality, however, was restored using the proposed topography quantification (Eq. (3.4)). As shown in Fig. 3.6 (b3), the difference between the low speed and the high speed scan was less than 7% (compare Fig. 3.6 (b3) to Figs. 3.6 (a3) and (b1), particularly those small dots distributed around the upper right region of the images. Also see the cross section comparison in Fig. 3.7). The probe-sample interaction force increased dramatically (over 3 folds) as the scan rate increased from 1 Hz to 2.5 Hz (compare Fig. 3.6 (a2) to Fig. 3.6 (b2)). Therefore, the experimental results demonstrated that the sample topography profile in TM-imaging can be accurately quantified by using the proposed method (Eq. (3.4)), while the substantial force increase clearly manifested the limits of TM-imaging.

3.4.3 High-speed near-minimum-force AMLM imaging

With the proposed sample topography quantification being validated, the proposed AMLM-imaging was implemented to image the PtBA sample at scan rate of 25 Hz (the average lateral scanning speed: 2.5 mm/s), and then compared to the results obtained using TM-imaging at 2.5 Hz. The z-piezo displacement images, the cross sections of the z-piezo displacement images, and the phase images obtained using these two methods are compared in Figs. 3.8–3.10, respectively. The z-piezo displacement comparison shows that the proposed AMLM-imaging can track the sample topography more accurately at the scan rate of 25 Hz than TM-imaging at the scan rate of 2.5 Hz. For example, those small dots near the upper right region of the image were sharper in Fig. (8) (a1) than those in Fig. (8) (a2). More specifically, by using the AMLM-imaging at 25 Hz, the relative difference between the z-piezo displacement in Figs. 3.8(a) and the sample height quantified in Fig. 3.6(a3) at a randomly selected cross-section (marked by the dashed lines in Fig. 3.8) was three times smaller than that of using TM-imaging at 2.5 Hz ($<8\%$ vs. 24%, see Fig. 3.9). Furthermore, the comparison of the phase images in Figs. 3.10 (a) and (b) also confirmed that the sample details through the phase contract were largely distorted when using TM-imaging at 2.5 Hz, whereas clearly preserved and presented when using the AMLM-imaging at 25 Hz. Therefore, the experimental results demonstrated that the proposed AMLM-imaging technique substantially improved the sample topography tracking. Such an improvement in sample topography tracking provided the opportunity to further reduce the tip-sample interaction force.

We further evaluated the AMLM-imaging in maintaining the near-minimum interaction force during the imaging, by regulating the TM-deflection set-point and maintaining the tapping-amplitude. The TM-deflection set-point was updated at every sampling point according to Eq. (3.5). The images of the averaged force (i.e., the TM-deflection) measured by using the AMLM-imaging at 25 Hz and TM-imaging at 2.5 Hz are compared in Figs. 3.11 (a1) and (b1), respectively. The tapping-amplitude set-point for both the imaging processes was chosen at 20% of the free vibration amplitude (with the corresponding TM-deflection $d_{TM-d} \approx 0\, nN$,

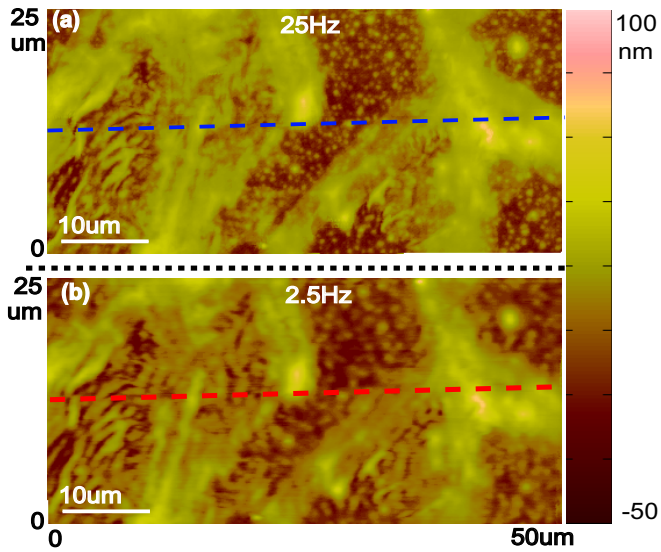

Figure 3.8: Top-view plot (i.e., image) of the z-piezo displacement obtained using (a) the proposed AMLM-imaging technique at the scan rate of 25 Hz; and (b) the TM-imaging at the scan rate of 2.5 Hz,respectively.

see Fig. 3.5), and images of the tapping-amplitude ratio measured in these two cases are compared in Figs. 3.11 (a2) and (b2), respectively. Also, the cross-section force and tapping-amplitude ratio variation at a randomly-selected location are compared in Figs. 3.11 (c1) and (c2), respectively.

The experiment results clearly demonstrated that both the averaged force and the tapping-amplitude fluctuation were substantially reduced by using the inner-outer feedback loop control of the TM-deflection along with the online iterative feedforward control in the proposed AMLM-imaging. The averaged force and the tapping-amplitude ratio mainly stayed in the regions of $\pm$5 nN and 15%–25%, respectively, when using the AMLM-imaging at 25 Hz, compared to the regions of -10–15 nN and 0–40%, respectively, when using the TM-imaging at 2.5 Hz. More specifically, at the cross-section (randomly selected) marked in Fig. 3.11, the amplitude of the averaged force and the fluctuation of the tapping-amplitude of the 25 Hz AMLM-imaging were 37% and 20% lower than those of the 2.5 Hz TM-imaging (See Figs. 3.11(c1) and (c2), respectively). Therefore, the proposed AMLM-imaging substantially reduced the probe-sample interaction force in TM-imaging as well.

Finally, the image quality of the proposed AMLM-imaging technique was evaluated, as shown in Fig. 3.12, where the sample topography image obtained by using the AMLM-imaging

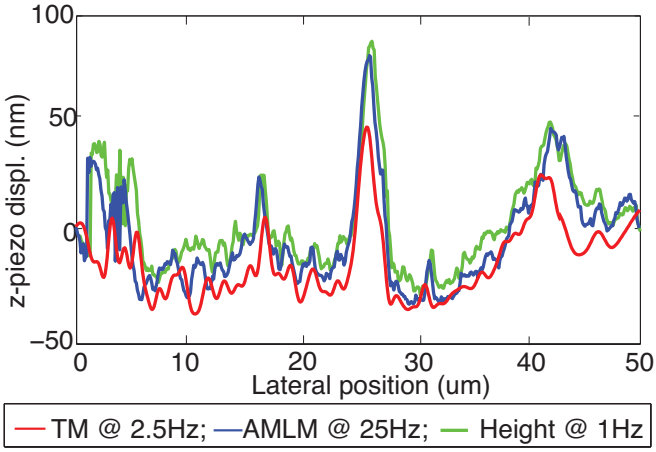

Figure 3.9: Comparison of the z-piezo displacement profile at the same cross-section location as marked out in Figs. 3.8(a), (b) and Fig. 3.6 (a3).

at 25 Hz is compared to that obtained using TM-imaging at 1 Hz. It can be seen that the image quality of the topography obtained by using the AMLM technique at 25 Hz was almost the same as that obtained by TM imaging at 1 Hz—Both images presented almost the same details of the sample surface (compare Fig. 3.12 (a) to Fig. 3.12 (b)), whereas those details were degraded in the TM image at the scan rate of 2.5 Hz, as shown in Fig. 3.6 (b1). The cross-section of the topography image further confirmed these observations—the topography difference (with respect to the topography of 1 Hz TM scan obtained by using Eq. (3.4)) obtained using the AMLM-imaging at 25 Hz was 20% smaller than that obtained using the TM at 2.5 Hz (see Fig. 3.13). We realize that such a substantial imaging speed increase–25 folds–with the image quality maintained was achieved at the cost of increased probe-sample interaction force. The force increase, however, was rather small–the RMS total interaction force (quantified by Eq. (3.2)) during the imaging was only increased by 18%, and was 35% smaller than that of the TM-imaging at 2.5 Hz. Therefore, the experimental results demonstrated the efficacy of the AMLM-imaging in substantially increasing the imaging speed of TM-imaging.

To further evaluate and demonstrate the proposed AMLM-imaging, images of the sample sample over a smaller size (20 μm $\times$ 10 μm) were also obtained using the AMLM-imaging at the scan rate of 40 Hz, as shown in Figs. 3.14, respectively. The topography images (Figs. 3.14(a1)-(a2)) showed that both the taller and lower sample surface features were captured consistently, and the averaged force and the tapping amplitude were maintained closely

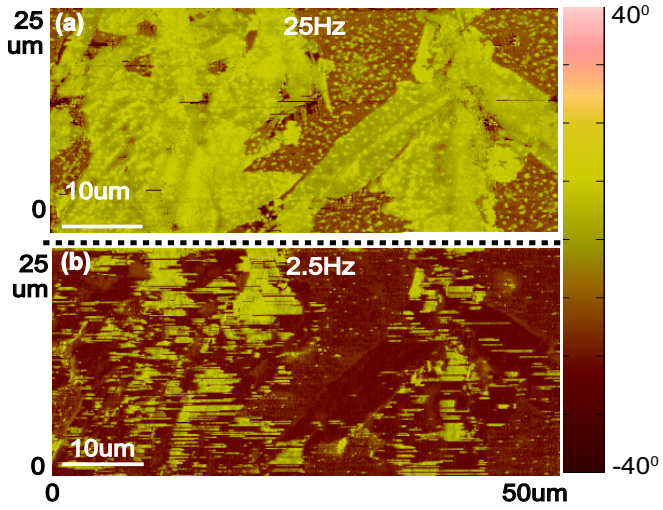

Figure 3.10: Phase images obtained using (a) the proposed AMLM-imaging technique at the scan rate of 25 Hz; and (b) the TM-imaging at the scan rate of 2.5 Hz, respectively.

around the desired values. Particularly, the amplitude of the averaged force was maintained below 10 nN during most of the imaging process, substantially lower than the averaged force (23 nN) exerted in the TM imaging at much lower scan rate of 2.5 Hz (compare Fig. 3.14 (b1) with Fig. 3.11(c1)), and the tapping amplitude ratio was well controlled around 20% throughout the whole image as shown in Figs. 3.14 (b2).

In summary, the experimental results demonstrated that the proposed AMLM-imaging technique increased the imaging speed by over 10 folds while substantially lowering the tip-sample interaction force during the imaging closely around the minimal level needed to maintain a stable tapping of the probe.

3.5 Conclusion

Adaptive Multi-loop mode (AMLM) imaging is proposed to substantially improve the speed of tapping-mode imaging. The proposed AMLM-imaging combines the cantilever deflection control in CM imaging with the tapping amplitude control in TM imaging, while maintaining the tapping motion of the probe as in the TM-imaging. First, both the z-piezo displacement and the TM-deflection are used to quantify the sample topography. Then, a feedback control loop of inner-outer loop structure is augmented to regulate the TM-deflection around the minimal-level for maintaining a stable probe tapping during the imaging, and a data-driven

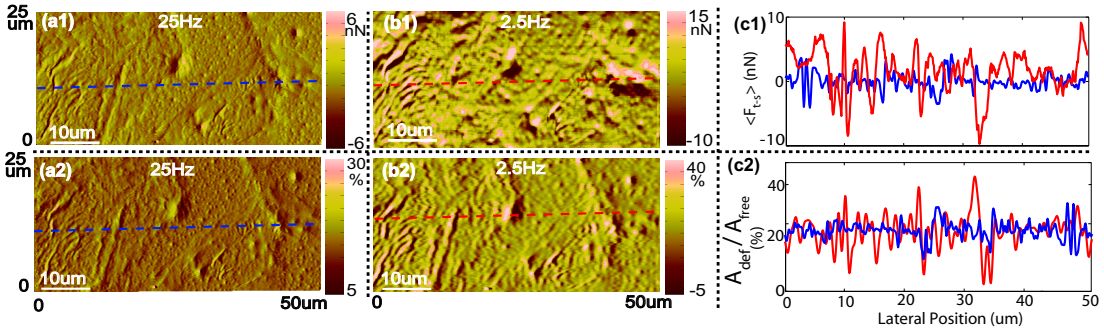

Figure 3.11: Comparison of the averaged probe-sample interaction force (i.e., the TM-deflection) (a1) by using the AMLM-imaging at 25 Hz to (a2) that by using the TM-imaging at 2.5 Hz, and (b1, b2) the images of the corresponding tapping-amplitude ratio ($A_{\text{def}}/A_{\text{free}}$); And the comparisons of (c1) the averaged force and (c2) the tapping amplitude ratio at the cross-section location marked in (a1) to (b2).

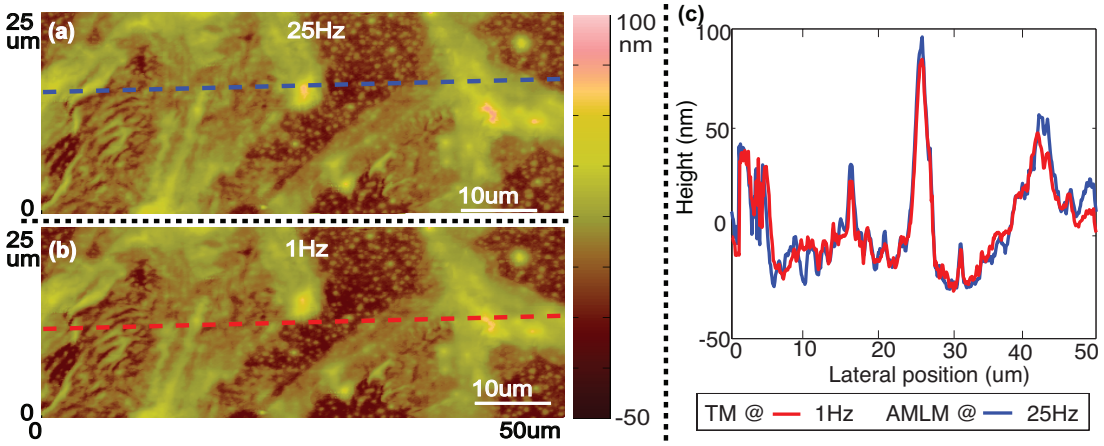

Figure 3.12: Comparison of the topography image obtained (a) using the proposed AMLM-imaging technique at the scan rate of 25 Hz; to (b) the TM-image at 1 Hz; and (c) comparison of the corresponding topography profile cross-sections.

online iterative learning feedforward controller is integrated to the feedback loop to further improve the tracking of the sample topography. The efficacy of the proposed AMLM-imaging was demonstrated by imaging a PtBA sample at different scanning speeds (25 Hz and 40 Hz) and different imaging sizes (50 μm and 20 μm). The comparisons of the sample topography tracking performances, the averaged tip-sample interaction forces, and the tapping-amplitude fluctuation between the proposed AMLM-imaging and the TM-imaging results showed that by using the proposed AMLM-imaging technique, the imaging speed was significantly increased by over 10 folds over large-size imaging, and the tip-sample interaction force was substantially reduced.

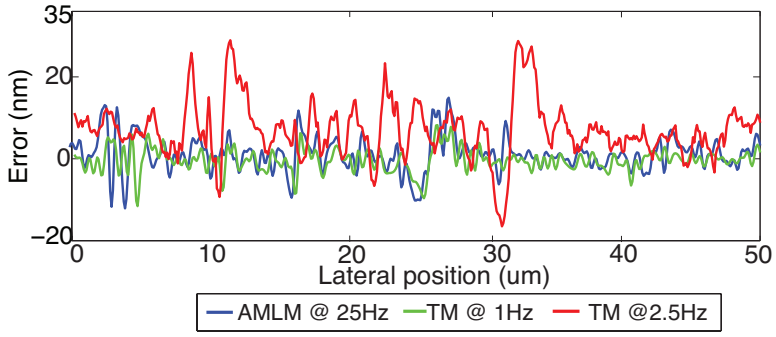

Figure 3.13: Comparison of the sample topography error obtained using the proposed AMLM-imaging at 25 Hz to those obtained by using the TM imaging at 1 Hz and 2.5 Hz (with respect to the sample topography at 1 Hz TM scan quantified via Eq. (3.4)).

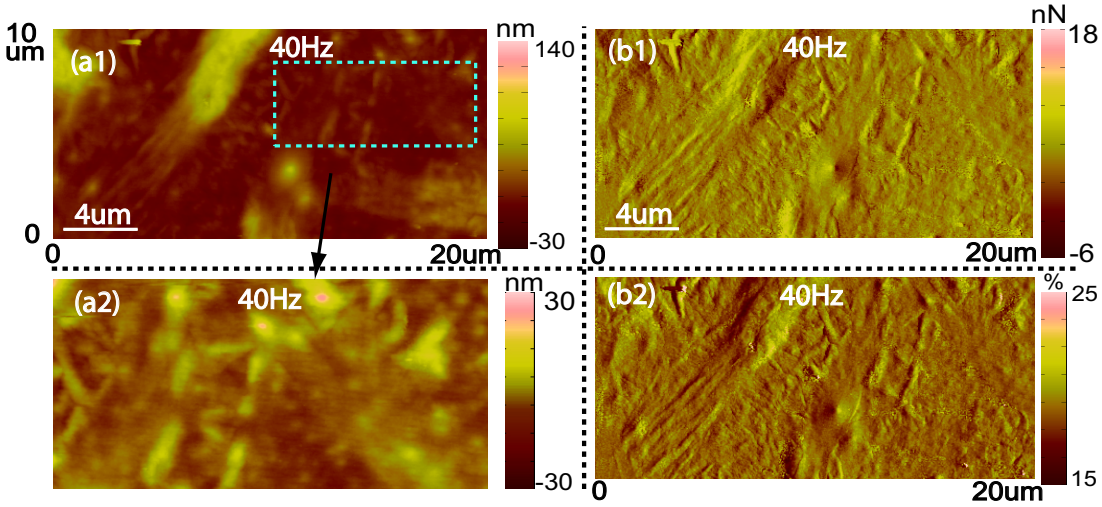

Figure 3.14: The sample topography image obtained using the proposed AMLM-imaging at (a1) 40 Hz and (a2) the zoomed-in image, and images of the corresponding (b1) averaged force and (b2) the tapping-amplitude ratio ($A_{\text{def}}/A_{\text{free}}$), respectively.

Chapter 4

Adaptive Scanning Near-Minimum Deformation Atomic Force Imaging of Soft Sample in Liquid: Live Mammalian Cell Imaging Example

Abstract

In this chapter, an adaptive mode of in-liquid topography imaging (AML) using atomic force microscopy (AFM) is proposed to replace the traditional contact-mode imaging on live biological samples in liquid by addressing the major concerns in both the speed and the force exerted to the sample. The speed of the traditional in-liquid contact-mode imaging is largely limited by the need to maintain precision tracking of the sample topography over the entire imaged sample surface, and large image distortion and excessive probe-sample interaction force occur during high-speed imaging. In this work, first, the sample deformation caused by the probe-sample interaction during imaging is analyzed and it is proposed to optimize the imaging speed based on the sample deformation estimated. Secondly, the sample topography which is quantified using the AFM piezo displacement and cantilever response is utilized in a gradient-based optimization method to adjust the cantilever deflection set-point for each scanline closely around the minimal level needed for maintaining a stable probe-sample contact, and a data-driven iterative feedforward control that utilizes a prediction of the next-line tracking is integrated to the topography feeedback loop to enhance the sample topography tracking. The proposed AML approach is demonstrated and evaluated by implementing it to image live human prostate cancer cells in cell culture medium.

4.1 Introduction

Due to the capability of recording dynamic processes with an unparalleled spatial resolution and operating in aqueous solution, topography imaging of cell surfaces is considered an important biological application of atomic force microscope (AFM) [5, 70, 71]. Particularly, contact mode AFM has been the most popular protocol for cell topography imaging because of the stable tip-sample interaction [1, 70]. Although it was marked earlier that the generally high scanning forces, between 1 and 30 nN, are considered to be necessary for cell cytoskeleton observation [70, 5, 72], under such an invasive approach, the scanned cells inevitably suffer various degrees of structural deformation or damage because of their intrinsic softness, which, even worse, may further provoke significant biological changes inside the cell since it is difficult to determine authenticity of the observed changes in cell morphology—either the changes are caused by dynamic cellular movement, or are artificial, induced by the tip-sample interaction during imaging. These issues raised by extensive tip-sample interaction force have become a significant technical hurdle for AFM cell topography imaging. Therefore, it is urgent that the AFM cell imaging approach needs to be re-investigated and improved for further exploration of AFM applications to study important dynamic cellular processes.

Conventionally, it has been suggested to reduce the cell structural deformation by substantially lowing the imaging speed, e.g., as low as 0.1 Hz [73, 1], however, it becomes more difficult to observe plasma membrane dynamics in living cells since time resolution is significantly reduced by such an operation. Although high speed AFMs have been developed to improve the image acquisition rate [74, 75], the workable sample imaging range (at all three dimensions) is substantially reduced by the new hardware and additional sample preparation is required to fit the imaging stages of these high speed devices [76, 77]. To capture fast movements of single molecule dynamics, a single line scan method has been applied, in which an AFM tip repeatedly scans a single line to record the height changes as a function of time [78, 79], however, such an approach lacks three-dimensional morphological information and cannot be utilized for cell topography study. To further extend AFM application in dynamic biological process study, an adaptive mode of in-liquid topography imaging (AML) using atomic force microscopy is proposed.

The proposed AML approach substantially increases the contact mode (CM) imaging speed on living cells, and maintains a near minimal interaction force. The improvements arise from the following four folds: (i) The imaging speed is optimized online based on real-time estimation of the sample deformation, the tip-sample interaction force, as well as the sample topography variation rate, as opposed to being fixed during the entire imaging process in the conventional AFM imaging; (ii) The sample topography is quantified using both the AFM z-axis piezo placement and the cantilever deflection as opposed to using only the piezo displacement in the conventional CM imaging; (iii) The sample topography quantified in (ii) is utilized in an iterative feedforward control scheme to track the sample surface as opposed to solely relying on the cantilever deflection in the conventional CM imaging; (iv) The deflection set-point is adjusted line-by-line closely around the minimal level needed for maintaining a stable tip-sample interaction as opposed to being fixed during the entire imaging process in the conventional AFM CM imaging.

The proposed AML technique was experimentally validated through imaging live human prostate cancer (PC-3) cells at the average scan rates of 0.41 Hz and 0.86 Hz. Compare to the conventional CM imaging, the AML technique was able to increase the imaging speed over four times while preserving the topography details of the live cells by accurate tracking of the sample topography. Therefore, the proposed AML approach substantially improves over the CM imaging on live cells in both the imaging speed and the sample topography tracking.

4.2 Deformation of Live Biological Samples during AFM Contact Mode Imaging in Liquid

In this section, the deformation of live biological samples (e.g., live cells) during contact mode (CM) AFM imaging in liquid is analyzed. During the topography imaging on soft samples in CM, the AFM tip constantly slides on the sample surface, and the stable tip-sample interaction is maintained by exerting a vertical force from the tip to the sample. As a consequence, the sample deforms both laterally and vertically as reaction to the lateral sliding motion of the tip and the vertical force applied, respectively, i.e.,

$$\vec{\delta}(t) = \vec{\delta}_z(t) + \vec{\delta}_l(t), \tag{4.1}$$

where $\vec{\delta}(t)$ is the deformation of the sample, $\vec{\delta}_z(t)$ and $\vec{\delta}_l(t)$ are the vertical and lateral deformation of the sample, respectively.

The vertical deformation of the sample, $\delta_z(t)$, can be quantified using the Hertz contact model as [1]

$$\delta_z(t) = \left[\frac{9F_z^2(t)(1-\nu^2)^2}{16R_cE^2}\right]^{\frac{1}{3}}, \tag{4.2}$$

where ν, E and R_c are the Poisson's ratio, the elastic modulus of the sample, and the AFM tip radius, respectively. $F_z(t)$ is the vertical tip-sample interaction force, which is equivalent to the multiplication of the cantilever spring constant (k_c) and the cantilever deflection ($d(t)$), i.e.,

$$F_z(t) = k_c d(t). \tag{4.3}$$

The lateral deformation of the sample, $\delta_l(t)$, caused by the sliding motion of the tip, however, is more complicated and closely related to the sample topography variation and the imaging speed. Next, we present a novel quantification of the lateral deformation of the sample.

4.2.1 Lateral Deformation of Biological Samples during CM Imaging

When the AFM probe moves along the cell surface with a preload applied, the mass of cell, $\delta m(t)$, "pushed" by the probe to move along with the tip at any time instant t can be quantified as:

$$\delta m(t) = \rho\lambda(l,t)\delta A(l,t), \tag{4.4}$$

where ρ, $\lambda(l,t)$ and $\delta A(l,t)$ are the density of the cell, the effective distance of the probe–cell interaction, and the local probe–cell interaction area segment around any point within the probe–cell contact area, i.e.,

$$\delta A(l,t) = \pi l \sin\alpha(l,t)\delta l, \tag{4.5}$$

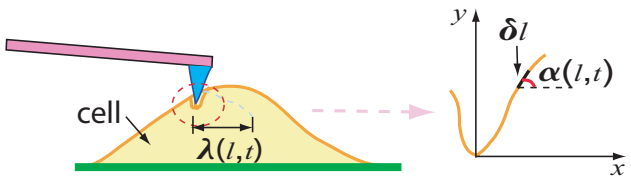

Figure 4.1: Sketch of probe–cell interaction.

where $\alpha(l,t)$ is the contact angle at location l, as shown in Fig. 4.1.

After time duration Δt, the momentum change of the probe-sample interaction system $\Delta P_{t\to t+\Delta t}$, i.e.,

$$\Delta P_{t\to t+\Delta t}(l) = \delta m(t+\Delta t)v(t+\Delta t) - \delta m(t)v(t), \tag{4.6}$$

where $v(\cdot)$ is the linear speed of the AFM tip on the cell surface. Eq. (4.6) can be simplified as:

$$\Delta P_{t\to t+\Delta t}(l) = \delta m(t)\Delta v(t) + \Delta\delta m(t)v(t), \tag{4.7}$$

where $\Delta\delta m(t) = \delta m(t+\Delta t) - \delta m(t)$, and $\Delta v(t) = v(t+\Delta t) - v(t)$.

Therefore, the "thrust", F_{th}, which results in the energy change of the cell, exerted from the AFM probe onto to cell is (i.e., $\Delta t \to 0$):

$$\delta F_{th}(l,t) = \frac{\Delta P(l)}{\Delta t} = \delta m(t)\dot{v}(t) + \delta\dot{m}(t)v(t). \tag{4.8}$$

Combining Eqs. (4.4) and (4.8),

$$\delta F_{th}(t) = \rho\lambda(l,t)[\delta A(l,t)\dot{v}(t) + \delta\dot{A}(l,t)v(t)] + \rho\dot{\lambda}(l,t)\delta A(l,t)v(t). \tag{4.9}$$

Hence, the stress of the live cell within the contact area, $\sigma_{tan}(t)$, is written as

$$\sigma_{th}(t) = \frac{F_{th}(t)}{\delta A(l,t)} = \rho\lambda(l,t)[\dot{v}(t) + \frac{\delta\dot{A}(l,t)}{\delta A(l,t)}v(t)] + \rho\dot{\lambda}(l,t)v(t). \tag{4.10}$$

Now, to consider the deformation of mass Δm (the total mass involved during the probe–cell interaction), the local strain, $\varepsilon_{tan}(t)$, at time t—caused by $\sigma_{tan}(t)$, can be quantified by using the viscoelastic contact model, i.e.,

$$\sigma_{th}(l,t) = E\varepsilon_{th}(l,t) + \eta\dot{\varepsilon}_{th}(l,t), \tag{4.11}$$

where η is the apparent elastic modulus and the apparent viscosity of cell. The solution of $\varepsilon_{tan}(t)$ for the above Eq. (4.11) is

$$\varepsilon_{th}(l,t) = \frac{\int_{t_0}^{t} e^{\frac{E}{\eta}\tau}\sigma_{th}(l,\tau)d\tau}{\eta e^{\frac{E}{\eta}t}}, \tag{4.12}$$

where t_0 is the time instant at which the probe–cell interaction starts to affect the point of interest on the cell, in another word, the probe–cell interaction affects the interested point from

t_0 to t till the AFM tip moves far away from Δm, i.e., $t \in [t_0, t_0 + \Delta t]$ for $\varepsilon_{th}(t)$, where Δt associates the maximum lateral deformation of the point of interest.

With the strain given in Eq. (4.12), the total lateral deformation of Δm is

$$\delta_{th}(l) = \varepsilon_{th}(l, t_0 + \Delta t)\delta l, \tag{4.13}$$

where δl can be chosen based on the image resolution, and $t = t_0 + \Delta t$ in Eq. (4.12).

Therefore, combining Eqs. (4.10) and Eq. (4.13),

$$\delta_{th}(l) = \frac{\int_{t_0}^{t_0+\Delta t} e^{\frac{E}{\eta}\tau}[\rho\lambda(l,\tau)[\dot{v}(\tau) + \frac{\dot{A}(l,\tau)}{A(l,\tau)}v(\tau)] + \rho\dot{\lambda}(l,\tau)v(\tau)]d\tau}{\eta e^{\frac{E}{\eta}(t_0+\Delta t)}}\delta l. \tag{4.14}$$

4.2.2 Quantification of the Parameters during Probe–Cell Interaction

To determine the effective distance $\lambda(l, t)$ of contact, we consider the force distribution inside the cell during contact mode imaging. At the location which is 13 times of the vertical deformation at the contact point—$\delta_z(l, t)$ (the indentation), the stress is reduced to only 3% of the stress within the contact area [80]. Therefore, $\lambda(l, t)$ can be determined as

$$\lambda(l, t) = 13\delta_z(l, t). \tag{4.15}$$

Furthermore, Δt—the loading time length of a certain location on the cell can be determined as:

$$\int_{t_0}^{t_0+\Delta t} v(t)dt = \lambda(t_0). \tag{4.16}$$

Therefore, the overall deformation, δ_{tot}, of a certain location on the live cell along the vertical direction is

$$\delta_{tot}(t) = \delta_z(t) + \nu\delta_{th}(t). \tag{4.17}$$

Next, we validate the deformation quantification through experiments by imaging on live human prostate cancer cells at different imaging speed, and comparing the deformation caused by high speed imaging with the result quantified using the above discussion.

4.2.3 Experimental Implementation and Discussion

The above deformation analysis was validated through imaging on prostate cancer (PC-3) cells at the scan size of 50 μm. PC-3 cells (ATCC, Rockville, MD, USA) were grown in RPMI-1640

culture medium containing 10% FBS that was supplemented with penicillin (100 units/ml)-streptomycin (100 μg/ml) and L-glutamine (300 μg/ml). To accommodate the AFM measurements, the PC-3 cells were seeded at a density of 0.2×10^5 cells/ml in 60 mm tissue culture dishes (5 ml/dish) and incubated for 24 h before imaging. Both the cells and the cantilevers were thermally equilibrated at $\sim 37^{\circ}\mathrm{C}$ for 40-60 mins prior to imaging to minimize the cantilever drifts.

The experiments were conducted on a commercial AFM (Dimension Icon, Bruker AXS Inc.) on which both the drive of the piezo actuators and all of the sensor signals including the deflection and the piezo displacement sensor signals can be directly accessed. All of the signals were acquired through a computer-based data acquisition system (NI-6259) under the Matlab xPC-target environment. Precise tracking in the lateral x-y axes scanning was achieved using PI feedback control. The cells were imaged at two different speed: 0.1 Hz (10 μm/s) and 0.5 Hz (2 μm/s) at the same location. The topography images of PC-3 cells at these two different imaging speed are shown in Figs. 4.2.

The deformation difference of the imaged PC-3 cells caused by the AFM probe at the two imaging speeds were directly computed by subtracting the topography data of the 0.1 Hz image from that of the 0.5 Hz scan, as shown in Fig. 4.3(a). Note that this operation is eligible as the sample deformation is linearly affected by the imaging speed as shown in Eq. (4.14) and the effect of probe acceleration can be ignored (since commercial CM images at constant speed). We also computed the deformation difference based on the analysis above (Eqs. (4.2), (4.14), and (4.17)). To simplify the calculation, the elastic model of the cell mechanics was used instead of the viscoelastic one, and the elastic modulus and the Poisson's ratio of PC-3 cells was chosen as $E = 4kPa$ and $\nu = 0.5$, respectively. The estimated deformation difference is shown in Fig. 4.3(b).

Comparison between the sample deformation obtained through the imaging result and the deformation analysis proposed validated the formulation of cell deformation caused during CM AFM imaging. Specifically, the deformation difference (caused by different imaging speeds) computed using the proposed model (Fig. 4.3(b)) is 27.4% different from that directly quantified from the experimental data (Fig. 4.3(a)). The percentage was the RMS value of the point-by-point difference between this two figures. The 27% percent difference may be caused

by the estimation uncertainties, e.g., the inhomogeneity of cells, the estimation error due to elastic contact approximation. However, considering the estimation uncertainties, accuracy of over 70% demonstrated that the proposed deformation formulation was close to the experimental measured result, and thereby is valid for biological sample deformation analysis. Based on the proposed deformation formulation, we have developed a novel CM imaging scheme—adaptive mode of in-liquid topography imaging, to optimize the imaging speed while minimizing the sample deformation.

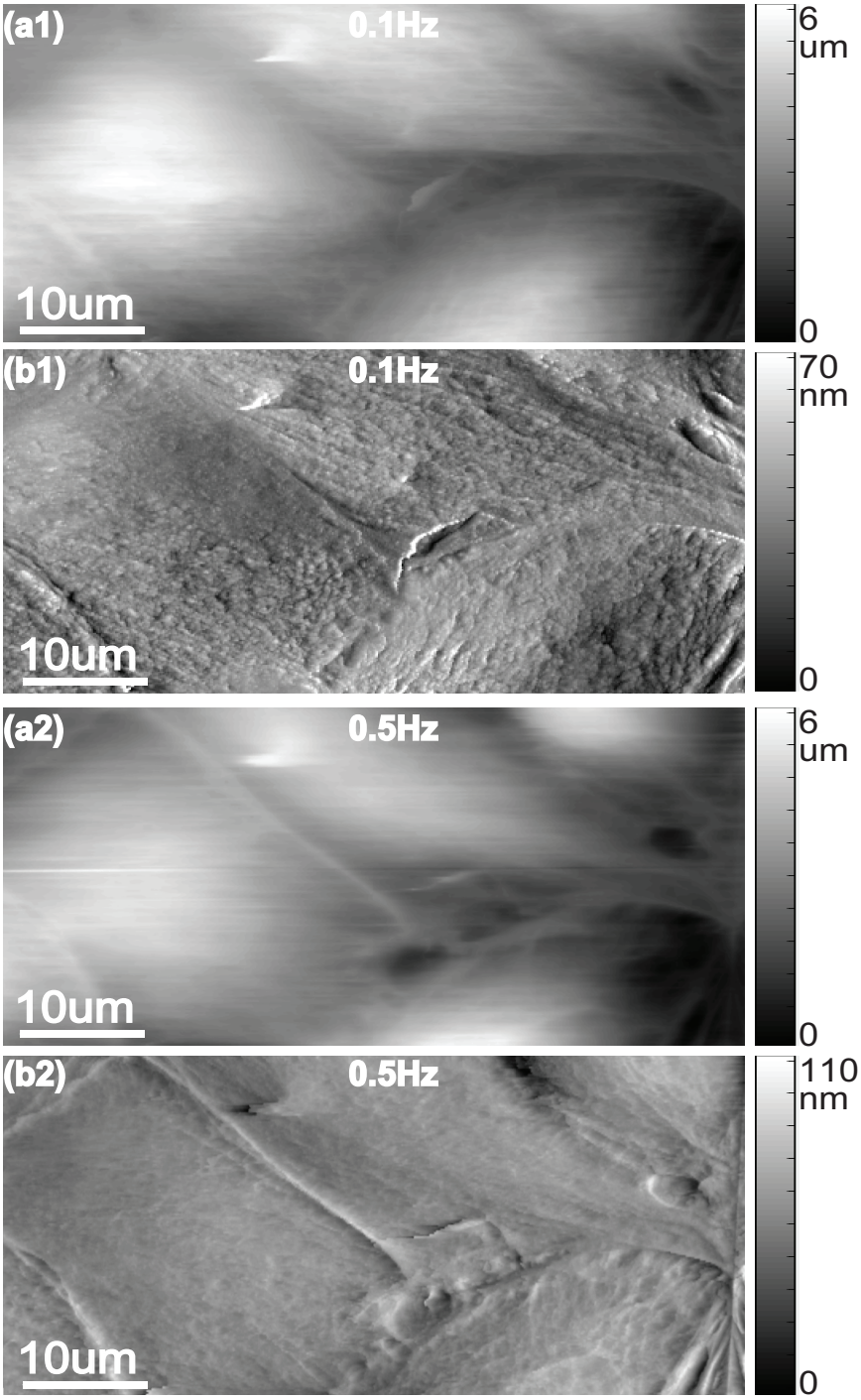

Figure 4.2: CM images of PC-3 cells at the imaging speed of 0.1 Hz: (a1) height, and (b1) deflection; 0.5 Hz: (a2) height, and (b2) deflection.

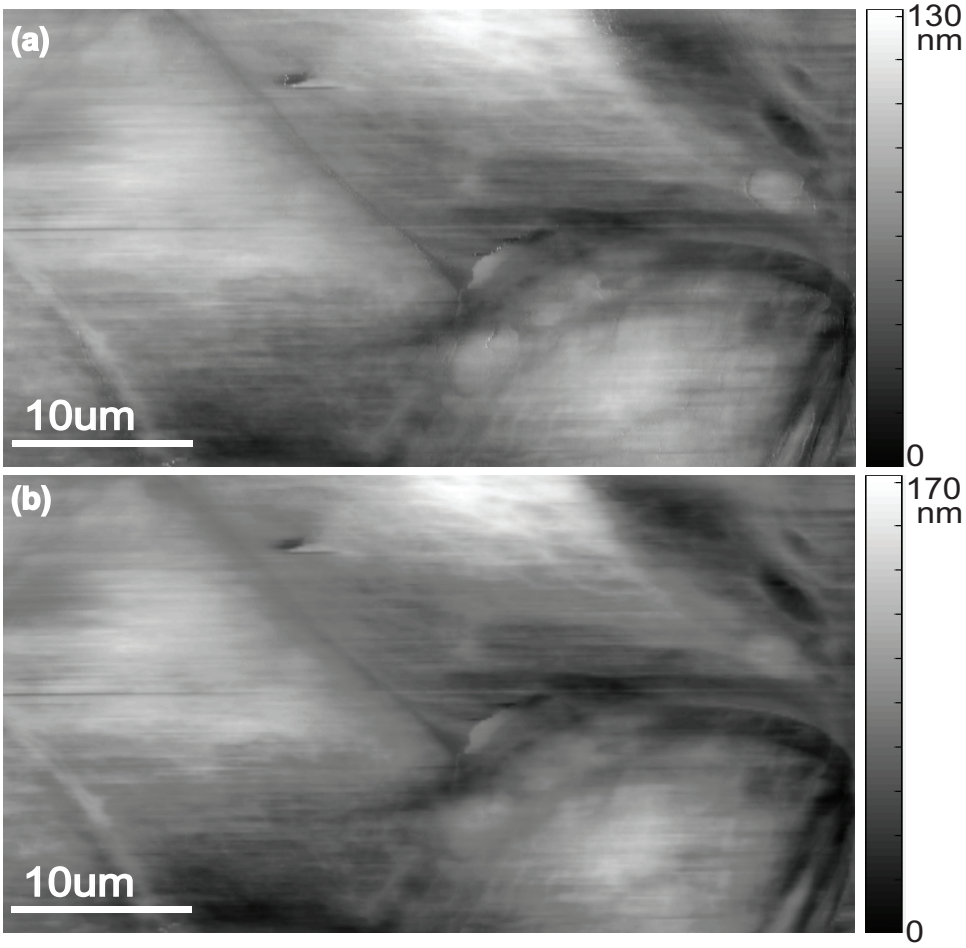

Figure 4.3: Sample deformation computed (a) based on experimental collected data from Figs. 4.2, and (b) using Eqs. (4.2), (4.14), and (4.17).

4.3 Adaptive Scanning with Near-Minimum Deformation

The proposed adaptive mode of in-liquid topography imaging (AML) consists of two main components: First, an online scanning speed optimization scheme is developed so that the lateral deformation of the sample caused by the scanning motion of the AFM tip is minimized; Secondly, during the scanning, the vertical deformation of the sample is minimized by utilizing a gradient-based optimization of the deflection set-point and a data driven iterative feedforward control scheme to improve the sample topography tracking.

4.3.1 Adaptive Scanning towards Minimum Lateral Deformation

As discussed in Sec. 4.2, the lateral deformation of the sample, $\delta_l(t)$, caused by the sliding motion of the tip during CM imaging in liquid is closely related to the sample topography variation and the imaging speed. Specifically, the biological sample is disturbed by the sliding motion of the AFM tip during imaging, and a certain portion of the sample moves with the tip (e.g., cytoplasm of cells). Therefore, the lateral force exerted to the sample, $F_l(t)$, can be considered as the "thrust" generated by the tip (a simplified form of the lateral force in Sec. 4.2), i.e.,

$$F_l(t) = \dot{m}(t)|\dot{x}(t)| = |\dot{x}(t)| \left[\rho \frac{d}{dt} \int_0^{\delta_z(t)} \int_{-r}^{r} \bigtriangledown h(x)\psi(z) dx dz \right], \tag{4.18}$$

where $|\dot{x}(t)|$ is the scanning speed, ρ and r are the sample mass density and the tip-sample contact radius, respectively. $\bigtriangledown h(x)$ and $\psi(z)$ are the sample topography (height) gradient along the scanning direction and the tip contour profile function, respectively. Given the monotonic relation between deformation and force, the lateral deformation of the sample is closely related to the imaging speed and the sample topography gradient as following,

$$\delta_l(t) \propto F_l(t) = |\dot{x}(t)| \left[\rho \frac{d}{dt} \int_0^{\delta_z(t)} \int_{-r}^{r} \bigtriangledown h(x)\psi(z) dx dz \right]. \tag{4.19}$$

As clearly shown in Eq. (4.19), the lateral deformation of the sample increases with the increases of both the imaging speed and the sample topography gradient. Furthermore, due to the feedback control implemented in AFM imaging, when the imaging speed is increased, the AFM tip fails to track the sample topography. As a result, the tip-sample interaction force increases dramatically, which further leads to sever sample deformation and unreliable sample

topography quantification [1, 59]. Conventionally, it is suggested to choose the lowest scan speed (0.1 Hz) for live cell imaging, and in return, it takes more than one hour to obtain a topography image. Moreover, this unnecessary time consumption limits the capability of AFM imaging in capturing dynamic evolution of soft samples, such as cell morphological change under different chemical conditions. Therefore, combining Eqs. 4.2, 4.3 and 4.19, we proposed to online optimize the scanning speed to obtain topography images with desired quality and minimum imaging time as following,

$$|\dot{x}(t)| = \frac{\dot{x}^*}{1+\kappa}\left(\left|\frac{\bigtriangledown h^*}{\bigtriangledown h(t-t_s)}\right| + \kappa\left|\frac{d^*}{d(t-t_s)}\right|\right), \quad t_s: \text{ sampling period} \tag{4.20}$$

where κ is the normalization ratio, $\bigtriangledown h^*$ and d^* are the threshold values of the sample topography gradient and the cantilever deflection to ensure imaging quality, respectively. Note that lower and upper bounds of $|\dot{x}(t)|$ must be applied during the imaging in case that the computed scanning speed is extreme. Specifically, since the lateral imaging resolution is generally determined by the geometrical configuration of the AFM tip, the lowest scanning speed, $\dot{x}_{\min}$, can be determined based on the AFM tip radius R_c [1]:

$$\dot{x}_{\min} = 0.2R_t \times f_{sl}, \tag{4.21}$$

where f_{sl} is the lowest sampling frequency, and usually $f_{sl} = 100$Hz for live human cell imaging. Practically, $\dot{x}_{min}$ is the lowest speed for CM imaging which leads to the best imaging quality. Unnecessary time consumption may be caused during the imaging if the tip speed is lower than $\dot{x}_{min}$ since the imaging resolution and quality cannot be further improved by slowing down the scanning speed. Furthermore, the upper limit of the]scanning speed is set as $\dot{x}_{\max}$—a practically tuned value for each sample to ensure that the sample will not be ruined during imaging.

Combine both the upper and lower limits of the scanning speed, the optimal scanning speed, $|\dot{x}(t)|$, is set as,

$$|\dot{x}(t)| = \begin{cases} \dot{x}_{\min} & \text{if } |\dot{x}(t)| \le \dot{x}_{\min} \\ \dot{x}_{\max} & \text{if } |\dot{x}(t)| \ge \dot{x}_{\max} \\ |\dot{x}(t)| & \text{else} \end{cases} \tag{4.22}$$

Finally, to construct the zigzag-shaped lateral scanning path, the imaging velocity is defined as following:

$$\begin{aligned} \dot{x}(t) &= \mathscr{D}(t)|\dot{x}(t)|, \\ \text{with } \mathscr{D}(t) &= \begin{cases} +1 & \text{when } t = 0 \\ \text{sgn}\left[\mathscr{D}(t-t_s) * (\hat{x} - |x(t-t_s)|)\right] & \text{else,} \end{cases} \end{aligned} \tag{4.23}$$

where $\hat{x}$ is the scanning limit, and $x(\cdot)$ is the scanning position.

The perpendicular scanning velocity is regulated based on $|\dot{x}(t)$ as:

$$\dot{y}(t) = g_{xy}|\dot{x}(t)|, \tag{4.24}$$

where g_{xy} is the x-to-y direction conversion gain, and determined by the y-scanning size and total number of scanlines.

4.3.2 Adaptive Scanning towards Minimum Vertical Deformation—True-Topography Tracking via Iterative Feedforward Control of the Piezo Actuator

As explicitly shown in Eqs. 4.2 and 4.3, to minimize the vertical deformation of the sample is equivalent to minimize the vertical tip-sample interaction force—the cantilever deflection. Therefor, an online iterative feedforward control approach with deflection set-point optimization is integrated to the sample topography tracking system to minimize the tip-sample interaction force and enhance the sample topography tracking performance .

We propose a gradient-based optimization scheme to adjust the deflection set-point line-by-line. Specifically, the deflection set-point of the $k+1^{th}$ scanline, $d_{\text{set,k+1}}$, is updated/adjusted from that of the previous line, $d_{\text{set,k}}$, by using the difference between minimum of the predicted deflection at the $k+1^{th}$ scanline, $\min(\hat{d}_{k+1}(t))$, and the minimum deflection/force needed to maintain the stable repulsive tip-sample interaction, D^*_{min} (i.e., a lower bound),

$$\begin{aligned} d_{\text{set,0}} &= d_{\text{set,org}}, \\ d_{\text{set,k+1}} &= d_{\text{set,k}} - [\min(\hat{d}_{\text{k+1}}(t)) - D^*_{\text{min}}], \quad k \geq 1 \\ \text{with} \quad \hat{d}_{\text{k+1}}(t) &\triangleq d_{\text{k}}(t) + \lambda[(d_{\text{k}}(t) - d_{\text{k-1}}(t))], \quad \text{for} \quad t \in [0,\, T_{\text{scan}}], \end{aligned} \tag{4.25}$$

where T_{scan} is the scanning period, $d_{\text{set,org}}$ is the original deflection set-point chosen *a priori* to the imaging process, and $\lambda \in [0, 1]$ is the gradient factor, and can be tuned to improve the

imaging quality.

Given the line-to-line topography variation of the sample is small with enough scanlines per image, the topography of the $k+1^{th}$ scanline can be estimated as that of the k^{th} scanline ($h_{\mathrm{k}}(x)$), and to further reduce the topography tracking error, the next-line topography is modified using the deflection error of the k^{th} line as

$$h_{\text{ffd,k+1}}(x) = h_{\mathrm{k}}(x) + \alpha[d_{\mathrm{k}}(x) - d_{\text{set,k}}], \text{with } \; h_{\mathrm{k}}(x) = z_{\mathrm{k}}(x) + [d_{\mathrm{k}}(x) - d_{\text{set,k}}], \qquad (4.26)$$

where α is the correction factor, T_{scan} is the scanning period, and $z(\cdot)$ is the AFM z-axis piezo actuator displacement. Due to the compliance of the cantilever and the cantilever fixture (connecting the cantilever to the piezo actuator), time delay exists in the response of the cantilever deflection to the sample topography change. The above modified desired trajectory—for the feedforward control input to track—helps the AFM piezo actuator to drive the cantilever to respond in advance (i.e., pre-actuate) to the topography variation, thereby reducing the amplitude of the deflection variations. The correction factor α can be tuned based on the estimated height of the sample surface features.

We propose to track the modified next-line sample topography profile, $h_{\text{ffd,k+1}}(t)$, using a data-driven iterative feedforward control augmented to the conventional AFM feedback control. Particularly, the feedforward control input is obtained by implementing the following high-order modeling-free difference-inversion-based iterative-control (HOMDIIC) algorithm [66] online,

$$\begin{aligned}
U_{\text{ff,0}}(j\omega) &= 0, \\
U_{\text{ff,1}}(j\omega) &= \frac{U_{\text{ff+fb,0}}(j\omega)}{Z_0(j\omega)} H_{\text{ffd,1}}(j\omega), \\
U_{\text{ff,k+1}}(j\omega) &= U_{\text{ff,k}} + \lambda \frac{U_{\text{ff+fb,k}}(j\omega) - U_{\text{ff+fb,k-1}}(j\omega)}{Z_{\mathrm{k}}(j\omega) - Z_{\text{k-1}}(j\omega)} e_{\mathrm{k}}(j\omega), \quad k \geq 1 \\
e_{\mathrm{k}}(j\omega) &= H_{\text{ffd,k+1}}(j\omega) - Z_{\mathrm{k}}(j\omega)
\end{aligned} \qquad (4.27)$$

where '$j\omega$' denotes the Fourier transform of the corresponding signal, λ is a pre-chosen constant to ensure the convergence of the iteration, and $U_{\text{ff+fb,k}}(\cdot)$ and $Z_{\mathrm{k}}(\cdot)$ are the total control input (feedback+feedforward) applied to the z-piezo actuator (i.e., $U_{\text{ff+fb,k}}(j\omega) = U_{\text{ff,k}}(j\omega) + U_{\text{fb,k}}(j\omega)$ and the z-piezo displacement measured on the k^{th} scan line, respectively, and $H_{\text{ffd,k+1}}(\cdot)$ denotes the desired trajectory that the z-piezo needs to track at the $k+1^{th}$ scanline.

Finally, to avoid noise being fed back into the closed-loops via the feedforward channel, the feedforward control input, $U_{\text{ff,k+1}}(\cdot)$, is passed through a zero-phase low-pass filter $Q(j\omega)$,

$$\hat{U}_{\text{ff,k+1}}(j\omega) = Q(j\omega)U_{\text{ff,k+1}}(j\omega) = Q_b(j\omega)C_{\text{lead}}(j\omega)U_{\text{ff,k+1}}(j\omega), \tag{4.28}$$

where $Q_b(j\omega)$ and $C_{\text{lead}}(j\omega)$ are a low-pass filter and a phase-lead compensator, respectively. As the entire next-line feedforward control input is known a priori, the above noncausal zero-phase filter can be implemented online.

In summary, as shown in Fig. 4.4, the proposed AML imaging consists of: (1) an online scanning speed optimization based on sample topography variation and tip-sample interaction force to minimized the lateral sample deformation, and (2) a gradient based deflection set-point optimization scheme and a data driven iterative feedforward control approach to vertical sample deformation minimization.

4.3.3 Experimental Implementation and Discussion

The AML imaging technique was demonstrated through imaging on prostate cancer (PC-3) cells at the scan size of 50 μm. PC-3 cells (ATCC, Rockville, MD, USA) were grown in RPMI-1640 culture medium containing 10% FBS that was supplemented with penicillin (100 units/ml)-streptomycin (100 μg/ml) and L-glutamine (300 μg/ml). To accommodate the AFM measurements, the PC-3 cells were seeded at a density of 0.2×10^5 cells/ml in 60 mm tissue culture dishes (5 ml/dish) and incubated for 24 h before imaging. Both the cells and the cantilevers were thermally equilibrated at $\sim 37^{\circ}$C for 40-60 mins prior to imaging to minimize the cantilever drifts.

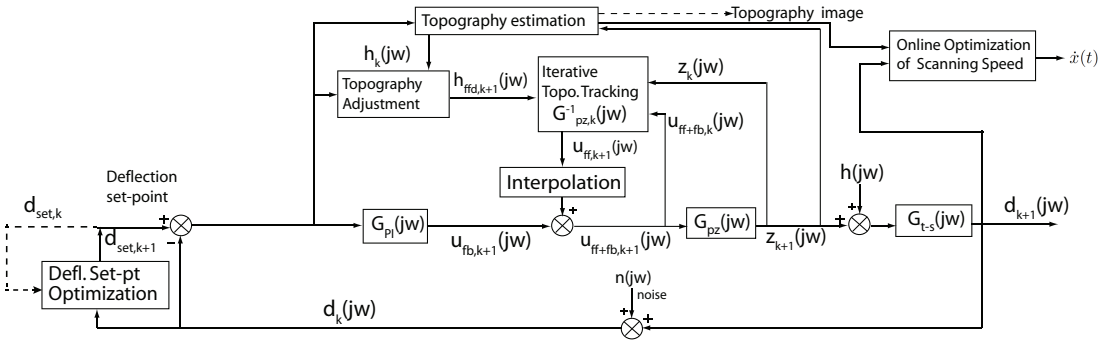

Figure 4.4: Schematic block diagram of the AML imaging.

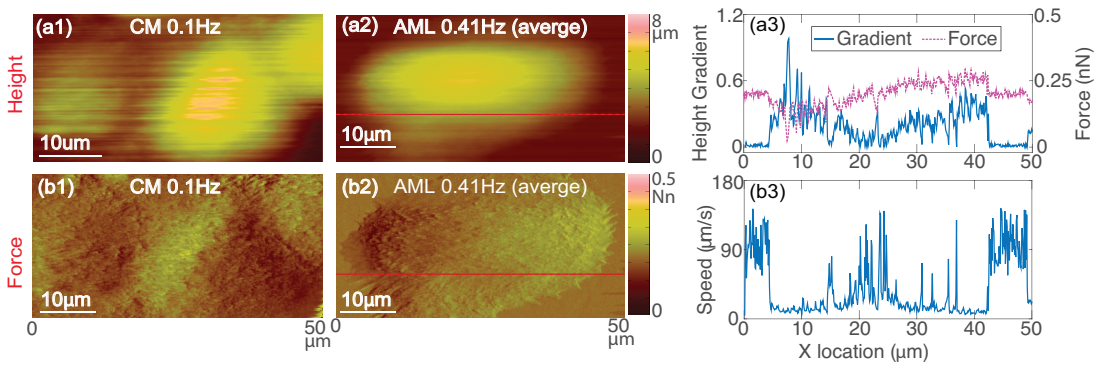

Figure 4.5: Comparison of the cell images obtained using: (a1)-(b1) the conventional CM at the scan rate of 0.1Hz; (a2)-(b3) the proposed AML imaging at the average scan rate of 0.41Hz; and (a3) the sample height gradient $\bigtriangledown h$ and the vertical tip-sample interaction force, (b3) the x-scanning speed of at the location of the cross section marked in (a2)-(b2).

Implementation of the AML Imaging Technique

The experiments were conducted on a commercial AFM (Dimension Icon, Bruker AXS Inc.) on which both the drive of the piezo actuators and all of the sensor signals including the deflection and the piezo displacement sensor signals can be directly accessed. All of the signals were acquired through a computer-based data acquisition system (NI-6259) under the Matlab xPC-target environment. Precise tracking in the lateral x-y axes scanning was achieved using PI feedback control. The x-scanning parameters were chosen as $\dot{x}^* = 25$ μm/s, $d^* = 15$ nm, and $\bigtriangledown h^* = 0.4$. Due to low signal-to-noise ratio for in-liquid imaging (since the cantilever deflection needs to be maintained small to prevent cell damage), the deflection set-point was chosen as $d_{\text{set}} = D^*_{\text{min}}$ =15 nm without adjustment during the experiment (the efficacy of the deflection set-point optimization is demonstrated in [77]).

The proposed AML imaging result is compared to that obtained using commercial CM imaging at the scan rates of 0.1 Hz and 0.3 Hz. Specifically, the cell images obtained using the conventional CM at the scan rate of 0.1 Hz is compared with the AML images obtained at the average scan rate of 0.41 Hz in Fig. 4.5. With the imaging speed increased by four times, the vertical tip-sample interaction force during the AML imaging was only 10% bigger than that in the 0.1 Hz CM imaging, and the imaging quality was well preserved (compare the detail feature of the cells in the force images). As an example, the x-scanning speed at the location of the cross section in the AML images are also shown in Fig. 4.5 (b3), which is determined

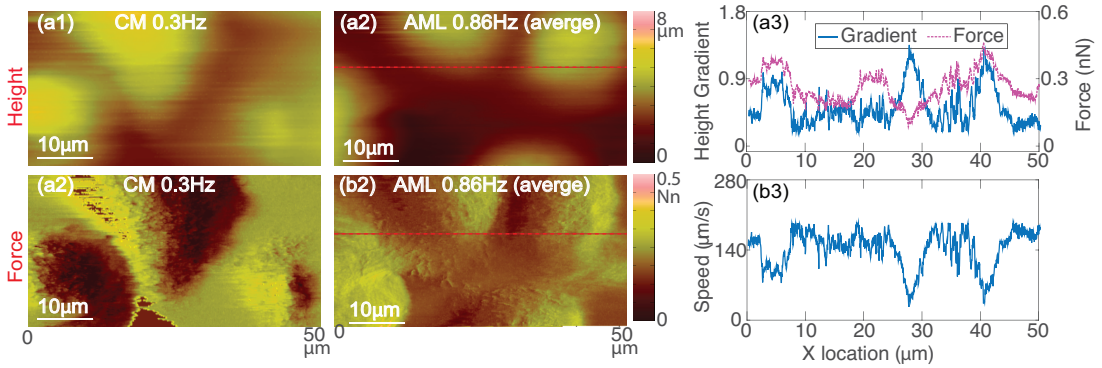

Figure 4.6: Comparison of the cell images obtained using: (a1)-(b1) the conventional CM at the scan rate of 0.3Hz; (a2)-(b3) the proposed AML imaging at the average scan rate of 0.86Hz; and (a3) the sample height gradient $\bigtriangledown h$ and the vertical tip-sample interaction force, (b3) the x-scanning speed of at the location of the cross section marked in (a2)-(b2).

by both the sample height gradient $\bigtriangledown h$ and the tip-sample interaction force (Fig. 4.5 (a3)) according to Eq. 4.20. We further pushed the scanning speed of the AML imaging by increasing the upper limit of the scanning speed $\dot{x}_{\max}$. The average scan rate of the AML images shown in Fig. 4.6 was 0.86 Hz. Compare to the CM imaging at the constant scan rate of 0.3 Hz (see Fig. 4.6 (a1)-(b1)), the vertical tip-sample interaction force during 0.86 Hz AML imaging was 40% lower, and the imaging quality was significantly improved at the same time: the topography details of the cell membrane were clearly captured and preserved by the proposed AML imaging technique, however, the cells were severely scratched by the AFM tip due to excessive tip-sample interaction force during CM imaging at 0.3 Hz, and the image was distorted at the same time. Furthermore, the comparison between Fig. 4.5 and Fig. 4.6 demonstrated that when the averaged scanning speed is increased by more than 8 times, the AML imaging is still capable of maintaining the imaging quality when comparing with the CM image at the scan rate of 0.1 Hz.

Therefore, the experimental result demonstrated that the proposed AML imaging technique increased the scan speed by over 8 folds using real-time adaptive imaging speed optimization while maintaining the imaging quality and substantially lowering the tip-sample interaction force.

4.4 Conclusion

An adaptive mode of in-liquid topography imaging (AML) is proposed to substantially improve the speed of contact mode (CM) imaging of live cells. In the proposed AML, the imaging speed is optimized online based on real-time estimation of the sample deformation, the tip-sample interaction force, as well as the sample topography variation rate, and the sample topography is quantified using both the AFM z-axis piezo placement and the cantilever deflection and then utilized in an iterative feedforward control scheme to track the sample surface. To minimize the probe-sample interaction force, the deflection set-point is adjusted line-by-line closely around the minimal level needed for maintaining a stable tip-sample interaction. The AML was experimentally validated through imaging live human prostate cancer (PC-3) cells at the average scan rates of 0.41 Hz and 0.86 Hz. Compare to the conventional CM imaging, the AML technique was able to increase the imaging speed over four times while preserving the topography details of the live cells by accurate tracking of the sample topography.

Chapter 5

Accurate Indentation Quantification in Broadband and In-liquid Nanomechanical Measurement of Soft Material Using Scanning Probe Microscopy

Abstract

In this chapter, we present a control-based approach to broadband and in-liquid nanomechanical property quantification of soft material using AFM. Accurate indentation measurement is essential to probe-based material property characterization as the force exerted and the indentation generated are the two most important physical variables measured in the process. Large measurement errors, however, occur when the measurement frequency range becomes large (i.e., broadband) and/or the measurement is conducted in liquid. Such large measurement errors are generated due to the inability of the conventional method to account for the the difference between the SPM z-axis piezo actuator displacement and the vertical displacement of the cantilever at its fixed-end, the lateral-vertical coupling-caused cantilever motion when the measurement frequency range becomes large, and the relative probe acceleration and the hydrodynamic force effects. We propose a control-based approach to address these challenges to overcome the limits of the conventional method. The proposed approach is demonstrated through experiments to measure the viscoelastic properties of a Polydimethylsiloxane (PDMS) sample over a broad frequency spectrum, and rate-dependent elastic modulus of human cervix cancer cells in liquid.

5.1 Introduction

In this chapter, a control-based approach to achieve accurate nanoindentation quantification in broadband and in-liquid nanomechanical measurement of soft sample using atomic force

microscope (AFM) is proposed. Indentation-based approach has been utilized to measure mechanical properties of a wide variety of soft materials at nano scale, ranging from polymers [17, 18, 19, 20], live biomaterials [21, 22, 23] to food product [24]. By measuring the excitation force applied and the indentation generated in the sample, mechanical properties such as the elastic modulus and/or the complex modulus (for viscoelastic materials) of the sample can be quantified (through a contact model of the probe-sample interaction, e.g., the Hertzian model or the DMT model) [21, 1, 25]. As the force and the indentation serve as the input and output in the contact model, respectively, accuracy of the indentation quantification dictates that of the nanomechanical properties measured. Therefore, accurate indentation measurement is crucial to nanomechanical property measurement of materials.

The conventional indentation measurement is limited and erroneous in broadband and in-liquid nanomechanical property quantification. Currently on almost all commercial AFM systems, the indentation is obtained by comparing the force-distance curves [1] measured on the soft sample and that on a hard reference sample under a constant force load-unload rate [1, 26]. This method (to quantify the indentation) is adequate when the measurement is quasi static (with constant force load/unload rate) and the load/unload rate is low—so that the AFM instrument dynamics is not excited and the cantilever base displacement (i.e., the cantilever displacement at its fixed end) equals to the z-axis piezo actuator displacement (measured by the z-axis sensor). As the measurement load/unload rate increases towards the resonances of the AFM instrument dynamics, the dynamics of the cantilever fixture (connecting the cantilever to the piezo actuator) can be excited [1], and the lateral-vertical cross-axis dynamics coupling effect becomes pronounced [27, 28]. Consequently, large measurement errors are induced when using the z-axis sensor to directly measure the cantilever base displacement, as the cantilever-base displacement is largely different from the z-axis sensor signal, and the cross-axis coupling dynamics induces extraneous motion of the cantilever in z-axis. Therefore, techniques need to be developed to accurately measure the indentation to achieve rapid, broadband nanomechanical properties quantification.

Furthermore, although the measurement frequency range for in-liquid nanomechanical quantification is generally below the resonance of the instrumental dynamics, the relative acceleration of the cantilever probe (with respect to the fixed-end of the cantilever (called the *the*

relative probe acceleration) becomes pronounced and substantially effects the indentation generated. The conventional indentation is also plagued by the uncertainty in determining the probe-sample contact point [29] and the hydrodynamic force effect [30, 31]. Although the contact-point uncertainty can be alleviated through the use of a reference sample [1], and the hydrodynamic force effect might be accounted for by quantifying it via experiment [31], these efforts are still limited to ultra-low force load rate, and the relative probe acceleration dominates over the hydrodynamic force (i.e., over an order of magnitude larger) when the force load rate is higher than $\sim$0.1 Hz for for most live cells. Therefore, to achieve accurate indentation quantification of live cell, the conventional indentation measurement needs to be replaced.

The main contribution of this chapter is the development of a control-based indentation measurement approach to achieve accurate nanoindentation quantification during broadband and in-liquid nanomechanical measurement. First, based on the analysis of the adverse effects of the cantilever-fixture dynamics and the lateral-vertical cross-axis coupling dynamics, an approach to individually quantify these two adverse effects through experiments is proposed. Secondly, the cantilever dynamics during the nanomechanical quantification is modeled and analyzed by taking into account the relationships between the measurement frequency range and the bandwidth of both the piezo actuator and the cantilever. Using the cantilever dynamics model, we propose to measure the indentation by accurately tracking the *same* excitation force profile (i.e., the same cantilever vertical deflection) on the soft sample and on a hard reference sample, and obtaining the indentation from the difference of the cantilever base displacements obtained on both samples. Control techniques such as the recently developed modeling-free inversion-based iterative control (MIIC) technique [32] is utilized to quantify both the cantilever-fixture dynamics and the cross-axis coupling dynamics, and to achieve accurate tracking of the excitation force of rich frequency spectrum. The proposed method is illustrated by implementing it to the broadband viscoelasticity measurement of different polymer samples and live cells in experiment.

This chapter is organized in the following format. The proposed control-based indentation quantification in broadband nanomechanical quantification and its experimental validation are presented in Section 2, and then followed by the in-liquid nanoindentation quantification and the experiment results on live human cell viscoelasticity measurements in Section 3. Finally,

the conclusion is given in Section 4.

5.2 A Control-based Approach to Accurate Nanoindentation Quantification in Broadband Nanomechanical Measurement using Atomic Force Microscopy

5.2.1 Limits of Conventional AFM Indentation Quantification for Broadband Measurement

The uniqueness of AFM for measuring nanoscale material properties and/or force interactions arises from the capability of AFM of applying excitation force with controlled amplitude at desired location, and measuring the properties/force, at the location, with nanometer and piconewton spatial and force resolutions, respectively [1]. Specifically, when measuring nanomechanical properties of a soft sample, a micro-fabricated cantilever with a nanometer size probe on its free end is driven by a piezo actuator to push upon the soft sample surface under a constant force load/unload rate (see Fig. 5.1(a)). Then a force of constant load/unload rate is exerted onto the sample surface via the cantilever probe, and the applied force and indentation generated (i.e., the deformation of the sample surface) are measured [81]. Therefore, the applied force and the indentation generated are the two most important variables that must be quantified in nanomechanical property characterization using AFM [1], and the accuracy of the indentation measurement is crucial to that of the nanomechanical properties to be measured. In specific, the nanomechanical properties of the soft sample are obtained from the measured interaction force and indentation via an appropriate contact mechanics model of the probe-sample interaction [1, 17]. For example, when the deformation is small and the adhesion force is negligible, the complex compliance of the sample J(t) can be obtained from the following Hertzian model [1, 17]

$$\Delta_z(t)^{\frac{3}{2}}(t) = C_1 \int_0^t J(t-\tau)\dot{F}(\tau)d\tau, \tag{5.1}$$

where $F(t)$ is the tip sample interaction force, $\Delta_z(t)$ is the indentation, $J(t)$ is the complex compliance of the sample in uniaxial compression, and $C_1 = [3(1-\nu^2)]/(4\sqrt{R})$ is constant with R and ν the tip radius and the poisson ratio of the sample, respectively [1]. It is clear—from Eq. (5.1)—that measurement error of indentation lead directly to the errors in the

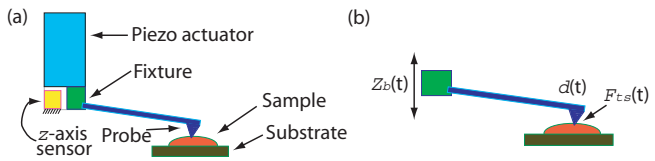

Figure 5.1: (a) The scheme of nanomechanical measurement using AFM; and (b) the model of the cantilever during the indentation measurement.

nanomechanical properties of the sample quantified.

Limit for Broadband Nanomechanical Measurement

Next we discuss the limits of the conventional indentation quantification for broadband nanomechanical spectroscopy. To quantify the indentation in the soft sample, conventionally the same input (i.e., the voltage to the z-axis piezo actuator) is applied to measure the force-distance curve on the soft sample and that on a reference hard one (e.g. a silicon sample) of stiffness several orders higher [81] (see Fig. 5.1 (a)), then by using the force-distance curves measured on both samples, the indentation at any given applied force value is calculated as the difference of the cantilever base displacement on the hard sample with respect to that on the soft one at that force value (see Fig. 5.2). To further measure the frequency-dependent nanomechanical properties of the soft sample, conventionally the above force-distance curve measurements are repeated at different load/unload rates [27], and the obtained force-indentation plots at different loading rates are used to compute, e.g., the elastic modulus, of the sample at different rates (frequencies) [18]. The cantilever base displacement is deemed to equal to the z-axis piezo actuator displacement measured. Therefore, the conventional method quantifies the indentation in broadband nanomechanical quantification by converting the measurement of dynamic properties to that of static property of the sample instead.

It is clear, from the above discussion, that the conventional indentation measurement is time consuming and too slow to capture the time evolution of the nanomechanical properties of the sample over a large frequency span rapidly. Moreover, it is assumed that the vertical z-axis motion of the AFM probe is solely caused by the AFM z-axis piezo movement, and the cantilever base displacement equals to that of the z-axis piezo actuator, measured by the z-axis sensor. These two assumptions, although reasonable in low frequency measurements,

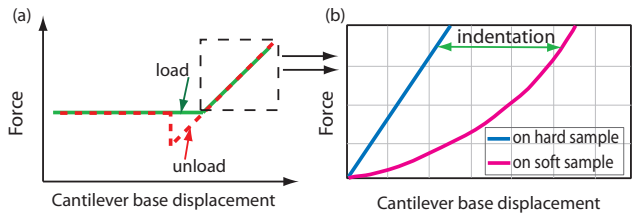

Figure 5.2: Conventional indentation measurement approach: (a) an illustrative force-distance curve; and (b) quantification of the indentation by using the force-distance curve on the soft sample and that on the hard sample.

fail when the measurement frequency range becomes large with respect to the AFM instrument dynamics.

Remark 1 *Note that the above quasi-static force-distance curve measurement has also been extended to characterize the rate-dependent viscoelastic behavior of the sample by augmenting an AC signal of much smaller amplitude to the constant-rate force curve during the process, as in the BE and the DART methods [82, 83, 84]. However, the indentation is not quantified directly, thereby, the viscoelasticity of the sample (e.g., the complex modulus) cannot be measured directly by these methods.*

Effect of Cantilever Fixture Dynamics on the Cantilever Base Displacement Measurement

Significant error can be induced by the cantilever-fixture dynamics (see Fig. 5.1(a)). When the measurement frequency is relatively low (i.e., over 1-2 orders lower than the first resonance of the cantilever-fixture), the cantilever base displacement can be accurately measured by the sensor of the z-axis piezo actuator displacement (called *the z-axis sensor* below, see Fig. 5.1(a)), i.e.,

$$z_b(j\omega) = z_{sen}(j\omega), \quad \text{when } \omega \ll \omega_{f,c}, \tag{5.2}$$

where '$j\omega$' denotes the Fourier transform of the corresponding signal, $z_b(j\omega)$ and $z_{sen}(j\omega)$ are the cantilever base displacement and the measured z-axis sensor, respectively, and $\omega_{f,c}$ is the first resonant frequency of the cantilever-fixture dynamics. As the measurement frequencies are increased and close to the resonant frequency of the cantilever-fixture dynamics, the cantilever-fixture dynamics can be excited. As a result, the cantilever base displacement cannot

be accurately measured by the z-axis sensor, i.e.,

$$z_{sen}(j\omega) \quad \neq z_b(j\omega), \quad \text{when } \omega \to \omega_{f,c} \tag{5.3}$$

Effect due to the AFM Lateral-vertical Cross-axis Coupling Dynamics

Error in the indentation measured can also be induced by the lateral-vertical cross-axis coupling of the piezo actuators and thereby, the coupling between the lateral and vertical motion of the cantilever probe. Specifically, lateral motion of the x-axis piezo actuator can be generated by the input voltage applied to the vertical z-axis piezo actuator [85]. As a normal load force is applied to the cantilever to maintain a stable probe-sample interaction during the nanomechanical measurement, the coupling-caused lateral motion of the piezo actuator results in an extraneous vibration of the probe around the contact point (i.e., a back and forth wobbling motion of the probe, see Fig. 5.3). Such a coupling-caused rotation of the probe can induce additional variation to the probe-sample contact angle and contact area. As the contact area (of the probe) on the soft sample is much larger than that on the hard one while there is virtually no indentation on the hard reference sample, the lateral-vertical coupling-caused variations in contact angle and/or contact area are much more pronounced on the soft sample, resulting in additional variations in the vertical motion (vertical deflection) of the cantilever (i.e., in the z-axis) [86]. The lateral-vertical coupling effect, although is small and negligible when the measurement is in the low frequency region (far below the first significant resonance of the AFM x-axis dynamics), becomes much larger when the measurement moves to the high frequency region and close to the resonance of the x-axis dynamics. The conventional indentation measurement, however, failed to account for the lateral-vertical cross axis coupling effect.

More concretely, in the presence of the lateral-vertical coupling effect, the total cantilever vertical displacement on the soft sample $\hat{d}_s(t)$ becomes:

$$\hat{d}_s(t) = d_{s-z}(t) + d_{s-x}(t). \tag{5.4}$$

where $d_{s-z}(t)$ and $d_{s-x}(t)$ are the cantilever vertical displacements due to the cantilever base displacement and the lateral-vertical cross coupling effect, respectively.

Thus, the above Eq. (5.4) implies that the indentation in the soft sample is generated by a combined force consisting of the z-axis excitation (corresponding to $d_{s-z}(t)$) and the

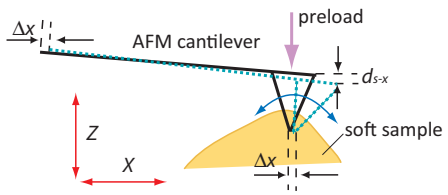

Figure 5.3: Illustration of the lateral-vertical (x-z) coupling effect on the cantilever vertical deflection during nanomechanical measurement.

lateral-vertical cross-coupling effect (corresponding to $d_{s-x}(t)$). Note that the cantilever base displacement measured by the z-axis sensor is responsible for the z-to-z cantilever vertical displacement $d_{s-z}(t)$ only, thereby, cannot be employed to quantify the total indentation.

Remark 2 *It is noted that the torsional motion of the probe is sensitive to the vertical vibration of the probe, and thereby, can be utilized to interrogate material properties through the design of the cantilever probe to amplify such a vertical-to-torsional motion coupling [87]. However, the opposite torsional-to-vertical coupling is much less pronounced, and much smaller than the longitudinal-to-vertical coupling (considered above), thereby, becomes negligible.*

5.2.2 A Control-Based Approach to Indentation Measurement of Soft Material

Next we present a control-based indentation measurement that overcomes the limits of the conventional method in broadband nanomechanical spectroscopy. We first present the proposed control-based approach to compensate for the above two adverse effects.

Compensation for the Cantilever-Fixture Dynamics Effect

The above discussion in Subsec. 5.2.1 implies that the key to accurately measuring the cantilever base displacement is to quantify the frequency response of the cantilever-fixture, $G_{fix}(j\omega)$, i.e., the frequency response from the end of the z-axis piezo actuator (measured by the z-axis sensor) to the free end of the cantilever (see Fig. 5.1(a)). The fixture dynamics $G_{fix}(j\omega)$, however, cannot be measured directly as the cantilever base displacement is not measurable when $G_{fix}(j\omega)$ is excited. Thus, we propose to quantify $G_{fix}(j\omega)$ by measuring the frequency response from the z-axis piezo displacement to the cantilever vertical displacement on a hard

reference sample (called the z-to-deflection dynamics later), $G_{z2d}(j\omega)$,

$$\begin{aligned} G_{z2d}(j\omega) &= G_{fix}(j\omega)G_c(j\omega) \\ &= \frac{z_b(j\omega)}{z_{sen}(j\omega)}\frac{d_h(j\omega)}{z_b(j\omega)} = \frac{d_h(j\omega)}{z_{sen}(j\omega)}, \end{aligned} \tag{5.5}$$

where $G_c(j\omega)$ is the cantilever dynamics under a stable contact with the hard sample (i.e., a repulsive contact under a normal force load)—from the cantilever base displacement to the cantilever vertical deflection at its free end, and $d_h(j\omega)$ and $z_{sen}(j\omega)$ denote the cantilever vertical displacement measured on a hard reference sample and the z-axis sensor signal, respectively. As the measurement frequency range is usually substantially lower (one to two orders of magnitude lower) than the resonance of the cantilever, and virtually there is no indentation in the hard sample, the cantilever dynamics $G_c(j\omega)$ is not excited in broadband nanomechanical quantification of the soft sample, and can be adequately treated as a constant for the frequency range ω_m^* in the nanomechanical measurement considered, i.e.,

$$G_c(j\omega) = \frac{d_h(j\omega)}{z_b(j\omega)} \approx g_c, \quad \text{for } \omega \leq \omega_m^* \ll \omega_c \tag{5.6}$$

where ω_m^* is the upper limit of the measured frequency range (Note ω_m^* can be larger than $\omega_{f,c}$, the first resonance of the cantilever-fixture dynamics). The constant g_c can be measured as the ratio of the cantilever vertical displacement to the z-axis sensor at low frequency (by Eq. 5.2). Then the mechanical fixture dynamics $G_{fix}(j\omega)$ is obtained by substituting Eq. (5.6) into Eq. (5.5).

Thus, during the nanomechanical measurement, the corresponding z-axis cantilever base displacement $z_b(t)$ can be obtained by using the fixture dynamics and the z-axis sensor signal measured during the process as

$$z_b(j\omega) = G_{fix}(j\omega)z_{sen}(j\omega), \tag{5.7}$$

and via inverse Fourier transform.

To measure the z-to-deflection dynamics $G_{z2d}(j\omega)$ accurately, the dynamics of z-axis piezo actuator must be compensated for, as the z-axis sensor—the output of the z-axis piezo—needs to accurately follow the desired excitation signal (e.g., a band-limited white noise or a chirp signal) during the quantification process. Direct application of the excitation signal to the z-axis piezo leads to the z-axis piezo dynamics being convoluted in the z-axis sensor signal,

causing poor signal-to-noise ratio in some frequency regions and/or saturation in others. Thus, we propose to use control techniques (e.g., MIIC technique) to ensure that the desired excitation signal can be accurately tracked by the z-axis piezo, i.e., by using the MIIC technique, the dynamics and hysteresis effects of the z-axis piezo actuator are compensated for [88]. Note that such an input (to the z-axis piezo actuator) to achieve accurate tracking of the desired excitation signal by the z-axis piezo can be obtained in advance independently, and then applied to measure $G_{z2d}(j\omega)$ under the conditions that (1) a stable probe-sample interaction is maintained, and (2) the cantilever vertical deflection on the hard reference sample is measured after the initial transient response of the probe-sample interaction becomes negligible. Also note that the above experimentally quantified cantilever-fixture dynamics $G_{fix}(j\omega)$ is independent to the cantilever and the hard reference sample used (this is verified by the experiment results presented in Sec. 5.2.4), thus only needs to be quantified once, and can be used in the nanomechanical measurement of different soft samples (or different measurement points on the same sample).

Compensation for the Lateral-Vertical Cross-Coupling Dynamics Effect

To account for the effect of the coupling-caused cantilever vertical deflection $d_{s-x}(t)$ on the cantilever base displacement, we propose to quantify the equivalent cantilever base displacement $\hat{z}_{bs}(t)$, i.e., the cantilever base displacement that corresponds to the measured cantilever vertical deflection as if there were no lateral-vertical coupling effect (see Eq. (5.4)), i.e., as if the vertical deflection of the cantilever free end is solely generated by the equivalent cantilever base displacement— the cantilever base displacement can be regarded as the driving input (see discussion in Subsec. II-C). We propose to, first, quantify the cross-coupling caused vertical deflection of the cantilever free end, $d_{s-x}(t)$, and secondly, use $d_{s-x}(t)$ to quantify the coupling-equivalent cantilever base displacement, $z_{b,cpl}(t)$, i.e., $z_{b,cpl}(t)$ would generate a cantilever vertical deflection equaling to $d_{s-x}(t)$, then finally, obtain the equivalent cantilever base displacement $\hat{z}_{bs}(t)$ as

$$\hat{z}_{bs}(t) = z_{b,cpl}(t) + z_{bs}(t) \tag{5.8}$$

where $z_{bs}(t)$ is the cantilever base displacement during the nanomechanical measurement of the soft sample (i.e., the base displacement corresponding to $d_{s-z}(t)$ in Eq. (5.4)). Note that

$z_{bs}(j\omega)$ can be quantified by using the measured z-axis sensor signal, as discussed in the above Subsec. 5.2.1 (see Eq. (5.7)).

To quantify the lateral-vertical coupling-caused cantilever vertical deflection $d_{s-x}(t)$ (see Eq. (5.4)), the frequency response of the cross-axis coupling dynamics $G_{x-z}(j\omega)$ from the cantilever lateral motion (input), $\Delta x(j\omega)$, to the resultant cantilever vertical deflection (output) on the soft sample, $\Delta d_{z-x}(j\omega)$, is measured as

$$G_{x-z}(j\omega) = \frac{\Delta d_{z-x}(j\omega)}{\Delta x(j\omega)}. \tag{5.9}$$

The key to the above frequency response quantification is to separate the cross-axis coupling-caused cantilever vertical deflection from the portion generated by the cantilever base displacement (Eq. (5.4)). Thus we propose to generate the lateral vibration of the cantilever without exciting the vertical displacement of the cantilever base, by applying an excitation input of small amplitude to the x-axis piezo actuator after a stable probe-sample interaction on the soft sample is established (under the desired preload level used in the nanomechanical measurement), then measuring the vertical vibration of the cantilever free end $\Delta d_{z-x}(t)$ (the static cantilever vertical deflection caused by the preload is subtracted) and the cantilever lateral vibration $\Delta x(t)$.

Thus, for the cantilever vertical deflection measured during the nanomechanical measurement, the portion of the cantilever vertical deflection caused by the cross-coupling effect, $d_{s-x}(t)$, can be quantified as

$$d_{s-x}(j\omega) = G_{x-z}(j\omega) d_{lat}(j\omega), \tag{5.10}$$

where $d_{lat}(j\omega)$ is the lateral vibration of the cantilever probe measured during the nanomechanical measurement. Then the portion of the cantilever vertical deflection generated by the cantilever base displacement $z_{bs}(t)$ is given by $\hat{d}_s(t) - d_{s-x}(t)$. Thus, the equivalent cantilever base displacement (corresponding to the total measured cantilever vertical vibration $\hat{d}_s(j\omega)$) is quantified as:

$$\hat{z}_{bs}(j\omega) = \frac{\hat{d}_s(j\omega)}{\hat{d}_s(j\omega) - d_{s-x}(j\omega)} z_{bs}(j\omega). \tag{5.11}$$

By also considering the effect of the cantilever-fixture dynamics, the equivalent cantilever base displacement is quantified from the measured z-sensor signal on the soft sample $z_{sen,s}(j\omega)$

as:

$$\hat{z}_{bs}(j\omega) = \frac{\hat{d}_s(j\omega)}{\hat{d}_s(j\omega) - d_{s-x}(j\omega)} G_{fix}(j\omega) z_{sen,s}(j\omega). \tag{5.12}$$

Note that the above cross-coupling compensation technique can be easily implemented in practices. First, as in the compensation for the cantilever-fixture dynamics (see Subsec. 5.2.2), control techniques such as the MIIC technique are utilized to obtain the input voltage (to the x-axis piezo actuator) in advance so that the effect of the x-axis piezo actuator dynamics can be avoided, i.e., to ensure that the displacement of the x-axis piezo actuator accurately tracks the desired frequency-rich trajectory [17, 88], e.g., a band-limited white-noise trajectory. Secondly, during the nanomechanical measurement, the frequency response of the coupling dynamics $G_{x-z}(j\omega)$ (Eq. (5.9)) is quantified right before the nanomechanical measurement (at the same location of the soft sample). The amplitude of the lateral vibration of the probe (around the instant center of the probe contact on the sample) is kept small (with respect to the preload static force) so that the translational displacement of the contact center in the x-axis direction is negligible. Finally, the cantilever lateral vibration $d_{lat}(j\omega)$ is measured along with the cantilever vertical deflection during the nanomechanical measurement (i.e., no additional force-curve measurement is needed.).

5.2.3 Tracking-based Approach to Broadband Nano-Indentation Measurement

With the above two adverse effects compensated for, we thus assume,

Assumption 4 *The cantilever base displacement can be accurately quantified through the measured z-axis sensor;*

Assumption 5 *The cross coupling effect between z-axis and x-axis on the vertical displacement of the cantilever is negligible.*

We further assume that during the broadband nanomechanical measurement,

Assumption 6 *The vibration modes of the cantilever are not excited;*

Assumption 7 *A continuous and stable probe-sample contact is maintained when the cantilever vertical deflection is measured;*

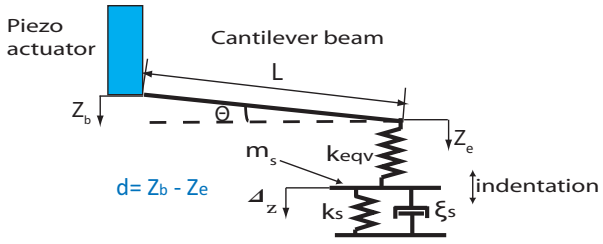

Figure 5.4: Simplified model of the tip-sample dynamics during the broadband nanomechanical measurement of soft sample.

Assumption 8 *The amplitude of the probe vibration on the sample surface is much smaller than the length of the cantilever.*

Assumption 6 holds as the measurement frequency range in nanomechanical property measurement of soft samples (usually within a few kHz) is over 10 times smaller than the first resonant frequency of the cantilever used, and consequently, the cantilever dynamics is not excited during the nanomechanical measurement. Assumption 4 also holds as the magnitude of the static preload force is at least 2-3 times larger than that of the dynamic excitation force, and consequently, the tip-sample interaction force is dominated by the repulsive electrostatic force. Thus, by Assumption 4, the repulsive tip-sample interaction can be captured by the AFM cantilever vertical deflection as F_z described as [1][48]

$$F_z(t) = k_c(z_{es}(t) - z_{bs}(t)) = -k_c d, \tag{5.13}$$

where k_c is the stiffness of the cantilever spring, and z_{es}, z_{bs} and d are the cantilever displacement at the free end and that at the base, and cantilever vertical deflection, respectively.

Finally, Assumption 5 holds as the displacement of the cantilever free-end relative to its free end is usually over 2 orders smaller than the length of the cantilever (in the range of 100-300 μm). Thus, the relative displacement of the cantilever free-end, can be measured by the vertical deflection signal at the free-end, i.e.,

$$\alpha L \sin\theta \approx \alpha L\theta \approx z_b - z_e = d, \tag{5.14}$$

where α is a constant that depends on the geometric shape of the cantilever, e.g., and equals $2/3$ for rectangular-shaped cantilever, L is the cantilever length, z_b and z_e are the displacements of the cantilever at the fixed end and the free end, respectively; θ is the bending angle of the cantilever free end relative to its fixed end, and d is the measured cantilever vertical displacement

(i.e., the normal deflection).

By Assumptions 4 and 5 (Eqs. (5.13) and (5.14)), during the nanomechanical measurement of a given soft sample in air, the dynamics of the cantilever (see Fig. 5.4) can be described in terms of the vertical deflection d_s and the indentation y_s as

$$\frac{1}{\alpha L} J \ddot{d_s}(t) = \frac{L}{2} m_c g - L k_{eqv}(z_{bs}(t) - d_s(t) - \Delta_z(t)), \tag{5.15}$$

where J and m_c are the mass moment of inertia of the cantilever relative to the fixed end, and the effective mass of the cantilever, respectively. k_{eqv} is the equivalent stiffness of the cantilever for the spring-mass-damper model as shown in Fig. 5.4. Then, the indentation and the nanomechanical properties of the sample are related through the force balance at the contact point by

$$m_s \ddot{\Delta}_z(t) = k_{eqv}(z_{bs}(t) - d_s(t) - y_s(t)) - k_s \Delta_z(t) - \xi \dot{\Delta}_z(t). \tag{5.16}$$

where m_s is the mass of the sample part involved in probe-sample interaction, and k_s and ξ_s are the equivalent spring constant and damping coefficient of the soft sample during the probe-sample interaction, respectively (see Fig. 5.4).

For the hard reference sample used in the indentation measurement, the indentation becomes negligible (compared to that on the soft sample) as the elastic modulus of the hard sample (e.g., silicon) is over several orders higher than that of the soft sample to be measured, while the viscosity of the hard sample is negligible (i.e., in Fig. 5.4, the effective spring constant $k_s \to \infty$ and the effective damping coefficient $c_s \to 0$). Thus, the dynamics of the cantilever during the nanomechanical measurement on the hard sample is reduced to (see Fig. 5.5),

$$J \ddot{\theta_h}(t) = \frac{L}{2} m_c g - L k_{eqv} z_{eh}(t), \tag{5.17}$$

where the subscript 'h' denotes the variables are with respect to the hard reference sample. The above Eq. (5.17) can be rewritten in terms of the cantilever vertical deflection d_h and the cantilever base displacement z_{bh} as

$$\frac{1}{\alpha L} J \ddot{d_h}(t) = \frac{L}{2} m_c g - L k_{eqv}(z_{bh}(t) - d_h(t)). \tag{5.18}$$

Combining Eq. (5.15) with (5.18) yields the indentation as

$$\begin{aligned} \Delta_z(t) = (z_{bs}(t) - z_{bh}(t)) + (d_h(t) - d_s(t)) \\ + \frac{1}{\alpha L^2 k_{eqv}} J(\ddot{d_s}(t) - \ddot{d_h}(t)). \end{aligned} \tag{5.19}$$

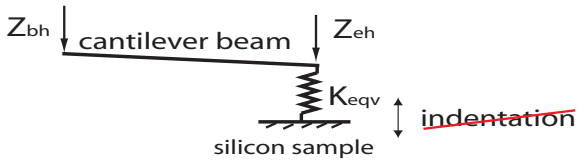

Figure 5.5: Small motion of cantilever on the hard reference sample.

The above Eq. (5.19)implies that the indentation $y_s(t)$ can be measured by using the cantilever base displacement. Particularly, control techniques are utilized to ensure precision tracking of the *same* desired cantilever vertical deflection trajectory on both the soft sample and the hard reference one, i.e., $d_s(t) = d_h(t)$ (thus the same tip-sample interaction force, i.e., Eq. (5.13)). Applying this equivalence to Eq. (5.19) yields

$$\Delta_z(t) = z_{bs}(t) - z_{bh}(t). \tag{5.20}$$

With the same desired excitation force (i.e., the same cantilever vertical deflection) accurately tracked on both the soft sample and the hard reference one, the proposed approach of indentation measurement ensures that at each time instant throughout the measurement process, the same force is applied to both samples. Therefore, with the adverse cantilever-fixture and the cross-coupling dynamics effects compensated for, the indentation can be obtained—by Eq. (5.20)—directly from the difference of the cantilever base displacement at each time instant. Note that in the proposed approach, the excitation force profile is not limited to constant load-unload rate but can have a rich frequency spectrum—needed to achieve rapid broadband nanomechanical measurement. Accurate tracking of the desired excitation force is achieved by using control techniques as discussed below immediately.

Inversion-based Iterative Control to Precision Cantilever Deflection Tracking

From the above discussion, it is evident that the key to the success of the proposed indentation measurement is to ensure (1) accurate measurement of the frequency responses of both the cantilever-fixture dynamics and the cross-coupling dynamics, and (2) the same excitation force is accurately applied to both the soft and the hard reference samples. Central to these operations is to achieve accurate tracking of a given desired trajectory of rich frequencies. In this article, we use the modeling-free inversion-based iterative learning control (MIIC) method

[32] to achieve precision tracking of the desired trajectory of complicated frequency spectrum.

Specifically, the control input signal applied to drive the AFM piezo actuator is obtained iteratively as follows (see Fig. 5.6):

$$U_{k+1}(j\omega) = \frac{U_k(j\omega)}{D_k(j\omega)} D_d(j\omega), \tag{5.21}$$

where $D_d(j\omega)$ is the desired output trajectory (e.g., the desired cantilever vertical deflection), and $U_k(j\omega)$ and $D_k(j\omega)$ are the input (e.g., the input voltage to the corresponding piezo actuator) and output signals (e.g., the cantilever vertical deflection) in the k^{th} iteration, respectively. Note that the repetitive nature of the indentation measurement makes the iterative control approach an ideal approach to track the desired cantilever vertical deflection accurately. Specifically, the MIIC technique does not require the modeling process of the system dynamics. Instead, the use of the system dynamics knowledge is embedded in the iterative process through the use of the measured input and output data. The efficacy of the MIIC technique for precision tracking of complicated trajectory (e.g., a trajectory of spectrum similar to band-limited white-noise) in nanopositioning control has been demonstrated [18, 32].

5.2.4 Experimental Implementation Example

In this part, we demonstrate the proposed approach to nanoindentation quantification in broadband nanomechanical property measurement by implementing it to measure the broadband complex modulus of a polydimethylsiloxane (PDMS) sample and three polyethylene samples with different densities.

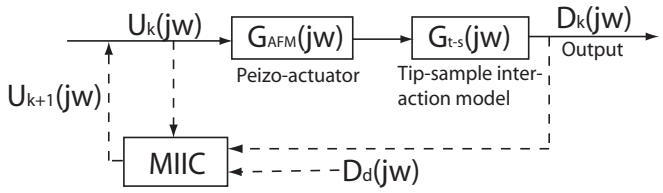

Figure 5.6: Block diagram of the MIIC technique to achieve precision tracking of the desired force profile in the proposed method to indentation measurement in air.

Table 5.1: Physical specifications of the cantilever probe

Geometry	Triangular	Tip Radius	20 nm
Spring Constant	0.3221 N/m	Tip Height	6 μm
Length	120 μm	Thickness	0.6 μm
Width	25 μm	Resonant Frequency	71.3 kHz

Experiment Setup

In the AFM system (Dimension Icon, Bruker AXS Inc.) employed in the experiments, the piezo actuators can be directly driven externally, and both the cantilever vertical (z-axis) and lateral (x-y-axes) motions of the piezo actuators can be measured directly. All the control and sensor signals were acquired through a data acquisition system under the Matlab xPC-target environment. The Matlab xPC-target package was also used to implement the MIIC technique. As the first resonant frequency of the cantilever (cantilever probe type: DNP-10, from Bruker) was over 71.3 kHz, the nominal width and the length of the cantilever were at 120 μm and 25 μm (see Table 5.1), respectively, the measurement frequency range was at 6 kHz, and the amplitude of the cantilever vibration during the following nanomechanical measurements was within 60 nm, Assumptions 3 and 5 held. Assumption 4 was also satisfied by applying a large enough static preload during the experiments. Assumptions 1 and 2 would be addressed by the proposed method as described below.

In all the experiments, the same initial conditions were maintained as closely as possible by using the same probe and applying the same preload force (56 nN) to all of the soft samples and the hard reference one (a silicon sample).

Implementation of the Proposed Nanomechanical Measurement Method to Broadband In-air Nanoindentation

In the following experiments, a band-limited white noise signal generated using Matlab was chosen as the desired excitation force to quantify the indentation for measuring the viscoelasticity in the frequency range of 100 Hz to 6 kHz (see Fig. 5.7). The average amplitude of the excitation force was 40% of the preload force, so that a stable probe-sample interaction in the repulsive region was maintained throughout the measurement (Assumption 7)), and the

plastic deformation of the PDMS sample can be ignored during the iterations when the MIIC technique was applied. We note that other excitation signal such as the model-based optimal multi-sinusoidal excitation force [89] or the dual-frequency excitation [84] have been proposed for viscoelasticity quantification. The band-limited white-noise excitation was chosen here for its uniform and rich frequency spectrum, and its capability of fully exciting the material's viscoelastic behavior without depending on the material model, thereby providing possibly the maximum information of the viscoelasticity of the sample in the measurement frequency range. Moreover, the band-limited white-noise will also fully excite the dynamics of the cantilever-fixture and the cross-axis coupling in the measurement frequency range, thereby clearly illustrating the challenges and issues in broadband nanomechanical quantification. Therefore, the band-limited white-noise signal served well as the desired excitation force in the experiment below.

First, experiments were conducted to illustrate the adverse effects of the cantilever-fixture dynamics and the lateral-vertical cross-coupling dynamics on the indentation measurement. The MIIC technique was applied to achieve precision tracking of the desired white-noise excitation force on both the PDMS sample and a silicon reference sample, as shown in Fig. 5.8 and Fig. 5.9 respectively, where the tracking error (in 2-norm) was less than 3%. In experiments, the MIIC converged rather rapidly to such an accurate tracking with merely 3-4 iterations. Then, the indentation was quantified by directly subtracting the z-axis sensor signals obtained on the silicon sample from that obtained on the PDMS sample. The z-axis sensor obtained on the

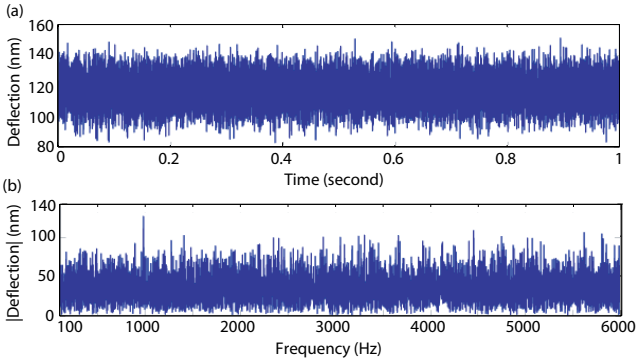

Figure 5.7: The desired excitation force (i.e., desired cantilever vertical deflection) (a) in time domain, and (b) in frequency domain (the amplitude of the Fourier transform components), used in the nanomechanical measurement experiments.

PDMS and the silicon samples and the indentation are plotted in Fig. 5.10(a), (b), and (c), respectively.

The results in Fig. 5.10 clearly showed that the adverse effects of the cantilever-fixture dynamics and the lateral-vertical coupling dynamics must be compensated for in broadband nanomechanical property quantification. Under the applied band-limited white noise excitation force, we expected that the indentation generated—as the viscoelastic response of the PDMS sample to the excitation force—shall monotonically decrease as excitation frequency increases [18], signaling the transition of the PDMS sample from the rubbery state to the glassy state [90]. On the contrary, we noticed large "peaks" appeared in the indentation shown in Fig. 5.10(c) when the cantilever-fixture dynamics and the lateral-vertical coupling effect were not compensated for. These "peaks", therefore, were measurement errors that were induced by the cantilever-fixture dynamics and the lateral-vertical coupling dynamics.

To clarify and differentiate the causes of those measurement-error induced "peaks" in the indentation plot obtained by directly using the z-axis sensor, we measured (1) the frequency response of the z-axis piezo dynamics (see Fig. 5.12(a)), (2) the cantilever lateral vibration during the nanomechanical measurement (Fig. 5.12(b)), and (3) the frequency response of the z-to-deflection dynamics $G_{z2d}(j\omega)$, as shown in Fig. 5.11. The frequency response of the z-axis piezo dynamics was measured with the AFM z-axis piezo drive voltage and the z-axis sensor as the input and output, respectively. And the z-to-deflection dynamics was measured with the z-axis sensor and cantilever vertical deflection on the silicon sample as the input and output, respectively.

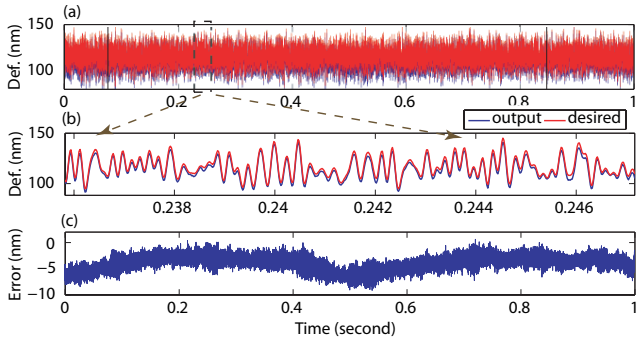

Figure 5.8: (a) The cantilever vertical deflection tracking results on the PDMS sample; (b) the zoomed-in view of the tracking results for 0.02 sec.; and (c) the tracking error.

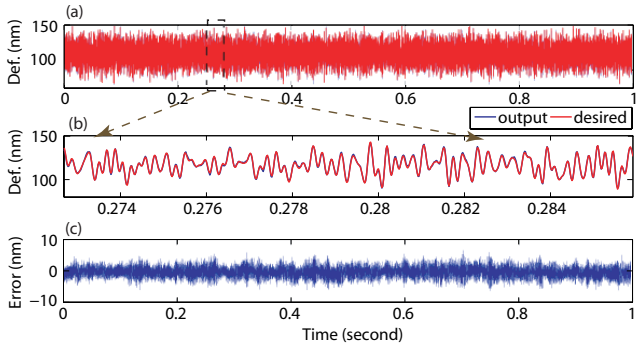

Figure 5.9: (a) The cantilever vertical deflection tracking results on the silicon sample in air; (b) the zoomed-in view of the tracking results for 0.02 sec.; and (c) the tracking error.

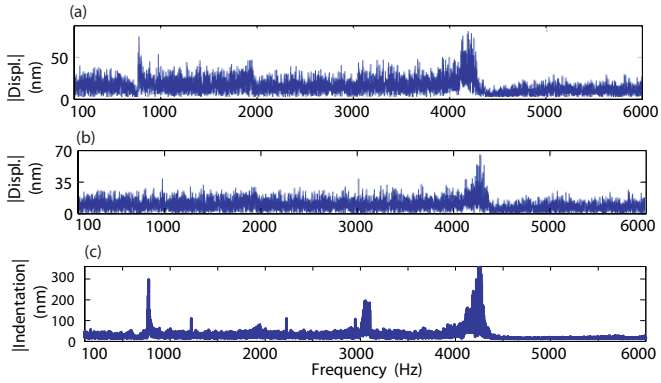

Figure 5.10: The AFM z-axis sensor measured during the nanomechanical measurement in frequency domain (the amplitude of the Fourier transform components) on (a) the PDMS sample and (b) the silicon sample, and (c) the indentation measured by directly subtracting the z-axis sensor on the PDMS sample and that on the silicon one (when the same desired cantilever vertical deflection was tracked on both samples).

The above measured frequency responses and cantilever lateral motion revealed that the "peaks" appeared in the indention obtained directly from the z-axis sensor in Fig. 5.10(c) were induced by the adverse effects of the cantilever-fixture dynamics and the lateral-vertical cross-coupling dynamics. Specifically, the "peaks" around 4300 Hz in Fig. 5.10(c) coincided with the resonant peak of the frequency response of the z-to-deflection dynamics (from the z-axis sensor to the cantilever vertical deflection) shown in Fig. 5.11. Note that the cantilever dynamics was not excited in the experiment—the cantilever vertical deflection on the hard sample was proportional to the cantilever base displacement (see Eq. (5.6)), the resonant peak around 4300 Hz was due to the cantilever-fixture dynamics. Secondly, other two groups of peaks around 715 Hz and 3000 Hz in the indentation of Fig. 5.10(c) coincided with the resonant peaks in the z-axis

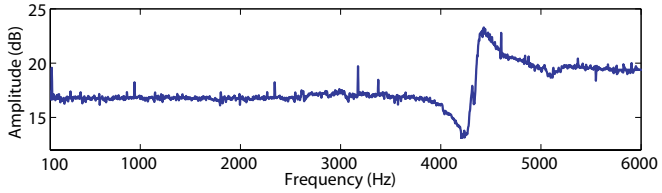

Figure 5.11: The frequency response from the z-axis sensor to the cantilever vertical deflection on the hard reference sample, $G_{z2d}(j\omega)$.

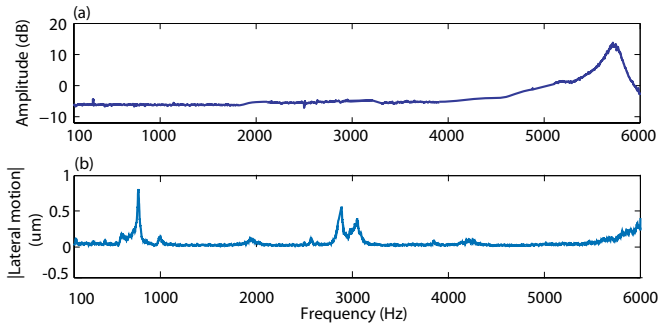

Figure 5.12: The measured frequency response of the (a) AFM z-axis piezo dynamics (with the voltage to the z-axis piezo and the z-axis sensor as the input and output, respectively), and (b) the cantilever lateral motion in frequency domain (the amplitude of the Fourier transform components).

sensor measured on the PDMS sample (Fig. 5.10(a)) (note the corresponding cantilever vertical deflection has uniform frequency spectrum—the desired white-noise excitation is tracked) and those in the cantilever lateral motion (see Fig. 5.12(b)), indicating that the lateral vibration of the cantilever caused extraneous vibration in the cantilever vertical deflection on the soft sample. Note that such a coupling effect was negligible on the hard silicon sample (see Fig. 5.10(b)). Finally, as we expected, the dynamics of the z-axis piezo actuator had no pronounced effect on the indentation measured (compare Fig. 5.10 with Fig. 5.12(a)). Thus, the experimental results demonstrated the cantilever-fixture dynamics and the cross-axis coupling dynamics effects, and the need to compensate for these adverse effects on indentation quantification in broadband nanomechanical measurement.

Broadband Nanoindentation Quantified by Using the Proposed Approach

First, the adverse effects of the cantilever-fixture dynamics and the coupling dynamics were compensated for by following the steps described in Secs. 5.2.2 and 5.2.2. We start with measuring the frequency response of the cantilever-fixture dynamics $G_{fix}(j\omega)$. To demonstrate

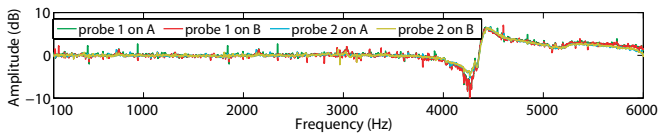

Figure 5.13: Frequency response of the mechanical dynamics between AFM sensor and cantilever base measured by using probe 1 and 2 on sample A: silicon and sample B: sapphire.

and verify that the cantilever-fixture dynamics obtained was independent with the cantilever and the hard sample used, the frequency responses using two different cantilevers (with different spring constant) and two different hard samples (silicon and sapphire) were measured. As shown in Fig. 5.13, the cantilever-fixture dynamics measured under these different conditions overlapped with each other (the largest difference between them was less than 8.3% in 2-norm). Then, the lateral-vertical cross coupling transfer function $G_{x-z}(j\omega)$ measured on the PDMS sample was obtained by driving the x-axis piezo with an amplitude small enough ($<$ 10% of the preload) so that the translational movement of the cantilever in the longitudinal direction was negligible, i.e., the x-axis drive was mainly to generate the lateral torsional motion of the cantilever probe around the sample contact point. The measured $G_{x-z}(j\omega)$ is shown in Fig. 5.14(a). Then, the cantilever vertical deflection caused by the cross-coupling effect was quantified according to Eq. (5.10), as shown in Fig. 5.14(b). With these measurements, the effect of the cantilever-fixture dynamics on the cantilever base displacement was first accounted for by using the measured $G_{fix}(j\omega)$ (Fig. 5.13) and the z-axis sensor signals measured on both the PDMS sample and the silicon reference one (see Eq. (5.7)). Then secondly, the effect of the coupling-dynamics on the z-axis sensor signal measured on the PDMS sample was further accounted for along with the lateral-vertical coupling dynamics. The compensated cantilever base displacement on the PDMS sample and that on the silicon one are shown in Fig. 5.15(a) and (b), respectively. Finally, the indentation can be quantified directly from the difference of the compensated cantilever base displacement, as shown in Fig. 5.16.

The experimental results demonstrated that the proposed approach can achieve accurate indentation quantification in broadband nanomechanical measurements. Figure. 5.15 shows that the adverse effects of the cantilever-fixture dynamics and the cross-coupling dynamics were removed. Comparison of Fig. 5.15 (a) with Fig. 5.10 (b), and Fig. 5.15 (b) with Fig. 5.10 (a) shows that the "peaks" appearing in the original z-axis sensor signals were not noticeable in the

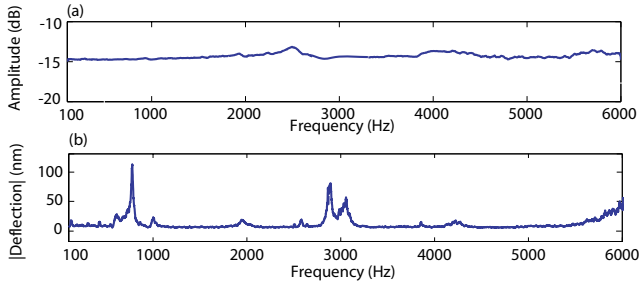

Figure 5.14: (a) The frequency response of the x-to-z cross-axis coupling dynamics measured on PDMS, and (b) the quantified cantilever vertical deflection due to the x-z cross coupling.

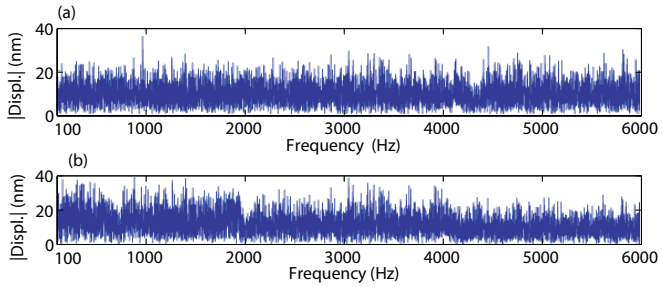

Figure 5.15: The compensated cantilever base displacement (a) on the silicon sample; (b) on the PDMS sample.

cantilever base displacements on both samples after compensation. Specifically, after compensation, the cantilever base displacement maintained a uniformly distributed amplitude across the measurement frequency range on the silicon sample, while showed an amplitude distribution monotonically decreasing with frequency increase on the PDMS sample, both agreeing with the widely-accepted elastic and viscoelastic behavior of these two materials, respectively. As a result, the cantilever-fixture dynamics and the coupling dynamics caused "peaks" were also removed in the indentation obtained by using the proposed method, as shown in Fig. 5.16. Moreover, the indentation also decreased monotonically with the increase of the excitation frequency.

Finally, to further evaluate the indentation quantified by using the proposed method, we also computed the complex modulus $E(j\omega)$ (see Fig. 5.17) of the PDMS sample by using the load-displacement relation for oscillatory loading with the radius equivalent to the mean AFM tip radius [91, 92] as

$$E(j\omega) = \frac{F_z(j\omega)}{2Ry_s(j\omega)}, \tag{5.22}$$

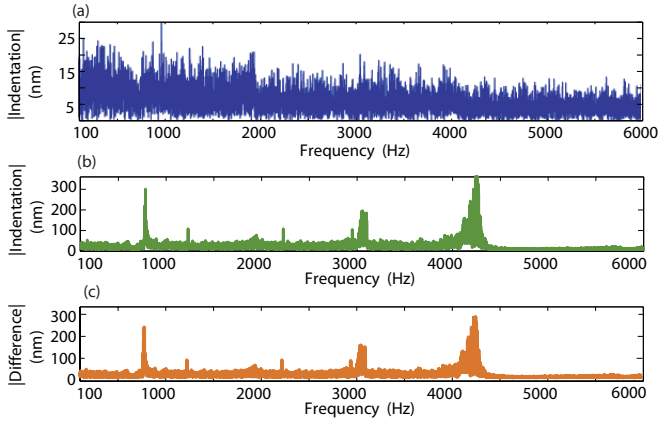

Figure 5.16: Indentation in the PDMS sample: (a) measured by using the proposed method; (b) measured by using the conventional method; (c) the indentation difference between the convectional measurement result and the proposed measurement one.

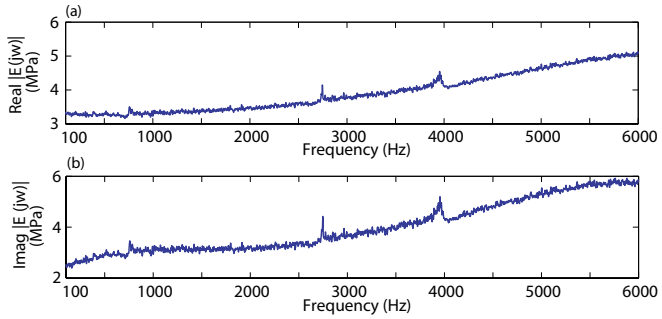

Figure 5.17: The complex modulus of the PDMS sample: (a) the real part, and (b) the imaginary part.

where R is the AFM tip radius (see Table. 5.1), and $F_z(j\omega)$ and $y_s(j\omega)$ are the tip-sample interaction force and the indentation in the PDMS sample, respectively. The obtained storage modulus (the real part of $E(j\omega)$) and loss modulus (the imaginary part of $E(j\omega)$) are plotted in Fig. 5.17. As shown in Fig. 5.17, the instrument dynamics effect on the moduli quantified was rather small—only a couple of small "spikes" appeared in the modulus plots. The value of the moduli in the low frequency range (within a few hundred Hz) compared well with that obtained in previous work [18, 19] (2-5 MPa). Note that the measurement frequency range (of the viscoelasticity quantification of PDMS using AFM) presented in this work is much larger than those reported in the literature. Therefore, the experiment results illustrate the efficacy of the proposed indentation measurement for AFM-based broadband nanomechanical measurement.

To further validate the proposed broadband nanomechancial quantification, the proposed approach was also implemented to measure the detailed viscoelastic behavior of four different

Table 5.2: Tested Polymer Samples

PDMS	LDPE 1	LDPE 1	LDPE 1
Mw 2100 g/mol	0.87 g/cm^3	0.89 g/cm^3	0.93 g/cm^3
2∼5 MPa	4∼5 MPa	∼70 MPa	∼70 MPa

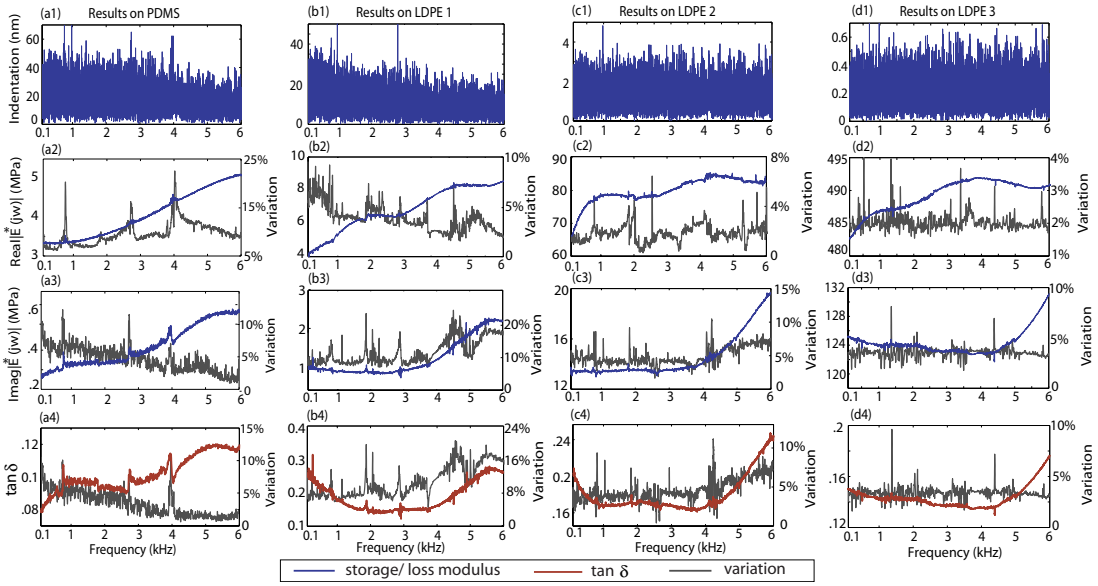

Figure 5.18: Experiment indentation, storage modulus, loss modulus and loss tangent on (a1)-(a4) PDMS, (b1)-(b4) LDPE 1, (c1)-(c4) LDPE 2, and (d1)-(d4) LDPE 3.

types of polymer samples (a PDMS sample and three LDPE samples with different densities, see Table 5.2). Specifically, the loss tangent of PDMS increases slowly from 0.07 to 0.12 in measured frequency range (see FIG.5.18(a4)). This slow change of $\tan\delta$ of PDMS shows that the low dielectric energy dissipation of this polymer is resistant to the change of load frequency, agrees well with previous studies on PDMS using nanoindenter ($\tan\delta$ increased from 0.03 at 10 Hz to 0.2 at 10 kHz) [93]. The plot of $\tan\delta$ of LDPE 1 (with the lowest density) reveals three distinct viscoelastic regimes [94] (see FIG.5.18(b4)): 1) the gradual decrease of $\tan\delta$ at low frequencies (100 Hz to $\sim$ 2 kHz) caused by stiffening of the polymer surface, due to the lesser amount of time available for molecular chain rearrangement; 2) the following flat portion of $\tan\delta$ at medium frequencies ($\sim$ 2 kHz to 3.5 kHz) associated with the stabilizing of the molecular configuration produced in the previous decrease of $\tan\delta$; and 3) the increase of $\tan\delta$ at high frequencies caused by localized softening of amorphous phase, due to the greater amount

of energy dissipation as the increase of loss modulus and free volume in the contact region. With the increase of mass density (see Table 5.2), the shape of $\tan\delta$ plot changed substantially towards lower value for LDPE 2 and 3. Such a dramatic variation is caused by overall shift of the $\tan\delta$—frequency curve due to the molecular changes, including change of crystallinity, molecular weight, and length of molecular chain. Furthermore, the results also suggested that higher density LPDE samples possessed higher resistance to loading frequency increase as the relative changes of $\tan\delta$ for LDPE 2 and 3 over the measurement frequency range were much smaller than that of LPDE 1 (45.2% and 24.6% compared to 87.5%, respectively). Note that the temperature–frequency equivalence of viscoelasticities of polymers implies that the proposed technique can also be employed as an alternative approach to interrogate the temperature dependence of nanomechanical properties of polymers [95]–the band-limited white-noise excitation shown in Fig. 5.7 draws strong similarity to the thermal vibration of materials over a broad range temperature variation [95]. Moreover, this technique is readily to be applied to other soft materials as well, such as few-layer graphene [96]. We expect that the measured frequency range (or equivalently, the accuracy of the indentation measured over a larger frequency range) can be substantially increased by using the proposed approach (care must be taken to minimize the substrate effect). Therefore, the experiment results illustrate the efficacy of the proposed indentation measurement for AFM-based broadband nanomechanical measurement.

5.3 Accurate Indentation Quantification in In-liquid Nanomechanical Measurement of Soft Material Using Atomic Force Microscope: Rate-dependent Elastic Modulus of Live Cell

Cell morphology serves for its specialized function [97]. However, in some physiological and pathophysiological events (i.e., epithelial-mesenchymal transition), cells change their morphology due to dynamic remodeling of internal cellular cytoskeleton in response to external physical force stimuli or internal reprogramming of genes expression profiles. More importantly, the morphological alterations are considered as important diagnostic indexes in the progression of numerous diseases such as fibrosis, cancer initiation and metastasis. Many studies have demonstrated that the alteration of cell shapes is associated with the change of mechanical properties

[98, 99]—Morphological alteration will affect mechanical integrity of the cell. Conversely, mechanical properties (i.e stiffness) of the cell also reflect upon the dynamics of underlying molecular activities and cell behaviors [100]. Therefore, detection and quantification of cell mechanical properties will help to predict the ongoing changes of cell morphology, function and fate.

Epithelial-mesenchymal transition (EMT) is an important biological event during embryonic development and cancer progression [101, 102]. During the EMT process, epithelial cells lose adherent and tight junctions, prompting morphological alterations towards an invasive mesenchymal phenotype. However, biomarkers that quantify and predict cells predisposition to EMT are lacking. The proposed control-based technique using AFM provides the ability to quantitatively monitor the cellular viscoelastic behavior in real time [103]. In this study, we used serum-starvation to treat HeLa cells, human cervical epithelial cancer cell line, mimicking initiation of EMT and evaluating the dynamics of cell stiffness. The morphology of HeLa cells was changed towards mesenchyme-like shape after serum deprivation for one day owing to decrease of E-Cadherin, a key component involved in the formation of adherens junction, at cell-cell junctions [104]. Indeed, our experimental results demonstrate that the rate-dependent elastic modulus of these stressed cells was also strikingly decreased compared to that of unstressed cells towards those of murine embryonic fibroblasts (MEF), mesenchymal cell line, indicative of their acquisition of mechanical characteristic as similar as MEFs. This quantification is consistent with the altered morphology. Thus, these finding suggests that the control-based indentation and nanomechanical quantification possesses great potential to quantify and even predict cell fate during the EMT process.

5.3.1 Control-based Approach to Accurate Indentation Measurement of Live Cell

We start by discussing the fundamental limits of conventional method to in-liquid indentation measurement of soft materials like live cell.

By modeling the probe-sample interaction as a spring-dashpot system under Assumptions 6 to 8 (see Fig. 5.4), the dynamics model of the rotational motion of the cantilever with respect

to its fixed end is

$$J\ddot{\theta}(t) = Lk_{eqv}(z_{es}(t) - \Delta_z(t)) - M_{hs}(t), \tag{5.23}$$

In Eq. (5.23), "$Lk_{eqv}(z_{es}(t) - \Delta_z(t))$" is the moment acting on the cantilever caused by the tip-sample interaction, and $M_{hs}(t)$ is the moment due to the hydrodynamic force exerting on the cantilever beam. As during the in-liquid force-indentation measurement the Reynolds number R_e is very small ($R_e \ll 1$) (for the cantilever velocity is at most tens of μm/s) [1, 31], the hydrodynamic force is proportional to the velocity of the cantilever, i.e.,

$$M_{hs}(t) = \int_0^L C_d w x v_s(x,t) dx, \tag{5.24}$$

where C_d and w are the drag coefficient of the liquid and the width of the cantilever, respectively. x and $v_s(x,t)$ denote a point on the cantilever with respect to the fixed-end and the velocity of the cantilever at that point, respectively. Previous work in [1, 105, 31] has shown that for AFM cantilever operations on live cell, the hydrodynamic-force-generated moment $M_{hs}(t)$ can be adequately approximated by that of an equivalent force $F_{hs}(t)$ exerting at the free end of the cantilever, i.e., $M_{hs}(t) = LF_{hs}(t)$, where the equivalent-hydrodynamic force $F_{hs}(t)$ depends on the absolute velocity of the cantilever, which in turn, can be written as the summation of the velocity of the indentation and that of the cantilever deflection,

$$M_{hs}(t) \approx LF_{hs}(t), \quad \text{with} \quad F_{hs}(t) = \mathcal{C}_d(\dot{d}_s(t) + \dot{\Delta}_z(t)), \tag{5.25}$$

where $\mathcal{C}_d$ is the equivalent drag factor of the liquid—independent to the tip-sample interaction [105, 106] (for cell culture media, $\mathcal{C}_d$ ranges between 0.2 and 0.5 μN·s/m [1]).

By the small motion assumption (Eq. (5.14)), and invoking the definition of cantilever deflection, $d(t) = z_b(t) - z_e(t)$ (see Eq. (5.23)), the above Eq. (5.23) can be rewritten in terms of deflection as

$$\frac{1}{\alpha L} J\ddot{d}_s(t) = Lk_{eqv}(z_{bs}(t) - d_s(t) - \Delta_z(t)) - M_{hs}(t). \tag{5.26}$$

Therefore, the indentation in the soft sample, $\Delta_z(t)$, can be computed as

$$\begin{aligned} \Delta_z(t) &= z_{es}(t) - \frac{J}{\alpha L^2 k_{eqv}}\ddot{d}_s(t) - \frac{1}{Lk_{eqv}} M_{hs}(t) \\ &= z_{bs}(t) - d_s(t) - \frac{J}{\alpha L^2 k_{eqv}}\ddot{d}_s(t) - \frac{1}{k_{eqv}} F_{hs}(t). \end{aligned} \tag{5.27}$$

In the conventional method (e.g., [1, 105]), the indentation is measured as the displacement difference between the base and the free-end of the cantilever on the soft sample, i.e.,

$$\hat{\Delta}_z(t) = z_{bs}(t) - d_s(t), \tag{5.28}$$

where $\hat{\Delta}_z(t)$ denotes the indentation measured by the conventional method. Thus, Eq. (5.27) implies that the conventional method (Eq. (5.28)) is valid only when the effects of both the relative probe acceleration and the hydrodynamic force are small and can be ignored, i.e., $\ddot{d}_s(t) = 0$, and $F_{hs}(t) = 0$. These two effects are negligible, however, only when the force load rate is low and maintained at constant during the force-indentation measurement. Thus, the conventional method becomes erroneous and should not be applied when measuring viscoelastic behavior of soft material (including live cell) where excitation force of multi-frequencies is applied, i.e., $\ddot{d}_s(t) \neq 0$, particularly as the excitation frequency increases. Even when the base displacement of the cantilever is maintained at a constant-rate, $\dot{z}_{bs}(t) = k_l$ with $k_l > 0$ a constant, the relative probe acceleration, due to the probe-sample interaction that leads to indentation in the soft material, is nonzero unless the load rate k_l is very small.

To be more concrete, the dynamics relating the cantilever base displacement to the cantilever deflection is analyzed. First, note that by the force balance at the contact point, the indentation dynamics is given by (see Fig. 5.4 and Eq. (5.16)

$$m_s\ddot{\Delta}_z(t) + \xi_s\dot{\Delta}_z(t) + (k_s + k_{eqv})\Delta_z(t) = k_{eqv}z_{es}(t) = k_{eqv}(z_{bs}(t) - d_s(t)), \tag{5.29}$$

To simplify the discussion but without loss of generality, the dynamics from the cantilever base displacement to the cantilever deflection can be described in frequency domain as below, by ignoring the hydrodynamic force and treating the parameters as constants (as will be discussed immediately below, the parameter variations can be accounted for by considering the variations of the frequency responses thus caused),

$$G_{z2d}(s) = \frac{D_s(s)}{Z_{bs}(s)} = \frac{m_s s^2 + \xi_s s + k_s}{\frac{J}{\alpha L^2 k_{eqv}} m_s s^4 + \frac{J}{L^2 k_{eqv}}\xi_s s^3 + (\frac{J}{\alpha L^2 k_{eqv}}k_s + m_s)s^2 + \xi_s s + (k_{eqv} + k_s)} \tag{5.30}$$

where $D_s(s)$ and $Z_{bs}(s)$ are the Laplace transforms of $d_s(t)$ and $z_{bs}(t)$, respectively. The above Eq. (5.30) is obtained by taking the Laplace transform of both Eqs. (5.27) and (5.29), and eliminating the indentation term.

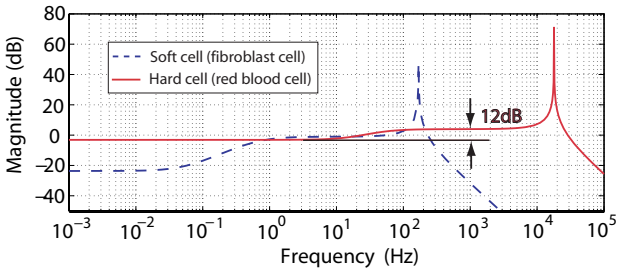

Figure 5.19: The (red) upper bound and (blue-dashed) lower bound of the frequency response of the dynamics from the cantilever base displacement to the cantilever deflection, corresponding to "hard" cell (red blood cell) and "soft" cell (fibroblast cell), respectively.

To quantify the $G_{z2d}(s)$ dynamics in Eq. (5.30), we set, $\alpha = 1$, and based on the values reported in the literature for soft and hard mammalian cells, respectively [1, 107], we choose $m_s \in$(34.7, 0.5) pg, $\xi_s \in$(0.4, 0.007) Ns·m^{-1} and $k_s \in$ (0.003, 0.24) N/m, respectively. Using these parameter ranges and accounting for mechanical properties of live cells (e.g., the largest mass and damping ratio are accompanied with the smallest spring constant [1]), the upper and lower bounds of the frequency response of $G_{z2d}(s)$ can be obtained, as shown in Fig. 5.19. It can be seen that even for hard cells (e.g., human red blood cell with Young's modulus $\sim$70 kPa [108]), $G_{z2d}(s)$ is constant only for frequencies below $\sim$10 Hz. This implies that for conventional indentation measurement to be valid, the load rate of the triangle force profile—used in usual force indentation measurement—needs to be below 2$\sim$3 Hz. This load rate limit becomes extremely small when the sample becomes softer—below 0.01 Hz for fibroblast cell with Young's modulus $\sim$1 kPa. Thus, it is evident that the relative probe acceleration effect is pronounced in nanomechanical measurement of a broad range of soft materials, including almost all live cells—The conventional indentation measurement is largely erroneous for these soft materials.

Next we discuss that for live cell measurement, the hydrodynamic force effect [109, 31, 106] on indentation quantification is much less than the relative probe acceleration effect. It can be estimated by using Eq. (5.25) that for force load velocity usually employed in nanomechanical property measurement of live cell ranging between 0.05 μm/s to 60 μm/s (for load rate between 0.1 to 100 Hz), the hydrodynamic force is within the range of 0.025$\sim$30 pN. However, the equivalent force due to the relative probe acceleration, $\frac{J}{L^2}\ddot{d}_s(t)$, is around 10 pN$\sim$1 nN, more than 30 times larger than the hydrodynamic force. Thus, it is clear that the relative probe

acceleration has a dominate impact on the indentation measurement of soft material including live cell.

In summary, the conventional indentation measurement fails to account for both the relative probe acceleration and the hydrodynamic force effects, thereby is largely erroneous for not only most elastic modulus measurement (with constant load rate), but also broadband nanomechanical measurement (with multi-frequency excitation force) of soft materials in liquid.

A Control-based Method to Accurate Indentation Measurement of Live Cell In-liquid

We propose a control-based approach that overcomes the limits of the conventional method. Specifically, the proposed approach amounts to (1) using a hard reference sample; and (2) tracking the *same* excitation force profile (i.e., the same cantilever deflection) on both the live cell and the hard reference.

Note that although by Eq. (5.27), the relative probe acceleration effect, $\frac{J}{\alpha L^2}\ddot{d}_s(t)$, might be accounted for directly by using the measured cantilever deflection signal $d_s(t)$, significant uncertainties can be induced as it is very challenging (if not completely impossible) to accurately calibrate and quantify the inertia of the cantilever, J, and the effective spring constant, k_{eqv}, as both parameters depend on the cantilever geometric configuration and the probe geometry. Moreover, the calibration process itself is time consuming and prone to external disturbances. Instead, the proposed approach removes the relative probe acceleration effect with no need to calibrate/quantify these parameters. As the indentation becomes negligible (compared to that on the live cell) on the hard reference sample (e.g., silicon, with elastic modulus several orders higher than that of live cell), the dynamics of the cantilever during in-liquid probe-sample interaction on the hard reference is reduced to (see Fig. 5.5),

$$\frac{J}{\alpha L}\ddot{d}_h(t) = Lk_{eqv}z_{eh}(t) - M_{hh}(t), \tag{5.31}$$

where the subscript 'h' denotes the variables are with respect to the hard reference sample.

Combining Eq. (5.27) with (5.31) yields the indentation as

$$\begin{aligned}\Delta_z(t) &= z_{es}(t) - z_{eh}(t) + \frac{J(\ddot{d}_h(t) - \ddot{d}_s(t))}{\alpha L^2 k_{eqv}} + \frac{M_{hh}(t) - M_{hs}(t)}{Lk_{eqv}} \\ &= z_{bs}(t) - z_{bh}(t) + d_h(t) - d_s(t) + \frac{J(\ddot{d}_h(t) - \ddot{d}_s(t))}{\alpha L^2 k_{eqv}} + \frac{(F_{hh}(t) - F_{hs}(t))}{k_{eqv}}\end{aligned} \tag{5.32}$$

The above Eq. (5.32) implies that the relative probe acceleration can be completely removed by ensuring accurate tracking of the *same* desired cantilever deflection trajectory on both the live cell and the hard reference, i.e., $d_h(t) = d_s(t)$, and thereby, the indentation is given by

$$\Delta_z(t) = z_{bs}(t) - z_{bh}(t) + \frac{(F_{hs}(t) - F_{hh}(t))}{k_{eqv}}. \tag{5.33}$$

As discussed above, the contribution of the hydrodynamic force to the indentation is rather small (at most a few nm, compared to a few hundred nm of indentation in usual live cell measurement [1, 110]). Moreover, the above Eq. (5.33) shows that the hydrodynamic force effect is further reduced as only the difference of the hydrodynamic force (soft vs. hard sample) contributes to the indentation. To quantify the reduction, we estimated the relative hydrodynamic force difference (i.e., the ratio of $F_{hs}(t) - F_{hh}(t)$ to $F_{hs}(t)$) by using Eq. (5.25) and the cantilever displacement data obtained on a fibroblast cell, as shown in Fig. 5.20 as a function of force load rate. It is clear, from Fig. 5.20, that the hydrodynamic force effect is reduced by over 45 % when force load rate is higher than 50 Hz (corresponding to force load speed of 30 μm/s with a total piezo displacement of 460 μm), and even more as the force load rate increases further, pointing to an advantage of the proposed approach for nanomechanical measurement of live cell with relatively high load rate (e.g., a few hundreds Hz).

Therefore, the proposed approach not only significantly improves the accuracy of indentation measurement on soft materials like live cell in liquid, but also is not limited to force measurement of constant drive rate only, and equally applicable to broadband nanomechanical measurement as well, i.e., the excitation force profile can be virtually chosen freely as any signal of bounded time-derivative, e.g., a band-limited white noise for rapid broadband nanomechanical characterization [111, 17].

MIIC technique [32] (see Eq. (5.21)) is implemented to to ensure precision tracking of the *same* desired cantilever deflection trajectory on both the live cell and the hard reference. Care, however, shall be taken when implementing the MIIC algorithm to live cell measurement as iteration is involved to obtain the control input (to the piezo actuator) to ensure the tracking of the same excitation force on both samples—applying the force stimuli repetitively at the same location of the live cell might deform and damage the cell membrane. Thus, instead of seeking accurate tracking of a pre-specified desired excitation force on both the live cell and

the hard reference, we use the cantilever deflection measured on the live cell (during the force measurement) as the desired force profile to be tracked on the hard reference, i.e., iteration is only needed for deflection tracking on the hard reference. Alternatively, we realize that the force applied on the live cell may not maintain the desired constant force load rate. This issue can be alleviated by applying the MIIC technique to the force-distance curve measurement on a hydrogel sample with elastic modulus similar to the live cell to be measured (i.e., the elastic modulus is within the same order), and obtaining the input signal to achieve accurate excitation force tracking on the hydrogel. Then, by applying the obtained input to the measurement on the live cell, the desired force profile can be tracked closely as well.

5.3.2 Experimental Measurement of Rate-dependent Elastic Modulus of Live Cells

In this part, we present the implementation of the above proposed control-based technique to investigate the effect of the nutrient-deprivation process on mechanical property of live mammalian cell. Specifically, the proposed technique is employed to measure the indentation (and thereby, the elastic modulus) of live HeLa cells, nutrient-deprived HeLa cells, and fibroblast cells when the force load rate is changed by three orders of magnitude. The outcome of the following experimental results shed light on the application of the proposed technique to study mechanical evolution of dynamic cellular processes such as the EMT process. We realize that HeLa cells are pathological in their properties. However, HeLa cell served well as an example in this experiment to illustrate the proposed approach. Moreover, the experiment provided pilot data to explore future implementation of the proposed approach to cancer-related studies.

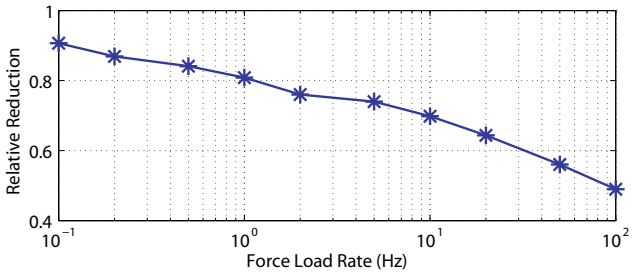

Figure 5.20: Relative reduction of the hydrodynamic force.

Cell Preparation

MEF cells and HeLa cells were maintained in DMEM (Mediatech Cat.10017CV) supplemented with 10% fetal bovine serum (FBS, Sigma, Cat. F6178) and 1% penicillin/streptomycin (Gibco, Cat.15070063). For AFM detection, 5×10^5 HeLa cells were seeded onto Collagen I-coated glasscover (BDbiosciences, Cat. 354089) in 6-well plate and grew to complete confluence overnight. Next morning, HeLa cells were washed with sterile 1xPBS for three times and then cultured in DMEM with or without 10% FBS for one more day before detection.

Experimental Setup

A triangle excitation force profile with constant load and unload rate (as employed in usual force-distance curve measurement) was applied as the desired force profile, and the load rate was varied over four orders of amplitude from 0.1 Hz to 100 Hz (see the Results part below for the ten different load rates tested), corresponding to the force velocity of 0.01 μm/s to 59 μm/s.

For ease of implementation, the amplitude of the input voltage (to the piezo actuator) was kept the same during the force-displacement measurement on the HeLa cell while the load/unload rate is changed. Then the applied force and the indentation generated were measured and used in the Hertz contact model [112, 113] to compute the elastic modulus at that load rate:

$$F_z = \frac{4}{3}\frac{E\sqrt{R\Delta_z^3}}{1-\nu^2}, \tag{5.34}$$

where R is the tip radius, and E and ν are the Young's modulus and the poisson ratio of the live cell, respectively.

A cantilever of normal spring constant of 0.01 N/m was used in the experiments. As listed in Table 5.3, the specification of the cantilever ensures that Assumptions 6 to 8 were satisfied in the experiments (where the resonant frequency is experimentally calibrated for in-liquid cantilever oscillation).

Before the indentation measurement, an AFM image of the HeLa cell topography was acquired under contact-mode (scan rate: 0.2 Hz, scan size: 20 μm $\times$ 20 μm), as shown in Fig. 5.21. Then the elastic modulus measurements were conducted near the center of the nuclei of the cell (as marked by the red cross in Fig. 5.21). Note that the center of the cell was

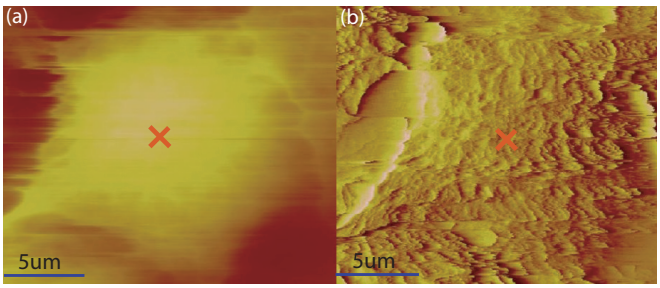

Figure 5.21: AFM topography image of the HeLa cell: (a) height; and (d) deflection error, where the cross marks the location at which the force-curve measurements were executed.

chosen–as commonly done in other nanomechanical measurements of live cell using AFM (e.g., [114, 115, 105]), to (1) eliminate the substrate effect, and (2) make the comparison between different cells easy and less prone to measurement uncertainties.

To quantify the elastic modulus of the HeLa cell and stressed HeLa cell, a triangle voltage signal was sent to drive the z-axis piezo actuator of the AFM system during the force curve measurement on the cell, and the load/unload force rate (i.e., the frequency of one entire push and retract operation) was varied between 0.1 Hz and 100 Hz for the following 10 different values (while the amplitude of the signal is maintained the same): $\{0.1,\ 0.2,\ 0.5\} \times k$ Hz ($k = 1,\ 10,\ 100$) and 100 Hz. To minimize the distortion to the cell membrane, the triangle drive was applied for only one or two periods when the force load rate was lower or higher than 50 Hz, respectively. The drive inputs were applied successively separately with a separation time of ~ 3 min between each to allow the cell to recover from the previous force stimuli. For each load rate, the excitation force exerted (i.e., the cantilever deflection) on the live cell was measured and regarded as the desired excitation force profile to be tracked on the hard reference sample (a silicon sample). Then the MIIC technique was utilized to achieve accurate tracking of the given desired force profile for each load/unload rate. The iteration was terminated when the relative-RMS-tracking error of the cantilever deflection is smaller than 3%. Finally, the

Table 5.3: Specifications of the AFM-probe used in the experiments

Geometry	Triangular	Tip Radius	20 nm
Spring Constant	0.01 N/m	Tip Height	5 μm
Length	310 μm	Thickness	0.55 μm
Width	20 μm	Resonant Frequency	2.17 kHz

indentation was quantified as the difference of the cantilever base displacement on the silicon sample from that obtained on the HeLa cell. For the force load rate employed in this study ($<$ 100 Hz), the dynamics of the z-axis piezo actuator and that of the cantilever fixture (connecting the cantilever to the z-axis piezo actuator) were not excited, and hence, the cantilever base displacement can be directly measured from the z-axis sensor (that measures the z-axis piezo actuator displacement).

To study the effect of the stress process on the elastic modulus of HeLa cell, the above protocol to indentation and nanomechanical measurement was applied to the stressed HeLa cell as well. Furthermore, to evaluate the accuracy and consistency of the method, the above indentation and nanomechanical measurement protocol was repeated on other eleven HeLa cells and sixteen stressed HeLa cells.

5.3.3 Results & Discussion

Indentation Measurement Using the Control-based Protocol

We first show the indentation of the live HeLa cell measured by using the proposed control-based protocol. Central to this protocol is to ensure accurate tracking of the *same* excitation force profile on both the cell and the silicon sample. Such an accurate tracking has been maintained (via the use of the MIIC technique [32]) across all the load/unload force rates. As an example, the tracking of the excitation force profile (measured on the HeLa cell) on the silicon

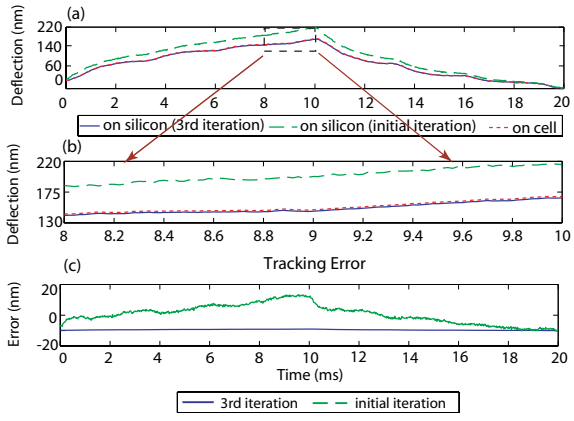

Figure 5.22: (a) The cantilever deflection tracking results (1st and 3rd iterations) on the silicon sample; (b) the zoomed-in view of the tracking results for 2 ms; and (c) the tracking error.

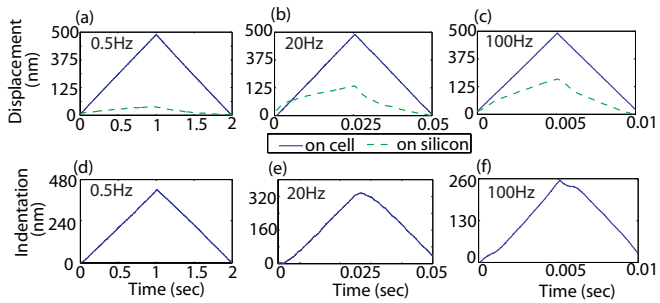

Figure 5.23: (a) The cantilever base displacement on HeLa cell and the silicon sample at 0.5Hz; (b) the cantilever base displacement on HeLa cell and the silicon sample at 20Hz; (c) the cantilever base displacement on HeLa cell and the silicon sample at 100Hz; and indentation quantified (d) at 0.5Hz,(e) at 20Hz, and (f) at 100Hz.

sample for the load rate of 50 Hz is shown in Fig. 5.22. The need of control and the efficacy of the MIIC technique to compensate for the relative probe acceleration and other adverse effects are pronounced in Fig. 5.22: Initially the cantilever deflection measured on the silicon sample was largely different from that measured on the HeLa cell—the relative RMS tracking error was at 23.4%. With the use of MIIC technique, such a large tracking error was dramatically reduced to 2.83% after merely three iterations. Same level of tracking precision ($< 3\%$) was maintained across all other 9 different load rates and during the measurements of all cells. We note that the remaining error was mainly a static offset (see Fig. 5.22(c)), which was due to the small drift of the cantilever probe in liquid. Thus, by the proposed protocol, the indentation in the HeLa cell was obtained directly from the difference of the cantilever base displacement trajectory on the HeLa cell from that on the silicon sample. As examples, the cantilever base displacement trajectory on both samples and the corresponding indentation measured were plotted in Fig. 5.23 for the load rates of 0.5 Hz, 20 Hz, and 100 Hz, respectively. Note that as we discussed before, as even the highest load rate (100 Hz) was still far below the resonance of the z-axis piezo actuator and the cantilever fixture (for the AFM system used in this work, around 5.6 kHz and 4.3 kHz, respectively), the effects of these two dynamics were negligible—As shown in Fig. 5.23 (top row), the cantilever base displacement measured on the HeLa cell followed the triangle profile of the input voltage very closely, whereas on the contrary, the cantilever base displacement measured on the silicon was largely deviated from the input triangle profile, reflecting the compensation for the relative probe acceleration and the cell viscoelasticity effect (on the cantilever deflection).

Indentation Measurement Errors of Conventional Method

Next, we present experimental results that demonstrated the limits of conventional indentation measurement. As an example, the cantilever base-deflection curve on the cell is plotted in Fig. 5.24 for load rate of 0.5 Hz, 20 Hz, and 50 Hz (top row), respectively, along with the corresponding indentation-force plot obtained by using the proposed control-based protocol compared to those by using the conventional protocol at these three rates (bottom row).

The measurement errors of the conventional method are evident, particularly when the force load rate increased and became relatively high. When using the conventional method, the cantilever base displacement needs to be greater than the cantilever deflection during the probe-sample interaction for the indentation obtained to be positive [1, 105] (see Eq. (5.28)), i.e., the base-deflection plot should stay above the dashed-line of unit slope in Fig. 5.24 (a1) to (a2). However, the base-deflection curve crossed below the unit-slope line when the load rate was increased to 20 Hz and then further to 50 Hz, respectively. As a result, the indentation measured by the conventional method became largely erroneous as the force load rate increased. As shown in Fig. 5.24 (b1) to (b3), the indentation measured by using the conventional method was closed to that measured by the proposed method at low load rate of 0.5 Hz, but then decreased with the force load rate increase and became negative during the initial portion of the measurement as the load rate increased to 20 Hz, and even more so at 50 Hz—the decrease of indentation with the force increase and negative indentation contradicted the physical reality. Therefore, the experimental results clearly demonstrated the limit of conventional method for force-indentation (nanomechanical) measurement of live cell.

The measurement error of the conventional method was further investigated along with the analysis of Sec. II-A. First, the indentation caused by the relative probe acceleration, $\frac{J}{\alpha L^2 k_{eqv}}\ddot{d}_s(t)$ (choose $\alpha = 1$), was quantified by using the measured cantilever deflection and nominal cantilever geometric values (see Table 5.3), and then added to the indentation measured by the conventional method. As shown in Fig. 5.24 (b1) to (b3), with such a modification, the difference between the indentation measured by the conventional method and that by the proposed method was largely reduced—The difference was almost completely removed at load rate of 0.5 Hz, and the modified indentation was almost completely positive even at load rate of

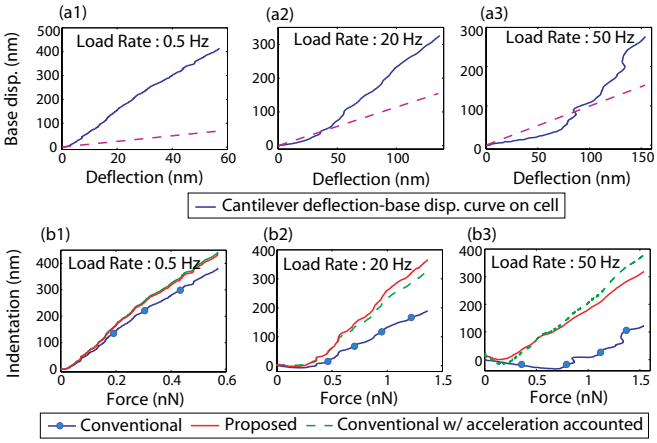

Figure 5.24: Indentation measured by using the conventional method:(a1)-(a3) cantilever deflection—base displacement curve on HeLa cell and the silicon sample at 0.5 Hz, 20 Hz, and 50 Hz by using the conventional approach, respectively; (b1)-(b3) comparison of the indentation measured by using the conventional method, the proposed approach and the corrected conventional results with taking the relative probe acceleration into account at 0.5 Hz, 20 Hz, and 50 Hz, respectively.

50 Hz. Thus, the experimental results showed that the relative probe acceleration effect played a significant role in the conventional indentation measurement. We noticed that residual difference existed between the modified indentation and that measured by the proposed method. The residual difference most likely was due to the uncertainty of the cantilever parameter values (J and L) used in computing the relative probe acceleration effect. Moreover, the relative probe acceleration effect was also compared to the hydrodynamics force effect for all the 10 measured frequencies in Fig. 5.25, where $b(0)$=0.4 μN·s/m was used in Eq. (5.25). It is clear that the indentation caused by the relative probe acceleration was much higher than that caused by the hydrodynamics force across all tested load rates (about 30$\sim$50 times higher). Hence, our experiment demonstrated the incapability of the conventional indentation measurement raised from the ignorance of both the relative probe acceleration as load rate increased and the hydrodynamic force effect.

It is evident, from the experimental results, that the conventional protocol cannot accurately measure the indentation of live cell in liquid upon high force load rate (i.e., when the relative probe acceleration becomes pronounced)—as needed to study the rate-dependent viscoelasticity of live cell.

Rate-dependent Elastic Modulus of HeLa Cell

With the proposed control-based protocol to indentation measurement established by the experiment results, we present next the rate-dependent elastic modulus measurement results. First, the indentation-force curves for the nine load rates tested in the experiment are shown in Fig. 5.26. The rate-dependence of the viscoelasticity of HeLa cell is evident—the slope of the indentation-force curve consistently decreases with the increase of the load/unload rate, reflecting that the HeLa cell "behaves" stiffer when the excitation force is exerted on the cell membrane at higher rate—agreeing with both the previous observations (e.g., [112]) and theoretical modeling study (e.g., [110]). The increasing viscoelastic behavior of the HeLa cell upon increasing force load/unload rate can also be seen from the indentation-force relation being less linear with higher load/unload rate. Moreover, we realize that as the amplitude of the input voltage (to the z-axis piezo actuator) is kept the same for each force load rate, thereby the cantilever base displacement range (at 500 nm), is kept the same in all the force-distance measurements on the HeLa cell (see Fig. 5.23, top row), the maximum indentation in the HeLa cell should decrease while the maximum reaction force from the cell membrane (equal to the applied force as the load/unload rate is very close to constant) should decrease—a direct result of the HeLa cell's appearing stiffer upon force stimuli of faster load/unload rate—exactly presented in Fig. 5.24. Note the load/unload speed corresponding to the ten load/unload rates are varying between 0.01 μm/s (for 0.1 Hz) and 59 μm/s (for 100 Hz). Thus, the experimental results show that the control-based protocol clearly captures the rate-dependence of the viscoelastic behavior of the HeLa cell.

Next, the force-indentation curve is utilized to compute the elastic modulus of the HeLa

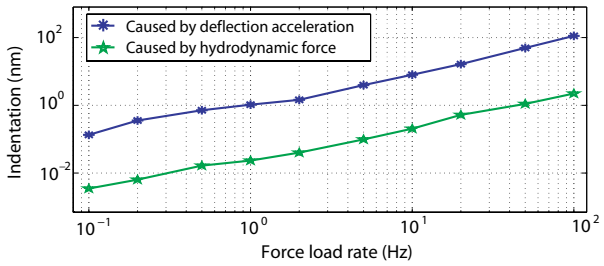

Figure 5.25: Comparison of the relative probe acceleration effect and the hydrodynamics force on the indentation

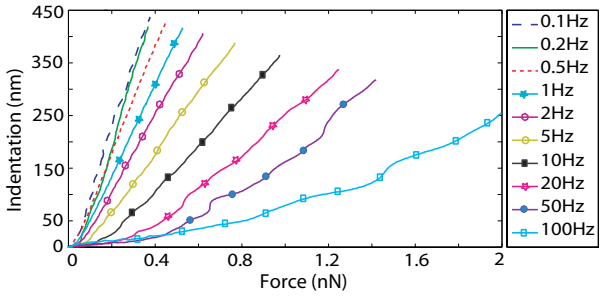

Figure 5.26: The indentation-force curves measured by using the proposed control-based protocol for nine different load rates between 0.1 Hz to 100 Hz.

cell at the ten different load rates via the Hertz model, where the maximum force-indentation point is used for each load rate. The obtained elastic modulus is plotted in Fig. 5.27 with respect to the load rate for the **twelve** different HeLa cells. Three observations are readily in-line: (1). The measured values of the elastic modulus of the HeLa cell for low force load rates of 0.1 Hz to 5 Hz at 6.71 kPa to 20.76 kPa, compared well to the that reported in [116, 117] for HeLa cell at $\sim$ 4-30 kPa for force load rate lower than 10 Hz. However, the measurements of elastic modulus of live cell using force-displacement curve as reported in the literature are all limited to low force load rate ($<$ 10 Hz)—10 times lower than the load rate reported in this work; (2). The elastic modulus–load rate plot (in logarithmic scale) in Fig. 5.27 clearly follows a power law relation—the simple linear fitting results in $E = 13.39\ \omega^{0.40\pm0.03}$ (kPa), as shown in Fig. 5.27. Such a power law modulus-rate relation agrees with those results obtained on a wide variety of live mammalian cells and via various micro-/nanorheology methods (see, e.g., review [118] and references therein) including force modulation using AFM [105, 110]. However, unlike those results using AFM [105, 110] that are all based on force modulation concept, we report in this work, for the first time, such a power-law dependence via the quasi-static force-displacement curve measurement over four orders of magnitude frequency span and up to 100 Hz; (3). Fig. 5.27 also demonstrates that the measurement results are highly consistent—the standard deviation is between 4.6% (at 50 Hz) and 11.2% (at 100 Hz). The effect of the static preload force was applied in the experiment that substantially reduced the uncertainty of the initial contact point on the cell is also determined to be small: the preload applied is kept small ($<$ 50 pN), and the comparison of the indentation measured under three different preload levels (50pN, 80pN, and 100pN) across the 10 different load rates shows that the variations of

the indentation measured across these three different preload are small across all the load rates at less than 8%.

Effect of the Serum-Starvation Process on the Elastic Modulus of HeLa Cell

Finally, the rate-dependent elastic modulus of the HeLa cell before and after the stress-process are compared. The elastic modulus for the ten different load rates measured on sixteen different HeLa cells after the stress-process (called "stressed HeLa cells" in the figures) is plotted in Fig. 5.28, and is compared with that before the stress-process in Fig. 5.29. Three observations can be drawn also: (1). Similar power-law dependence of the elastic modulus on the load rate (frequency)—as observed for HeLa cells before the stress-process (Fig. 5.27)—also holds for the HeLa cells after the stress-process ($E = 5.48\ \omega^{0.26\pm0.01}$ (kPa)). Thus, this result also supports the statement that "the power law behavior and scale-free rheology are a common feature of cell mechanics" [118]. (2). As for the HeLa cells before the stress-process, the measured modulus results are highly consistent. The standard deviation of the measured modulus among the 16 stressed HeLa cells is between 4.29% (at the load rate of 10 Hz) and 12.19% (at the load rate of 20 Hz). And (3). The dramatic effect of the stress-process on the mechanical properties of the HeLa cell is evident. As shown in Fig. 5.29, the reduction of the elastic modulus induced by the stress-process is substantially larger than the different-cell-caused variations of the modulus, and there is no overlap between the elastic modulus of the HeLa cell before the stress-process and those after the stress-process across all 10 load rates. Moreover, the stress-process-caused reduction of the elastic modulus becomes even more significant as the

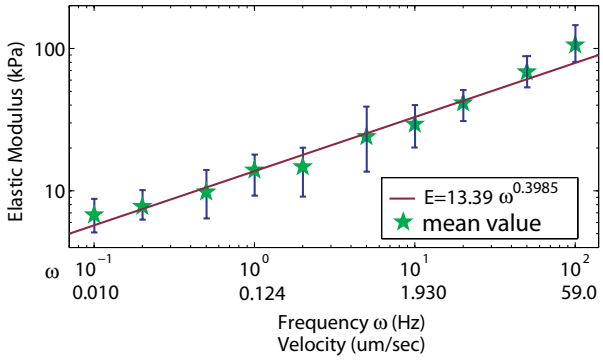

Figure 5.27: The elastic modulus vs. force load rate of the HeLa cells measured on the 12 different HeLa cells by using the proposed control-based protocol.

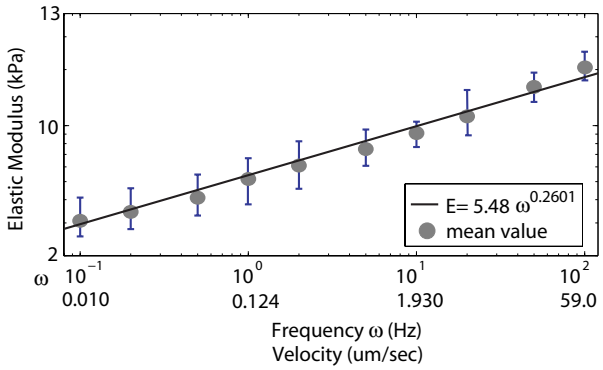

Figure 5.28: The elastic modulus vs. force load rate of the nutrient-deprived HeLa cells measured on the 16 different HeLa cells by using the proposed control-based protocol.

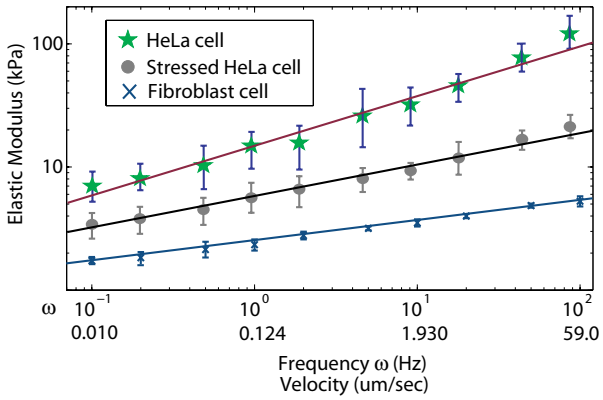

Figure 5.29: Comparison of the elastic modulus vs. the load rate for the control HeLa cells, nutrient-deprived HeLa cells that took on mesenchymal phenotype, and the fibroblast cells. The straight lines are the curve-fit of power law.

load rate increases. For example, the mean value of elastic modulus at the load rate of 100 Hz reduced by 5.07 times after the stress-process. Note that experiments have also been conducted to excluded other potential causes to such a significant change of elastic modulus, including aging of the HeLa cell. The experiments were repeated on HeLa cells that were kept in the same incubator environment along with those HeLa cells under going the stress process. The measurement elastic modulus values were similar to those measured on the un-stressed HeLa cell without one more day incubation (The difference is within the standard deviation at each measured frequency). Thus, this result is among the first that measures the stress-process effect on the elastic modulus of HeLa cell for load rate of four orders of magnitude range and up to 100 Hz.

Cellular cytoskeleton determines cell morphology and mechanical properties [119, 120].

The highly organized cytoskeleton is dynamically regulated by internal genetic and external physical or biochemical cues. Therefore, the dynamics of cytoskeleton will affect cell morphology and mechanical properties. E-Cadherin complexes form adherens junctions and transduce mechanical forces via association with actin cytoskeletal networks [121]. Once the number of adherens junctions reduced (i.e. in serum starvation), the integrity of original cytoskeleton will be compromised and consequently influence local mechanical properties. Here, our result verifies the elasticity of HeLa cells were decreased when they acquired mesenchyme-like phenotype owing to loss of cell-cell junctions. In fact, many studies have elucidated the elastic modulus of cells can be shaped due to cellular cytoskeleton reorganization during the process of cell proliferation, differentiation, and transformation [100, 98, 122, 99]. For example, invasive tumor cells become mechanically soft when they lose connection to their neighbors [123]. Highly metastatic cells have more reduced stiffness due to actin cytoskeleton remodeling compared to less invasive parental cells[124]. Thus, accurate quantification of cell mechanical properties provides a novel window to evaluate the cell predisposition and fate. Taken together, cell mechanical properties are one of important epigenetic parameters and also important indices which can be utilized to quantitatively assess cell function, plasticity and fate.

5.4 Conclusion

In this chapter, we have developed a control-based approach to broadband and in-liquid nanomechanical property quantification of soft material using AFM. The limits of the conventional indentation measurement have been discussed to clarify the adverse effects of the cantilever-fixture dynamics and the lateral-vertical cross-axis coupling dynamics for broadband quantification and the cantilever acceleration effect for in-liquid measurement, and the probe-sample interaction dynamics nanomechanical measurement has been analyzed. Then the measured frequency responses of the AFM instrument dynamics and advanced control techniques were utilized to compensate for the adverse effects for broadband quantification. Based on the analysis it has been proposed to track accurately the same broadband excitation force profile (i.e., the same cantilever vertical deflection) on both the soft sample and the hard reference one during the nanomechanical measurement, and then measure the indentation from the difference of

the cantilever base displacements obtained on both samples. The recently developed modeling-free inversion-based iterative control technique was employed to accurately track the excitation force of rich frequency spectrum. Experimental results of broadband nanoindentation measurements on polymer samples and rate-dependent elastic modulus quantification of both live HeLa cell before and after nutrient-deprivation and fibroblast cells demonstrated the efficacy of the proposed method.

Chapter 6

Conclusion

In this dissertation, a suite of control-based approaches have been developed for high-speed probe-based rapid broadband nanomechanical spectroscopy and high-speed imaging of soft and biological materials.

1. An adaptive contact-mode (ACM) imaging technique is proposed to achieve high-speed contact-mode (CM) imaging with near minimal contact force. The sample topography during CM-imaging was accurately quantified using both the z-piezo displacement and the cantilever deflection, and then the quantified sample topography was utilized in an iterative feedforward control scheme to achieve precision tracking of the sample topography during high-speed scanning, and in a gradient-based optimization scheme to adjust the deflection set-point line-by-line around the minimal level. The efficacy of the proposed ACM was demonstrated by imaging a silicon calibration sample at varies scan sizes and speed. The comparisons of the sample topography tracking performances and the normal forces between the proposed ACM imaging data and the CM-imaging results clearly showed that the imaging speed was significantly increased by 30 folds over large-size imaging, and the normal force was substantially reduced by using the proposed ACM technique.

2. Adaptive Multi-loop mode (AMLM) imaging is presented to substantially improve the speed of tapping-mode imaging. The proposed AMLM imaging combines the cantilever deflection control in CM imaging with the tapping amplitude control in TM-imaging, while maintaining the tapping motion of the probe as in the TM-imaging. First, both the z-piezo displacement and the TM-deflection are used to quantify the sample topography. Then, a feedback control loop of inner-outer loop structure is augmented to regulate the TM-deflection around the minimal-level for maintaining a stable probe tapping during

the imaging, and a data-driven online iterative learning feedforward controller is integrated to the feedback loop to further improve the tracking of the sample topography. The efficacy of the proposed AMLM imaging was demonstrated by imaging a PtBA sample at different scanning speeds (25 Hz and 40 Hz) and different imaging sizes (50 μm and 20 μm). The comparisons of the sample topography tracking performances, the averaged tip-sample interaction forces, and the tapping-amplitude fluctuation between the proposed AMLM imaging and the TM-imaging results showed that by using the proposed AMLM imaging technique, the imaging speed was significantly increased by over 10 folds over large-size imaging, and the tip-sample interaction force was substantially reduced.

3. An adaptive mode of in-liquid topography (AML) imaging has been developed to substantially improve the speed of in-liquid CM-imaging on live cells. In the proposed AML, the imaging speed is optimized online based on real-time estimation of the sample deformation, the tip-sample interaction force, as well as the sample topography variation rate, and the sample topography is quantified using both the AFM z-axis piezo placement and the cantilever deflection and then utilized in an iterative feedforward control scheme to track the sample surface. To minimize the probe-sample interaction force, the deflection set-point is adjusted line-by-line closely around the minimal level needed for maintaining a stable tip-sample interaction. The AML was experimentally validated through imaging live human prostate cancer (PC-3) cells at the average scan rates of 0.41 Hz and 0.86 Hz. Compare to the conventional CM-imaging, the AML technique was able to increase the imaging speed over four times while preserving the topography details of the live cells by accurate tracking of the sample topography.

4. We have developed a control-based approach to broadband and in-liquid nanomechanical property quantification of soft material using AFM. The limits of the conventional indentation measurement have been discussed to clarify the adverse effects of the cantilever-fixture dynamics and the lateral-vertical cross-axis coupling dynamics for broadband quantification and the cantilever acceleration effect for in-liquid measurement, and the probe-sample interaction dynamics nanomechanical measurement has been analyzed.

Then the measured frequency responses of the AFM instrument dynamics and advanced control techniques were utilized to compensate for the adverse effects for broadband quantification. Based on the analysis it has been proposed to track accurately the same broadband excitation force profile (i.e., the same cantilever vertical deflection) on both the soft sample and the hard reference one during the nanomechanical measurement, and then measure the indentation from the difference of the cantilever base displacements obtained on both samples. The recently developed modeling-free inversion-based iterative control technique was employed to accurately track the excitation force of rich frequency spectrum. Experimental results of broadband nanoindentation measurements on polymer samples and rate-dependent elastic modulus quantification of both live HeLa cell before and after nutrient-deprivation and fibroblast cells demonstrated the efficacy of the proposed method.

The most promising direction of future research on probe-based nano-quantification for soft and biological materials is to achieve high-speed simultaneous measurement of sample morphological characterization and mechanical properties quantification at nanoscale. As the correlation between morphology and nanomechanical property of biological samples plays an important role for thorough interpretation of biological phenomenon and biomedical study, future work will be focused on combining the developed high-speed imaging schemes and nanoindentation quantification approach as one single operation on AFM to achieve simultaneous quantification of these two aspects of sample properties. However, the combination is not a simple addition of the proposed approaches. Control challenges, such as non-linear tip-sample interaction dynamics and thermal drift for in-liquid measurement must be addressed.

References

[1] H.J. Butt, B. Cappella, and M. Kappl. Force measurements with the atomic force microscope: Technique, interpretation and applications. *Surface Science Reports*, 59:1–152, 2005.

[2] T Junno, S Anand, K Deppert, L Montelius, and L Samuelson. Contact mode atomic force microscopy imaging of nanometer-sized particles. *Applied physics letters*, 66(24):3295–3297, 1995.

[3] Yang Gan. Atomic and subnanometer resolution in ambient conditions by atomic force microscopy. *Surface Science Reports*, 64(3):99–121, 2009.

[4] RICARDO GARCA, ROBERT MAGERLE, and RUBEN PEREZ3. Nanoscale compositional mapping with gentle forces. *Nature Materials*, 6:405–411, June 2007.

[5] Christian Le Grimellec, Eric Lesniewska, Marie-Cécile Giocondi, Eric Finot, Véronique Vié, and Jean-Pierre Goudonnet. Imaging of the surface of living cells by low-force contact-mode atomic force microscopy. *Biophysical journal*, 75(2):695–703, 1998.

[6] D. Croft, D. McAllister and S. Devasia. High-speed scanning of piezo-probes for nanofabrication. *ASME Journal of Manufacturing Science and Engineering*, 120(3):617–622, Aug. 1998.

[7] G. M. Clayton and S. Devasia. Iterative image-based modeling and control for higher scanning probe microscope performance. *Review of Scientific Instruments*, 78(8):083704, 2007.

[8] Garrett M. Clayton, Szuchi Tien, Kam K. Leang, Qingze Zou, and Santosh Devasia. A review of feedforward control approaches in nanopositioning for high-speed spm. *ASME Journal of Dynamic Systems, Measurement and Control*, 131:061101–1 to 061101–19, 2009.

[9] S. Tien, Q. Zou, and S. Devasia. Control of dynamics-coupling effects in piezo-actuator for high-speed AFM operation. *IEEE Trans. on Control Systems Technology*, 13(6):921–931, 2005.

[10] Georg Schitter, Karl J Astrom, Barry E DeMartini, Philipp J Thurner, Kimberly L Turner, and Paul K Hansma. Design and modeling of a high-speed AFM-scanner. *Control Systems Technology, IEEE Transactions on*, 15(5):906–915, 2007.

[11] Ying Wu and Qingze Zou. An iterative based feedforward-feedback control approach to high-speed atomic force microscope imaging. *ASME Journal of Dynamic Systems, Measurement and Control*, 131:061105–1 to 061105–9, 2009.

[12] G. M. Clayton, S. Tien, K.K. Leang, Q. Zou, and S. Devasia. A review of feedforward control approaches for nano precision positioning in high speed SPM operation. *ASME Journal of Dynamic Systems, Measurement and Control*, 2008. submitted.

[13] AG. Khurshudov, K. Kato, and H. Koide. Wear of the AFM diamond tip sliding against silicon. *WEAR*, 203:22–27, 1997.

[14] G. Bar, Y. Thomann, R. Brandsch, H.J. Cantow, and M.H. Whangbo. Factors affecting the height and phase images in tapping mode atomic force microscopy. Study of phase-separated polymer blends of poly (ethene-co-styrene) and poly (2, 6-dimethyl-1, 4-phenylene oxide). *Langmuir*, 13(14):3807–3812, 1997.

[15] T. Sulchek, R. Hsieh, J. D. Adams, G. G. Yaralioglu, S. C. Minne, C. F. Quate, J. P. Cleveland, A. Atalar, and D. M. Adderton. High-speed tapping mode imaging with active q control for atomic force microscopy. *Applied Physics Letters*, 76(11):1473–1475, March 2000.

[16] T. Sulchek, G. G. Yaralioglu, and C. F. Quate. Characterization and optimization of scan speed for tapping-mode atomic force microscopy. *Review of Scientific Instruments*, 73(8):2928–2936, 2002.

[17] Zhonghua Xu, Kyongsoo Kim, Qingze Zou, and Pranav Shrotriya. Broadband measurement of rate-dependent viscoelasticity at nanoscale using scanning probe microscope: Poly (dimethylsiloxane) example. *Applied Physics Letters*, 93(13):133103, 2008.

[18] Kyong-Soo Kim, Zhiqun Lin, Pranav Shrotriya, Sriram Sundararajan, and Qingze Zou. Iterative control approach to high-speed force-distance curve measurement using AFM: time-dependent response of pdms example. *Ultramicroscopy*, 108(9):911–920, 2008.

[19] I-Kuan Lin, Kuang-Shun Ou, Yen-Ming Liao, Yan Liu, Kuo-Shen Chen, and Xin Zhang. Viscoelastic characterization and modeling of polymer transducers for biological applications. *Journal of Microelectromechanical Systems*, 18:1087 – 1099, Oct. 2009.

[20] GM Pharr, WC Oliver, and FR Brotzen. On the generality of the relationship among contact stiffness, contact area, and elastic modulus during indentation. *Journal of Materials Research*, 7(03):613–617, 1992.

[21] B.V. Derjaguin, V.M. Muller, and Yu.P Toporov. Effect of contact deformations on the adhesion of particles. *Journal of Colloid And Interface Science*, 53:314–326, 1975.

[22] D.J. Müller and Y.F. Dufrêne. Atomic force microscopy: a nanoscopic window on the cell surface. *Trends in cell biology*, 2011.

[23] J.L. Alonso and W.H. Goldmann. Feeling the forces: atomic force microscopy in cell biology. *Life sciences*, 72(23):2553–2560, 2003.

[24] Yang-Tse Cheng and Che-Min Cheng. General relationship between contact stiffness, contact depth, and mechanical properties for indentation in linear viscoelastic solids using axisymmetric indenters of arbitrary profiles. *Applied Physics Letters*, 87:111914–111916, 2005.

[25] V.M. Muller, V.S. Yushchenko, and B.V. Derjaguin. General theoretical consideration of the influence of surface forces on contact deformations and the reciprocal adhesion of elastic spherical particles. *Journal of Colloid And Interface Science*, 92:92–101, 1983.

[26] M. A. Monclus, T. J. Young, and D. Di Maio. AFM indentation method used for elastic modulus characterization of interfaces and thin layers. *Journal of Materials Science*, 45:3190–3197, 2010.

[27] Joesph E. Jakes, Rod S. Lakes, and Don S. Stone. Broadband nanoindentation of glassy polymers: Part i viscoelasticity. *Journal of Materials Research*, 27:463–474, 2012.

[28] P. M. BUECHNER, R. S. LAKES, C. SWAN, and R. A. BRAND. A broadband viscoelastic spectroscopic study of bovine bone: Implications for fluid flow. *Annals of Biomedical Engineering*, 29:719–728, 2001.

[29] A.B. Mathur, A.M. Collinsworth, W.M. Reichert, W.E. Kraus, and G.A. Truskey. Endothelial, cardiac muscle and skeletal muscle exhibit different viscous and elastic properties as determined by atomic force microscopy. *Journal of biomechanics*, 34(12):1545–1553, 2001.

[30] John Elie Sader. Frequency response of cantilever beams immersed in viscous fluids with applications to the atomic force microscope. *Journal of Applied Physics*, 84(1):64–76, 1998.

[31] RE Mahaffy, S. Park, E. Gerde, J. Käs, and CK Shih. Quantitative analysis of the viscoelastic properties of thin regions of fibroblasts using atomic force microscopy. *Biophysical journal*, 86(3):1777–1793, 2004.

[32] K. Kim and Q. Zou. A modeling-free inversion-based iterative feedforward control for precision output tracking of linear time-invariant systems. *IEEE Trans. on Mechatronics*, 18(6):1767 – 1777, 2013.

[33] A. L. Weisenhorn, M. Khorsandi, S. Kasas, V. Gotzos, and H. J. Butt. Deformation and height anomaly of soft surfaces studied with the AFM. *Nanotechnology*, 4:106–113, 1993.

[34] B Drake, CB Prater, AL Weisenhorn, SAC Gould, TR Albrecht, CF Quate, DS Cannell, HG Hansma, and PK Hansma. Imaging crystals, polymers, and processes in water with the atomic force microscope. *Science*, 243(4898):1586–1589, 1989.

[35] NA Burnham, X Chen, CS Hodges, GA Matei, EJ Thoreson, CJ Roberts, MC Davies, and SJB Tendler. Comparison of calibration methods for atomic-force microscopy cantilevers. *Nanotechnology*, 14(1):1, 2003.

[36] Donald Croft and Santosh Devasia. Hysteresis and vibration compensation for piezoactuators. *Journal of guidance, control, and dynamics*, 21(5):710–717, 1998.

[37] Ying Wu and Qingze Zou. Iterative control approach to compensate for both the hysteresis and the dynamics effects of piezo actuators. *IEEE Trans. on Control Systems Technology*, 15:936–944, 2007.

[38] LM Picco, L Bozec, A Ulcinas, DJ Engledew, M Antognozzi, MA Horton, and MJ Miles. Breaking the speed limit with atomic force microscopy. *Nanotechnology*, 18(4):044030, 2007.

[39] Toshio Ando, Takayuki Uchihashi, Noriyuki Kodera, Daisuke Yamamoto, Atsushi Miyagi, Masaaki Taniguchi, and Hayato Yamashita. High-speed afm and nano-visualization of biomolecular processes. *Pflügers Archiv-European Journal of Physiology*, 456(1):211–225, 2008.

[40] Deepak R Sahoo, Abu Sebastian, and Murti V Salapaka. Transient-signal-based sample-detection in atomic force microscopy. *Applied Physics Letters*, 83(26):5521–5523, 2003.

[41] Yan Zhang and Qingze Zou. High-speed force load in force measurement in liquid using scanning probe microscope. *Review of Scientific Instruments*, 83:013707, 2012.

[42] Andrew J Fleming. Dual-stage vertical feedback for high-speed scanning probe microscopy. *Control Systems Technology, IEEE Transactions on*, 19(1):156–165, 2011.

[43] Q Zou, KK Leang, E Sadoun, MJ Reed, and S Devasia. Control issues in high-speed afm for biological applications: Collagen imaging example. *Asian Journal of Control*, 6(2):164–178, 2004.

[44] Yan Yan, Qingze Zou, and Zhiqun Lin. A control approach to high-speed probe-based nanofabrication. *Nanotechnology*, 20(17):175301, 2009.

[45] L Ottaviano, S Di Nardo, L Lozzi, M Passacantando, P Picozzi, and S Santucci. Thin and ultra-thin films of nickel phthalocyanine grown on highly oriented pyrolitic graphite: an xps, uhv-afm and air tapping-mode afm study. *Surface science*, 373(2):318–332, 1997.

[46] DM Schaefer, R Reifenberger, A Patil, and RP Andres. Fabrication of two-dimensional arrays of nanometer-size clusters with the atomic force microscope. *Applied Physics Letters*, 66(8):1012–1014, 1995.

[47] YK Yong, SOR Moheimani, and IR Petersen. High-speed cycloid-scan atomic force microscopy. *Nanotechnology*, 21(36):365503, 2010.

[48] G. Prakash, S. Hu, A. Raman, and R. Reifenberger. Theoretical basis of parametric-resonance-based atomic force microscopy. *Physical Review B*, 79(9):094304–1–10, 2009.

[49] Troy Larsen, Katerina Moloni, Frank Flack, Mark A Eriksson, Max G Lagally, and Charles T Black. Comparison of wear characteristics of etched-silicon and carbon nanotube atomic-force microscopy probes. *Applied physics letters*, 80(11):1996–1998, 2002.

[50] Liwei Chen, Xuechun Yu, and Dan Wang. Cantilever dynamics and quality factor control in ac mode afm height measurements. *Ultramicroscopy*, 107(4):275–280, 2007.

[51] Christopher T Gibson, Brandon L Weeks, Chris Abell, Trevor Rayment, and Sverre Myhra. Calibration of afm cantilever spring constants. *Ultramicroscopy*, 97(1):113–118, 2003.

[52] James L Bosse and Bryan D Huey. Error-corrected afm: a simple and broadly applicable approach for substantially improving afm image accuracy. *Nanotechnology*, 25(15):155704, 2014.

[53] Haiming Wang, Qingze Zou, and Hongbing Xu. Inversion-based optimal output tracking–transition switching with preview for nonminimum-phase linear systems. *Automatica*, 48(7):1364–1371, 2012.

[54] Ying Wu, Qingze Zou, and Chanmin Su. A current cycle feedback iterative learning control approach for AFM imaging. *IEEE Trans. on Nanotechnology*, 8(4):515–527, 2009.

[55] Yan Yan, Haiming Wang, and Qingze Zou. A decoupled inversion-based iterative control approach to multi-axis precision positioning: 3d nanopositioning example. *Automatica*, 48(1):167–176, 2012.

[56] IA Mahmood and SO Reza Moheimani. Fast spiral-scan atomic force microscopy. *Nanotechnology*, 20(36):365503, 2009.

[57] Alvaro San Paulo and Ricardo García. Tip-surface forces, amplitude, and energy dissipation in amplitude-modulation (tapping mode) force microscopy. *Physical Review B*, 64(19):193411, 2001.

[58] C. Su, L. Huang, and K. Kjoller. Direct measurement of tapping force with a cantilever deflection force sensor. *Ultramicroscopy*, 100(3-4):233–239, 2004.

[59] B Rogers, T Sulchek, K Murray, D York, M Jones, L Manning, S Malekos, B Beneschott, JD Adams, H Cavazos, et al. High speed tapping mode atomic force microscopy in liquid using an insulated piezoelectric cantilever. *Review of scientific instruments*, 74(11):4683–4686, 2003.

[60] Bruker-Corp. Dimension fastscan, 2011.

[61] Noriyuki Kodera, Mitsuru Sakashita, and Toshio Ando. Dynamic proportional-integral-differential controller for high-speed atomic force microscopy. *Review of Scientific Instruments*, 77(8):083704, 2006.

[62] Lugen Wang. Analytical descriptions of the tapping-mode atomic force microscopy response. *Applied physics letters*, 73(25):3781–3783, 1998.

[63] JM Sloss, IS Sadek, JC Bruch Jr, and S Adali. Stabilization of structurally damped systems by time-delayed feedback control. *Dynamics and Stability of Systems*, 7(3):173–188, 1992.

[64] W Just. Principles of time delayed feedback control. *Handbook of Chaos Control*, pages 21–41, 1999.

[65] R. Garcia and A. San Paulo. Attractive and repulsive tip-sample interaction regimes in tapping-mode atomic force microscopy. *Physical Review B*, 60(7):4961–4967, 1999.

[66] Zhihua Wang, Jun Tan, Qingze Zou, and Wei Jiang. Mechanical-plowing-based high-speed patterning on hard material via advanced-control and ultrasonic probe vibration. *Review of Scientific Instruments*, 84(11):113704, 2013.

[67] Robert D Deegan, Olgica Bakajin, Todd F Dupont, Greb Huber, Sidney R Nagel, and Thomas A Witten. Capillary flow as the cause of ring stains from dried liquid drops. *Nature*, 389(6653):827–829, 1997.

[68] AA Golovin, BY Rubinstein, and LM Pismen. Effect of van der waals interactions on the fingering instability of thermally driven thin wetting films. *Langmuir*, 17(13):3930–3936, 2001.

[69] Zhihua Wang and Qingze Zou. Iterative-control-based high-speed direct mask fabrication via ultrasonic-vibration-assisted mechanical plowing. In *Proceedings of ASME Dynamic Systems and Control Conference*, pages 1784–1791, DOI:10.1115/DSCC2013–3945, Palo Alto, CA, 2013.

[70] Monika Fritz, Manfred Radmacher, and Hermann E Gaub. Granula motion and membrane spreading during activation of human platelets imaged by atomic force microscopy. *Biophysical journal*, 66(5):1328–1334, 1994.

[71] Hong Xing You, Joan M Lau, Shengwen Zhang, and Lei Yu. Atomic force microscopy imaging of living cells: a preliminary study of the disruptive effect of the cantilever tip on cell morphology. *Ultramicroscopy*, 82(1):297–305, 2000.

[72] PG Haydon, R Lartius, V Parpura, and SP MARCHESE-RAGONA. Membrane deformation of living glial cells using atomic force microscopy. *Journal of microscopy*, 182(2):114–120, 1996.

[73] Anshu Bagga Mathur, George A Truskey, and W Monty Reichert. Atomic force and total internal reflection fluorescence microscopy for the study of force transmission in endothelial cells. *Biophysical Journal*, 78(4):1725–1735, 2000.

[74] M. Shibata, H. Yamashita, T. Uchihashi, H. Kandori, and T. Ando. High-speed atomic force microscopy shows dynamic molecular processes in photoactivated bacteriorhodopsin. *Nature nanotechnology*, 5(3):208–212, 2010.

[75] N. Kodera, D. Yamamoto, R. Ishikawa, and T. Ando. Video imaging of walking myosin v by high-speed atomic force microscopy. *Nature*, 468(7320):72–76, 2010.

[76] Yuki Suzuki, Nobuaki Sakai, Aiko Yoshida, Yoshitsugu Uekusa, Akira Yagi, Yuka Imaoka, Shuichi Ito, Koichi Karaki, and Kunio Takeyasu. High-speed atomic force microscopy combined with inverted optical microscopy for studying cellular events. *Scientific reports*, 3, 2013.

[77] Juan Ren and Qingze Zou. High-speed adaptive contact-mode atomic force microscopy imaging with near-minimum-force. *Review of Scientific Instruments*, 85(7):073706, 2014.

[78] H Oberleithner, SW Schneider, L Albermann, U Hillebrand, T Ludwig, C Riethmüller, V Shahin, C Schäfer, and H Schillers. Endothelial cell swelling by aldosterone. *The Journal of membrane biology*, 196(3):163–172, 2003.

[79] Stefan W Schneider, Philipp Pagel, Christian Rotsch, Timm Danker, Hans Oberleithner, Manfred Radmacher, and Albrecht Schwab. Volume dynamics in migrating epithelial cells measured with atomic force microscopy. *Pflügers Archiv*, 439(3):297–303, 2000.

[80] Kenneth Langstreth Johnson and Kenneth Langstreth Johnson. *Contact mechanics*. Cambridge university press, 1987.

[81] Bhushan Bharat and Koinkar Vilas N. Nanoindentation hardness measurements using atomic force microscopy. *Applied Physics Letters*, 64:1653–1655, 1994.

[82] Stephen Jesse and Sergei V Kalinin. Band excitation in scanning probe microscopy: sines of change. *JOURNAL OF PHYSICS D: APPLIED PHYSICS*, 44:464006, 2011.

[83] Stephen Jesse, Sergei V Kalinin, Roger Proksch, A P Baddorf, and B J Rodriguez. The band excitation method in scanning probe microscopy for rapid mapping of energy dissipation on the nanoscale. *NANOTECHNOLOGY*, 18(43):435503, 2007.

[84] A Gannepalli, D G Yablon, A H Tsou, and R Proksch. Mapping nanoscale elasticity and dissipation using dual frequency contact resonance AFM. *NANOTECHNOLOGY*, 22(35):355705, 2011.

[85] Ying Wu, Jian Shi, Chanmin Su, and Qingze Zou. A control approach to cross-coupling compensation of piezotube scanners in tapping-mode atomic force microscope imaging. *Review of Scientific Instruments*, 80(4):043709, 2009.

[86] L Huang, C Meyer, and C Prater. Eliminating lateral forces during AFM indentation. *Journal of Physics Conference Series*, 61:805–809, 2007.

[87] O. Sahin, S. Magonov, C. Su, C.F. Quate, and O. Solgaard. An atomic force microscope tip designed to measure time-varying nanomechanical forces. *Nature Nanotechnology*, 2(8):507–514, 2007.

[88] Kyong Soo Kim and Qingze Zou;. Model-less inversion-based iterative control for output tracking: Piezo actuator example. In *Proceedings of American Control Conference*, pages 2710 – 2715, Seattle, WA, June 2008.

[89] Zhonghua Xu and Qingze Zou. Optimal input design in indentation-based rapid broadband nanomechanical spectroscopy: Poly(dimethylsiloxane) example. *IEEE Trans. on Control Systems Technology*, 2011. under review.

[90] Zhonghua Xu, Derek Tramp, Qingze Zou, Pranav Shrotriya, and Ping Xie. Nanoscale broadband viscoelastic spectroscopy of soft materials using iterative control. *Experimental Mechanics*, in press, 2011.

[91] J.A. Greenwood and K.L. Johnson. Oscillatory loading of a viscoelastic adhesive contact. *Journal of Colloid and Interface Science*, 296(1):28402291, April 2006.

[92] Wahl KJ, Asif SA, Greenwood JA, and Johnson KL. Oscillating adhesive contacts between micron-scale tips and compliant polymers. *Journal of Colloid and Interface Science*, 296(1):178–188, April 2006.

[93] Roderic S. Lakes. *Viscoelastic solids*. CRC Press, 1999.

[94] A Chakravartula and K Komvopoulos. Viscoelastic properties of polymer surfaces investigated by nanoscale dynamic mechanical analysis. *Applied physics letters*, 88(13):131901–131901, 2006.

[95] MMJ Treacy, TW Ebbesen, and JM Gibson. Exceptionally high young's modulus observed for individual carbon nanotubes. *Nature*, 1996.

[96] Changgu Lee, Xiaoding Wei, Jeffrey W Kysar, and James Hone. Measurement of the elastic properties and intrinsic strength of monolayer graphene. *science*, 321(5887):385–388, 2008.

[97] D'Arcy Wentworth Thompson and J.T. Bonner. *On growth and form*. Cambridge University Press, 1992.

[98] A. Clark and E. Paluch. Mechanics and regulation of cell shape during the cell cycle. *Cell Cycle in Development*, pages 31–73, 2011.

[99] P.S. Mathieu and E.G. Loboa. Cytoskeletal and focal adhesion influences on mesenchymal stem cell shape, mechanical properties, and differentiation down osteogenic, adipogenic, and chondrogenic pathways. *Tissue Engineering Part B: Reviews*, pages 18(6): 436–44, 2012.

[100] D.A. Fletcher and R.D. Mullins. Cell mechanics and the cytoskeleton. *Nature*, 463(7280):485–492, 2010.

[101] H. Acloque, J.P. Thiery, and M.A. Nieto. The physiology and pathology of the emt. *EMBO reports*, 9(4):322–326, 2008.

[102] B. De Craene and G. Berx. Regulatory networks defining emt during cancer initiation and progression. *Nature Reviews Cancer*, 13(2):97–110, 2013.

[103] R. Lal and SA John. Biological applications of atomic force microscopy. *American Journal of Physiology-Cell Physiology*, 266(1):C1–C21, 1994.

[104] I. Royal, N. Lamarche-Vane, L. Lamorte, K. Kaibuchi, and M. Park. Activation of cdc42, rac, pak, and rho-kinase in response to hepatocyte growth factor differentially regulates epithelial cell colony spreading and dissociation. *Molecular biology of the cell*, 11(5):1709–1725, 2000.

[105] J. Alcaraz, L. Buscemi, M. Grabulosa, X. Trepat, B. Fabry, R. Farré, and D. Navajas. Microrheology of human lung epithelial cells measured by atomic force microscopy. *Biophysical journal*, 84(3):2071–2079, 2003.

[106] R. E. Mahaffy, C. K. Shih, F. C. MacKintosh, and J. Käs. Scanning probe-based frequency-dependent microrheology of polymer gels and biological cells. *Phys. Rev. Lett.*, 85(4):880–883, Jul 2000.

[107] T.G. Kuznetsova, M.N. Starodubtseva, N.I. Yegorenkov, S.A. Chizhik, R.I. Zhdanov, et al. Atomic force microscopy probing of cell elasticity. *Micron*, 38(8):824–833, 2007.

[108] Studying the mechanical properties of red blood cells with nanovision, 2009. Application Note, Agilent Technologies, http://cp.literature.agilent.com/litweb/pdf/5990-5020EN.pdf.

[109] James W. M. Chon, Paul Mulvaney, and John E. Sader. Experimental validation of theoretical models for the frequency response of atomic force microscope cantilever beams immersed in fluids. *Journal of Applied Physics*, 87(8):3978–3988, 2000.

[110] BA Smith, B Tolloczko, JG Martin, and P Grütter. Probing the viscoelastic behavior of cultured airway smooth muscle cells with atomic force microscopy: stiffening induced by contractile agonist. *Biophysical journal*, 88(4):2994–3007, 2005.

[111] Juan Ren, Aliyeh Mousavi, Xuemei Li, Qingze Zou, Natalia Erina, and Chanmin Su. Enhanced measurement of broadband nanomechanical property of polymers using atomic force microscope. *Applied Physics Letters*, 102(18):183116, 2013.

[112] Q.S. Li, G.Y.H. Lee, C.N. Ong, and C.T. Lim. AFM indentation study of breast cancer cells. *Biochemical and Biophysical Research Communications*, 374:609–613, 2008.

[113] Dimitrios Kirmizis and Stergios Logothetidis. Atomic force microscopy probing in the measurement of cell mechanics. *International Journal of Nanomedicine*, 5:13717145, 2010.

[114] Shamik Sen, Shyamsundar Subramanian, and Dennis E. Discher. Indentation and adhesive probing of a cell membrane with AFM: Theoretical model and experiments. *Biophysical Journal*, 89(5):3203173213, 2005.

[115] M.J. Rosenbluth, W.A. Lam, and D.A. Fletcher. Force microscopy of nonadherent cells: a comparison of leukemia cell deformability. *Biophysical journal*, 90(8):2994–3003, 2006.

[116] Yeh-Chuin Poh, Sergey P. Shevtsov, Farhan Chowdhury, Douglas C. Wu, Sungsoo Na, Miroslav Dundr, and Ning Wang. Dynamic force-induced direct dissociation of protein complexes in a nuclear body in living cells. *Nature Communication*, 866(1873), 2012.

[117] A. Berquand, A. Holloschi, M. Trendelenburg, and P. Kioschis. Analysis of cytoskeleton-destabilizing agents by optimized optical navigation and AFM force measurements. *Microscopy Today*, 1017(S1551929510000131), 2010.

[118] G. Lenormand and J.J. Fredberg. Deformability, dynamics, and remodeling of cytoskeleton of the adherent living cell. *Biorheology*, 43(1):1–30, 2006.

[119] S. Kim and P.A. Coulombe. Emerging role for the cytoskeleton as an organizer and regulator of translation. *Nature Reviews Molecular Cell Biology*, 11(1):75–81, 2010.

[120] B. Fabry, A.H. Klemm, S. Kienle, T.E. Schäffer, and W.H. Goldmann. Focal adhesion kinase stabilizes the cytoskeleton. *Biophysical journal*, 101(9):2131–2138, 2011.

[121] N. Borghi, M. Sorokina, O.G. Shcherbakova, W.I. Weis, B.L. Pruitt, W.J. Nelson, and A.R. Dunn. E-cadherin is under constitutive actomyosin-generated tension that is increased at cell–cell contacts upon externally applied stretch. *Proceedings of the National Academy of Sciences*, 109(31):12568–12573, 2012.

[122] V. Swaminathan, K. Mythreye, E.T. O'Brien, A. Berchuck, G.C. Blobe, and R. Superfine. Mechanical stiffness grades metastatic potential in patient tumor cells and in cancer cell lines. *Cancer research*, 71(15):5075–5080, 2011.

[123] J. Guck, S. Schinkinger, B. Lincoln, F. Wottawah, S. Ebert, M. Romeyke, D. Lenz, H.M. Erickson, R. Ananthakrishnan, D. Mitchell, et al. Optical deformability as an inherent cell marker for testing malignant transformation and metastatic competence. *Biophysical journal*, 88(5):3689–3698, 2005.

[124] W. Xu, R. Mezencev, B. Kim, L. Wang, J. McDonald, and T. Sulchek. Cell stiffness is a biomarker of the metastatic potential of ovarian cancer cells. *PloS one*, 7(10):e46609, 2012.

[125] M. Lekka, P. Laidler, D. Gil, J. Lekki, Z. Stachura, and A.Z. Hrynkiewicz. Elasticity of normal and cancerous human bladder cells studied by scanning force microscopy. *European Biophysics Journal*, 28:312–316, 1999.

[126] M. Lekka and P. Laidler. Applicability of AFM in cancer detection. *Nature Nanotechnology*, 4(2):72–72, 2009.

[127] Thomas P Stossel. On the crawling of animal cells. *Science*, 260(5111):1086–1094, 1993.

[128] Juliet Lee, Akira Ishihara, and Ken Jacobson. How do cells move along surfaces? *Trends in cell biology*, 3(11):366–370, 1993.

[129] Hermann Schillers, Mike Wälte, Katarina Urbanova, and Hans Oberleithner. Real-time monitoring of cell elasticity reveals oscillating myosin activity. *Biophysical journal*, 99(11):3639–3646, 2010.

[130] LM Rebêlo, JS De Sousa, J Mendes Filho, and M Radmacher. Comparison of the viscoelastic properties of cells from different kidney cancer phenotypes measured with atomic force microscopy. *Nanotechnology*, 24(5):055102, 2013.

[131] Christian Rotsch and Manfred Radmacher. Drug-induced changes of cytoskeletal structure and mechanics in fibroblasts: an atomic force microscopy study. *Biophysical Journal*, 78(1):520–535, 2000.

[132] Gabriel YH Lee and Chwee T Lim. Biomechanics approaches to studying human diseases. *Trends in biotechnology*, 25(3):111–118, 2007.

[133] Juan Ren, Shiyan Yu, Nan Gao, and Qingze Zou. Indentation quantification for in-liquid nanomechanical measurement of soft material using an atomic force microscope: Rate-dependent elastic modulus of live cells. *Physical Review E*, 88(5):052711, 2013.

[134] LM Rebêlo, JS de Sousa, J Mendes Filho, J Schäpe, H Doschke, and M Radmacher. Microrheology of cells with magnetic force modulation atomic force microscopy. *Soft matter*, 10(13):2141–2149, 2014.

[135] M. Radmacher, RW Tillmann, and HE Gaub. Imaging viscoelasticity by force modulation with the atomic force microscope. *Biophysical journal*, 64(3):735–742, 1993.

[136] Juan Ren and Qingze Zou. A control-based approach to accurate nanoindentation quantification in broadband nanomechanical measurement using scanning probe microscope. *Nanotechnology, IEEE Transactions on*, 13(1):46 – 54, 2014.

[137] H. Karcher, J. Lammerding, H. Huang, R.T. Lee, R.D. Kamm, and M.R. Kaazempur-Mofrad. A three-dimensional viscoelastic model for cell deformation with experimental verification. *Biophysical journal*, 85(5):3336–3349, 2003.

[138] Hayden Huang, Roger D. Kamm, and Richard T. Lee. Cell mechanics and mechanotransduction: pathways, probes, and physiology. *Am J Physiol Cell Physiol*, 287(1):C1–11, 2004.

[139] Di Chen, Qiuzhi Cindy Cui, Huanjie Yang, and Q Ping Dou. Disulfiram, a clinically used anti-alcoholism drug and copper-binding agent, induces apoptotic cell death in breast cancer cultures and xenografts via inhibition of the proteasome activity. *Cancer research*, 66(21):10425–10433, 2006.

[140] Juan Ren, Aliyeh Mousavi, Xuemei Li, Qingze Zou, Natalia Erina, and Chanmin Su. Enhanced measurement of broadband nanomechanical property of polymers using atomic force microscope. *Applied Physics Letters*, 102(18):183116, 2013.

[141] Zhonghua Xu, Kyongsoo Kim, Qingze Zou, and Pranav Shrotriya. Broadband measurement of rate-dependent viscoelasticity at nanoscale using scanning probe microscope: Poly(dimethylsiloxane) example. *Applied Physics Letters*, 93:133103, 2008.

[142] Zhonghua Xu and Qingze Zou. A model-based approach to compensate for the dynamics convolution effect on nanomechanical property measurement. *Journal of Applied Physics*, 107:064315, 2010.

[143] Artur Zdunek and Andrzej Kurenda. Determination of the elastic properties of tomato fruit cells with an atomic force microscope. *Sensors*, 13(9):12175–12191, 2013.

[144] Brenton D Hoffman and John C Crocker. Cell mechanics: dissecting the physical responses of cells to force. *Annual review of biomedical engineering*, 11:259–288, 2009.

[145] Mohammad RK Mofrad and Roger Kamm. *Cytoskeletal mechanics*. Cambridge University Press New York:, 2006.

[146] Bruce Alberts, Dennis Bray, Julian Lewis, Martin Raff, Keith Roberts, and James D. Watson. *Molecular biology of the cell.* New York: Garland, 4th ed. edition, 2002.

[147] Antti Vaheri, Olli Carpén, Leena Heiska, Tuula S Helander, Juha Jääskeläinen, Päivi Majander-Nordenswan, Markku Sainio, Tuomo Timonen, and Ossi Turunen. The ezrin protein family: membrane-cytoskeleton interactions and disease associations. *Current opinion in cell biology*, 9(5):659–666, 1997.

[148] Lea Glass-Marmor and Rivka Beitner. Taxol (paclitaxel) induces a detachment of phosphofructokinase from cytoskeleton of melanoma cells and decreases the levels of glucose 1, 6-bisphosphate, fructose 1, 6-bisphosphate and atp. *European journal of pharmacology*, 370(2):195–199, 1999.

[149] Y Potchoo, D Braguer, V Peyrot, AM Chauvet-Monges, JC Sari, and A Crevat. In vitro inhibition of microtubule assembly by disulfiram. *International journal of clinical pharmacology, therapy, and toxicology*, 24(9):499–504, 1986.

[150] Dazhi Cen, Daniel Brayton, Babbak Shahandeh, Frank L Meyskens, and Patrick J Farmer. Disulfiram facilitates intracellular cu uptake and induces apoptosis in human melanoma cells. *Journal of medicinal chemistry*, 47(27):6914–6920, 2004.

[151] Hiroshi Hirai, Hiroshi Sootome, Yoko Nakatsuru, Katsuyoshi Miyama, Shunsuke Taguchi, Kyoko Tsujioka, Yoko Ueno, Harold Hatch, Pradip K Majumder, Bo-Sheng Pan, et al. Mk-2206, an allosteric akt inhibitor, enhances antitumor efficacy by standard chemotherapeutic agents or molecular targeted drugs in vitro and in vivo. *Molecular cancer therapeutics*, 9(7):1956–1967, 2010.

[152] SU-HYEONG Kim, Yong-SUNG Juhnn, and YONG-SANG Song. Akt involvement in paclitaxel chemoresistance of human ovarian cancer cells. *Annals of the New York Academy of Sciences*, 1095(1):82–89, 2007.

[153] Haijun Zhang, Di Chen, Jonathan Ringler, Wei Chen, Qiuzhi Cindy Cui, Stephen P Ethier, Q Ping Dou, and Guojun Wu. Disulfiram treatment facilitates phosphoinositide 3-kinase inhibition in human breast cancer cells in vitro and in vivo. *Cancer research*, 70(10):3996–4004, 2010.

[154] Xi Zheng, Richard L Chang, Xiao-Xing Cui, Gina E Avila, Vidya Hebbar, Mark Garzotto, Weichung Joe Shih, Yong Lin, Shou-En Lu, Arnold B Rabson, et al. Effects of 12-o-tetradecanoylphorbol-13-acetate (tpa) in combination with paclitaxel (taxol) on prostate cancer lncap cells cultured in vitro or grown as xenograft tumors in immunodeficient mice. *Clinical cancer research*, 12(11):3444–3451, 2006.

[155] Jacqueline K Akunda, Huei-Chen Lao, Chris A Lee, Alisha R Sessoms, Rachel M Slade, and Robert Langenbach. Genetic deficiency or pharmacological inhibition of cyclooxygenase-1 or-2 induces mouse keratinocyte differentiation in vitro and in vivo. *The FASEB journal*, 18(1):185–187, 2004.

[156] Uwe Werling, Sandra Siehler, Margarethe Litfin, Heinz Nau, and Martin Göttlicher. Induction of differentiation in f9 cells and activation of peroxisome proliferator-activated receptor δ by valproic acid and its teratogenic derivatives. *Molecular Pharmacology*, 59(5):1269–1276, 2001.

[157] Sui-Ting Lee, Pooi-Fong Wong, Shiau-Chuen Cheah, and Mohd Rais Mustafa. Alpha-tomatine induces apoptosis and inhibits nuclear factor-kappa b activation on human prostatic adenocarcinoma pc-3 cells. *PLoS One*, 6(4):e18915, 2011.

[158] S Ma, L Rao, IM Freedberg, and M Blumenberg. Transcriptional control of k5, k6, k14, and k17 keratin genes by ap-1 and nf-kappab family members. *Gene expression*, 6(6):361–370, 1996.

[159] P Venkatesan, Soumen Das, M Krishnan, Chandan Chakraborty, Koel Chaudhury, and Mahitosh Mandal. Effect of aee788 and/or celecoxib on colon cancer cell morphology using advanced microscopic techniques. *Micron*, 41(3):247–256, 2010.

[160] Philip L Yeagle. Cholesterol and the cell membrane. *Biochimica et Biophysica Acta (BBA)-Reviews on Biomembranes*, 822(3):267–287, 1985.

[161] Fitzroy J Byfield, Helim Aranda-Espinoza, Victor G Romanenko, George H Rothblat, and Irena Levitan. Cholesterol depletion increases membrane stiffness of aortic endothelial cells. *Biophysical journal*, 87(5):3336–3343, 2004.

[162] M Sato, DP Theret, N Ohshima, RM Nerem, and LT Wheeler. Application of the micropipette technique to the measurement of cultured porcine aortic endothelial cell viscoelastic properties. *Journal of biomechanical engineering*, 112(3):263–268, 1990.

[163] Gang Zhang, Mian Long, Zhe-Zhi Wu, and Wei-Qun Yu. Mechanical properties of hepatocellular carcinoma cells. *World Journal of Gastroenterology*, 8(2):243–246, 2002.

[164] Xiaolian Xu and Erwin London. The effect of sterol structure on membrane lipid domains reveals how cholesterol can induce lipid domain formation. *Biochemistry*, 39(5):843–849, 2000.

[165] David Needham and Rashmi S Nunn. Elastic deformation and failure of lipid bilayer membranes containing cholesterol. *Biophysical journal*, 58(4):997–1009, 1990.

[166] Leann L Norman, Ratna J Oetama, Micah Dembo, F Byfield, Daniel A Hammer, Irena Levitan, and Helim Aranda-Espinoza. Modification of cellular cholesterol content affects traction force, adhesion and cell spreading. *Cellular and molecular bioengineering*, 3(2):151–162, 2010.

[167] Q. Zou and Juan Ren. Us patent: method and apparatus for nanomechanical measurement using an atomic force microscope. pending.

[168] BM. Cooke, N. Mohandas, and Coppell RL. The malaria-infected red blood cell: structural and functional changes. *Adv Parasitol*, 50:1–86., 2001.

Appendices

Appendix A

An Atomic Force Microscope Study Revealed Two Mechanisms in the Effect of Anticancer Drugs on Rate-dependent Young's Modulus of Human Prostate Cancer Cells

Abstract

Mechanical properties of cells have been recognized as a biomarker for cellular cytoskeletal organization. As chemical treatments lead to cell cytoskeletal rearrangements, thereby, modifications of cellular mechanical properties, investigating cellular mechanical property variations provides insightful knowledge to effects of chemical treatments on cancer cells. In this study, the effects of eight different anticancer drugs on the mechanical properties of human prostate cancer cell (PC-3) are investigated using a recently developed control-based nanoindentation measurement (CNM) protocol on atomic force microscope (AFM). The CNM protocol overcomes the limits of other existing methods to in-liquid nanoindentation measurement of live cells on AFM, particularly for measuring mechanical properties of live cells. The Young's modulus of PC-3 cells treated by the eight drugs was measured by varying force loading rates over three orders of magnitude, and compared to the values of the control. The results showed that the Young's modulus of the PC-3 cells increased substantially by the eight drugs tested, and became much more pronounced as the force load rate increased. Moreover, two distinct trends were clearly expressed, where under the treatment of Disulfiram, paclitaxel, and MK-2206, the exponent coefficient of the frequency-modulus function remained almost unchanged, while with Celebrex, BAY, Totamine, TPA, and Vaproic acid, the exponential rate was significantly increased.

A.1 Introduction

Mechanical properties of live cells are known to be closely related to the cells' growth stage and functionality. Changes in mechanical properties have been recognized as an indicator of pathological modifications of cells [125, 123, 126] and thereby, can serve as a biomarker for cellular phenotypic events, for example, those associated with cell adhesion and cytoskeletal organization [127, 128, 23]. In particular, as a response to the environmental and/or mechanical condition variations, cell cytoskeleton undergoes dynamical rearrangements, which, in return, further induces changes to the cellular mechanical properties [129]. Therefore, studies of mechanical properties of cells contributes to a better understanding of cells' responses to chemical treatments, including drug treatments of cancer cells. It has been reported that diseases such as cancers alter the mechanical properties of the cells [125, 112, 130], and reversely, variations of mechanical properties of cancer cell caused by anticancer drugs may be employed to evaluate the efficacy of these chemicals [131, 132]. Investigations of mechanical properties of cancer cells can further help to unravel the physical mechanisms involved in cancer development, progression and metastasis. Therefore, study of cellular mechanical properties becomes an indispensable and critical component in the development of novel strategies for cancer prevention and diagnosis.

Atomic force microscope (AFM) has become a powerful tool to study mechanical properties of single live cell owing to its unique capability in applying force stimuli and then, measuring the response at specific locations in a physiologically friendly environment with piconewton force and nanometer spatial resolutions [112, 1]. Specifically, AFM has been utilized to investigate the evolution of cell mechanical properties caused by cell abnormalities (e.g., cancers) and chemical treatments on cancerous cells [112, 129]. For example, it has been found that the Young's modulus of cancerous human epithelial cells tend to be substantially lower than normal ones [126], the Young's modulus of breast cancer cells increases monotonically with the increase of the force load rate [112], and after F-actin-disrupting drug treatment, the average elastic modulus of fibroblast cells decreased distinctly [131]. However, these studies [112, 131, 126] have been limited to measuring static cellular mechanical behavior in low frequency regions (with force load rate below 5 Hz) and small force amplitudes (below 2 nN).

The dynamic mechanical behaviors of cancer cells in higher frequency regions, and the effects of chemical treatments on the frequency-dependent viscoelastic behavior of cancer cells are largely unknown. As chemical treatments lead to dynamical rearrangements of cell cytoskeleton, and thereby, dynamic evolution of mechanical properties of cells [131, 129], evolution of dynamic mechanical behaviors of cancer cells provide insightful information to anticancer drug development.

Studies of frequency-dependent biomechanical properties of live cells have been limited by the capability of current AFM mechanical measurement techniques. Specifically, the limit arises largely due to the current method to indentation measurement on AFM, by subtracting the cantilever deflection from the cantilever base displacement [112, 105]. Significant errors and uncertainties are induced in the indentation measured as the probe acceleration (with respect to the fixed-end of the cantilever attached to the piezoelectric scanner) is ignored and the initial contact point is largely uncertain [112, 105, 133, 134]. Particularly, the probe acceleration effect is pronounced and increases substantially when the measurement frequency increases. Although the force-modulation method has been employed to measure the frequency-dependent viscoelasticity of live cells [31, 135], by augmenting a sinusoidal oscillation to the load/unload force profile of constant rate, the probe acceleration effect is completely ignored, and large uncertainties exist in the indentation measured in the relatively high frequency region [133, 136]. Moreover, such an approach is further limited by the rather small amplitude of the dynamic force applied (tens of peco newtons) applied—whereas to interrogate a variety of biological responses of the cell, excitation force of much larger amplitude needs to be applied as the mechanical properties of live cells are amplitude dependent [137, 138]. Finally, the force modulation method requires the oscillatory force to be repetitively applied at the same location at each selected measurement rate in the measured frequency range. However, for live cells such a procedure is detrimental as the repetitive, same-location force exertion tends to deform and even damage the cell membrane. It was also proposed to study mechanical characteristics of live cell by quantifying the effective stiffness using a magnetic force modulation technique on AFM [134]. Such a method, however, not only requires additional sample/ equipment preparation (e.g., use of a home-built aluminum holder with vacuum grease to mount the sample), but also does not quantify the cell stiffness (i.e., the Young's modulus) directly [134]—Quantification of

the Young's modulus requires accurate measurement of the indentation. Since the force stimuli applied and the corresponding indentation generated act as, respectively, the input and output to the cantilever probe-sample interaction model, error in indentation measurement leads directly to that in the mechanical property quantified—regardless the probe-sample interaction model employed. Thus, it is crucial to accurately measure the indentation in mechanical studies of live cell.

In this study, the effect of anticancer chemical compounds on the dynamic mechanical properties of human prostate cancer cell (PC-3) is investigated by using a newly developed control-based nanoindentation measurement (CNM) protocol [133]. Eight distinct drugs, including Disulfiram (DSF), paclitaxel (Taxol), Tomatine, BAY 11-7082 (BAY), vaproic acid (VPA), 12-O-tetradecanoylphorbol-13-acetate (TPA), Celecoxib, and MK-2206 (MK) are tested. Although studies have shown the anticancer effects of these drugs, for example, proteasome inhibition and apoptosis process of breast cancer cells induced by DSF—a well-known drug for alcoholism treatment [139], experimental examinations of these chemical compounds as anticancer drugs are ongoing, and many questions remain unanswered. Therefore, studying the dynamic mechanical property changes of PC-3 cells treated by these eight drugs may provide insightful answers to the anticancer activities of these chemical compounds.

The CNM protocol [133] overcomes the limits of existing methods for in-liquid indentation measurement of soft samples on AFM. By the CNM protocol, the indentation on the live cell is measured by tracking the *same* excitation force profile (i.e., the same cantilever deflection) on both the live cell and a hard reference, and then quantified from the displacement difference of the cantilever fixed end on these two samples. The main advantage of the CNM protocol is that by using a hard reference and more critically, accurately tracking the same force profile on both the samples, the dominant adverse effect of the cantilever acceleration is completely removed with no need for parameter calibration [133, 136]. Moreover, the hydrodynamic force effect is substantially reduced, particularly at high force load rates (e.g., reduced by over 50% when the force load rate is higher than 100 Hz). In this study, the rate dependent Young's modulus of PC-3 cells was quantified using the CNM protocol by varying the load/unload rate of the excitation force over three orders of magnitude from 0.2 Hz to 100 Hz, with the measured indentation amplitude over 2 orders larger than the oscillatory amplitude in [31].

A.2 Materials and Methods

A.2.1 Cell culture and treatment

PC-3 cells were obtained from the American Type Culture Collection (ATCC, Rockville, MD, USA), and grown in RPMI-1640 culture medium containing 10% FBS that was supplemented with penicillin (100 units/ml)-streptomycin (100 μg/ml) and L-glutamine (300 μg/ml). Cells were cultured at 37°C in a 5% CO_2 incubator and passaged twice a week. To accommodate the AFM measurements, the PC-3 cells were seeded at a density of 2.0×10^4 cells/ml in 60 mm tissue culture dishes (5 ml/dish) and incubated for 24 hpurs. Then the cells in each dish were then treated with solvent DMSO (2 μl/ml) or with each of the eight drugs dissolved in DMSO for 24 hours before the AFM measurements.

A.2.2 MTT assay

PC-3 cells were seeded at a density of 2.0 $\times 10^4$ cells/ml of medium in 96-well plates (0.2 ml/well) and incubated for 24 h. The cells were then treated with the various anticancer agents for 72 h. After treatment, 200 μl 3-[4,5-dimethylthiazol-2-yl]-2,5-diphenyl tetrazoliumbromide (5 mg/ml in PBS) was added to each well of the plate and incubated for 2 h. After careful removal of the medium, 0.1 ml DMSO was added to each well. The absorbance was recorded on a microplate reader at 540 nm. The effect of different anticancer agents on cell viability was assessed as viability percentage as compared to the DMSO-treated cells.

Immunofluorescence

Immunofluorescence staining was used to determine β-actin in PC-3 cells. Briefly, PC-3 cells were seeded at a density of 2.0 $\times 10^4$ cells/ml of medium in 60 mm culture dishes and incubated for 24 h. The cells were then treated with MK or Celebrex for 24 h. Afterwards the cells were fixed in acetone/methanol (1:1) for 10 min at room temperature and then incubated with β-actin antibody (sc-47778, Santa Cruz Biotech Inc, Dallas, TX) overnight at 4°C. Next the cells were washed and incubated with Texas Red conjugated goat anti mouse antibody (115-075-003, Jackson ImmunoRsearch Lab Inc, West Grove, PA) for 60 min at room temperature.

Immunofluorescence staining was examined using a fluorescence microscope (Nikon Eclipse TE200, Nikon Inc.).

A.2.3 Chemicals

The RPMI-1640 tissue culture medium, penicillin-streptomycin, L-glutamine and fetal bovine serum (FBS) were acquired from Gibco (Grand Island, NY). Among the eight different drugs tested in this study, Disulfiram (DSF), paclitaxel (Taxol), tomatine, BAY 11-7082 (BAY), vaproic acid (VPA), and 12-O-tetradecanoylphorbol-13-acetate (TPA) were acquired from Sigma-Aldrich (St. Louis, MO), and Celecoxib and MK-2206 (MK) were provided by the National Cancer Institute's Repository.

A.2.4 Control-based Elasticity Measurements

The recently-developed CNM protocol [133, 136, 140] was employed to measure the rate-dependent Young's modulus and frequency-dependent complex modulus of EA.hy926 cells. The central issue is to measure the indentation in the live cell accurately, particularly during high-speed and/or broadband nanomechanical measurements. Based on the analysis of the cantilever dynamics during the nanoindentation measurement, the CNM protocol obtains the indentation in the live cell, $\Delta_z(t)$, as the difference of the displacement of cantilever base (i.e., the fixed end of the cantilever) on the cell, $z_{bs}(t)$, and that on a hard reference sample (e.g., a silicon sample), $z_{bh}(t)$ [133],

$$\Delta_z(t) = z_{bs}(t) - z_{bh}(t). \tag{A.1}$$

The above indentation quantification requires that the *same* excitation force profile (i.e., the same cantilever deflection trajectory) is tracked accurately on both the samples. The readers are referred to Ref. [16] for details of the CNM protocol.

To ensure precision tracking of the same excitation force profile on both the live cell and the hard reference, the CNM protocol utilizes iterative learning control techniques, for example, the modeling-free inversion-based iterative learning control (MIIC) technique [32]. Specifically, the control input applied to drive the AFM z-axis piezo actuator is obtained through iteration

as follows:

$$\begin{aligned} u_1(j\omega) &= \alpha d_d(j\omega), \qquad\qquad k=1, \\ u_{k+1}(j\omega) &= \begin{cases} \dfrac{u_k(j\omega)}{d_k(j\omega)} d_d(j\omega), & \text{when } d_k(j\omega)\neq 0 \text{ and } d_d(j\omega)\neq 0,\ k\geq 1, \\ 0, & \text{otherwise} \end{cases} \end{aligned} \tag{A.2}$$

where'$j\omega$' denotes Fourier transform. $d_d(\cdot)$ is the desired cantilever deflection, α is a constant, and $u_k(\cdot)$ and $d_k(\cdot)$ are the current input voltage to the AFM piezo actuator and the cantilever deflection in the k^{th} iteration, respectively. The control input $u_k(t)$ is obtained by taking Fourier transform of the input and the output signals and applying the MIIC algorithm Eq. A.2, and then the inverse Fourier transform afterwards. The MIIC algorithm has also been utilized to obtain rapid broadband nanomechanical measurement on polymers in air recently [141, 142].

A.2.5 Atomic force microscope

Young's modulus of the PC-3 cells was measured in the cell culture medium using a Dimension Icon AFM (Bruker, Santa Barbara, CA) equipped with a fluid cell. A soft cantilever (MLCT-C, Bruker, USA) with nominal spring constant 0.01 N/m was chosen for the measurements. The probe radius of 28 nm and the cantilever spring constant of 0.012 N/m were calibrated, respectively, by imaging a tip-radius calibration sample (PA-01, Mikromasch, NanoAndMore USA Corp.) and the thermal tuning process. A silicon sample was chosen as the hard reference sample. Both the cells and the cantilevers were thermally equilibrated at $\sim 37^{\circ}\mathrm{C}$ for 40-60 mins prior to all measurements to minimize the cantilever drifts. All of the control and sensor signals to/and from the AFM system were acquired through a data acquisition system (NI PCI-6259, National Instruments Corporation, Austin, TX) under the Matlab xPC-target (The MathWorks, Natick, MA) environment.

A triangle drive voltage with a constant load and unload rate (as employed in usual force-distance curve measurement) was applied to the z-axis piezo actuator of the AFM system, and the following nine load rates over three orders of magnitude were applied: 0.2 Hz, 0.5 Hz, 1 Hz, 5 Hz, 10 Hz, 20 Hz, 50 Hz, and 100 Hz. The amplitude of the drive voltage was kept the same for all the above load rates, resulting in the same cantilever base displacement at 250 nm (as for the above load rates, the dynamics of neither the z-axis piezoelectric actuator nor the cantilever

fixture mechanism was excited [136]). To minimize the cell membrane damage, the triangle drive was applied for only one period when the force load rate was lower than 50 Hz and two periods at higher load rates. The drive inputs were applied successively from low to high load rates, separated by a dwelling time of 3 min between each rate—to allow the cell to fully recover from the preceding force stimuli. For each load rate, the excitation force exerted (i.e., the cantilever deflection) on the live cell was measured and regarded as the desired excitation force profile, and the MIIC algorithm was applied in the force-distance curve measurement on the reference sample to ensure precision tracking of the desired force profile (the RMS tracking error was maintained below 1.5%).

To study the effect of each drug on Young's modulus of PC-3 cells, the measurements were performed on the corresponding control first, then on the treated cells. For each drug, these measurements were repeated on five different cells for both the control and the drug treated ones.

A.2.6 Rate-dependent Elastic Modulus Quantification

At each force load rate, the Young's modulus of cell was quantified using the spherical Hertzian contact model along with the measured probe-sample interaction force and indentation [1],

$$F_z = \frac{4}{3}\frac{E\sqrt{R\Delta_z^3}}{1-\nu^2}, \tag{A.3}$$

where R is the probe radius, and E and ν are the Young's modulus and the Poisson ratio of the live cell (ν =0.5 [1, 129]), respectively. The probe-sample interaction force is quantified as $F_z = k_c d_s$ (with cantilever spring constant (k_c)) [1]. We note that other Hertizan indentation contact model such as the conical model [1] might be used. The spherical contact model is chosen as in this work the indentation depths generated were not substantially larger (over 10 times) than but tend to be comparable to the probe radius [107, 143].

A.3 Results and Discussion

The force (i.e., cantilever deflection) time profile at the load rates of 0.2 Hz and 50 Hz on TPA treated PC-3 cells at high dosage (20 μM) is shown in Fig. A.1, as an example—the force-time plots of the low dosage and/or other drugs showed similar trend. The force-indentation curves

measured from the same treatment at all nine load rates are shown in Fig. A.2 for all the nine load rates (force-indentation curves for other measurements are not shown to save sapce). The Young's modulus of the control (i.e., untreated) and the drug treated PC-3 cells are compared in Figs. A.3–A.5 for the eight tested drugs, respectively, where the Young's modulus vs. the force load rate is plotted in logarithmic scale, and the curve-fitting of the data to the following power law is also shown,

$$E = E_0 \omega^{\alpha}, \tag{A.4}$$

where E_0 is the power law constant–the elasticity scale factor of cells, and α is the power law exponent that captures the viscosity of the cell membrane [105, 110]. Moreover, E_0 and α of the fitted Young's modulus vs. frequency curve are also compared in Fig. A.6 for the eight drugs tested for the control and the treated PC-3 cells under both the low and the high dosages.

The experiment results showed that the viscoelastic behaviors of the PC-3 cells were well captured in this work. As shown in Fig. A.1(b), the probe acceleration effect on the force-indentation trajectory was pronounced and needed to be accounted for in the indentation quantification, and for the same driven amplitude, the indentation generated decreased monotonically with the increase of the force load rates (see Fig. A.2), reflecting the viscoelasticity nature of the cell membrane [1, 112]. The indentation generated on the PC-3 cells ranged from 80 nm to 230 nm among all the eight tested drugs (for all the tested dosages). As the z-axis driven driven amplitude was kept the same at 250 nm, such a variation of the indentation exactly reflected the viscoelasticity of the cells and the drug effects on it, respectively.

The measured Young's modulus vs. frequency relation followed, quite well, the power law—the widely observed universal viscoelastic behavior of live human cells [105, 110, 144]. The variations of the elasticity scale factor E_0 and the power law exponent α were small among

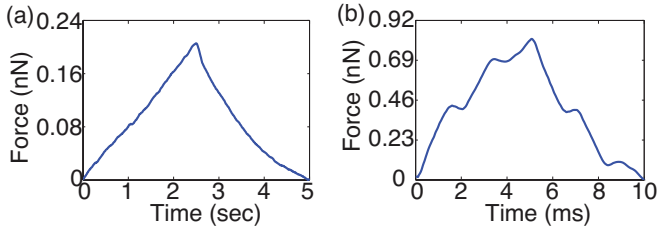

Figure A.1: Force time profile on 20 μM TPA treated cells at the load rate of (a) 0.2 Hz, and (b) 100 Hz.

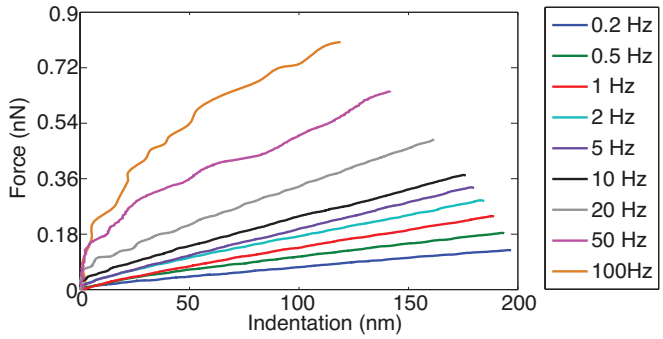

Figure A.2: Force vs. indentation curve measured on 20 μM TPA treated cells.

all the controls—with the standard deviation at 5.8% and 4.2%, respectively (see Fig. A.6), respectively. Such a small variation of E_0 and α, therefore, can be served as the baseline to examine the effects of the nine tested drugs on the mechanical properties of the PC-3 cells. Moreover, the range of the power law exponent α agrees well with the reported range (0.1–0.3) for live cells in literature [144].

As shown in Figs. A.3–A.5, all of the drug treated cells presented a much higher Young's modulus, and the higher the drug dosage was, the larger the increase of Young's modulus was. As the Young's modulus change in cells is directly related to remodeling of the cytoskeletal structure [127, 128, 131], one possible explanation of the modulus increase may be the aggregation of actin filaments under the drug effects since it has been shown that aggregation of actin filaments results in a distinct increase in the average Young's modulus of cells [131].

A quick comparison of Figs. A.3–A.5 revealed two major trends might exist in the eight test drugs effects on the Young's modulus: under the effect of DSF, MK, and Taxol, the Young's modulus of PC-3 cells was increased without significant changes in the frequency-dependence, i.e., the elasticity scale factor E_0 increased substantially (by 55% to 78%), while the power law exponent α remained almost unchanged (see Eq. A.4)—for these drugs the variation of α was only about 6% to 14%. Whereas under the effect of Celebrex, BAY, Totamine, TPA, and VPA, the frequency-dependency of the elevated Young's modulus changed significantly, i.e., E_0 increased by 78% to 260%, while α also increased by 22% to 75% (see Fig. A.6).

A.3.1 DSF, MK and Taxol: Elevated Young's Modulus without Significant Change of Frequency-dependency

For DSF, MK, and Taxol, the ratios of the Young's modulus between the treated PC-3 cells and the control were nearly the same cross all nine measured frequencies at each treatment dosage (shown as the increase of E_0, see Fig. A.3). This implies that the viscosity of the treated cells was not changed substantially compared to the control ones as the value of α didn't change substantially. It can be concluded that under the treatment of DSF, MK and Taxol, the cell cytoskeleton network reconstruction may lead to an overall stiffening of the membrane protein structure (e.g., filament shortening and thickening), but may not cause much change of degree of polymerization of actin filaments inside the cells—the general cause of viscosity change [145, 146].

Although MK, Taxol and DSF may have distinct molecular targets and mechanisms of action, the similar trend of cell Young's modulus change may explain the similarity of these three drugs' effects in cell mechanical behavior. MK can inactivate Ezrin which serves as linkers between plasma membrane and cytoskeleton [147]. Taxol interferes with normal breakdown of microtubules [148], and DSF inhibits tubulin polymerization [149]. It is reasonable to postulate that interfering with linkers between plasma membrane and cytoskeleton, interfering with microtubules breakdown and inhibiting tubulin polymerization could lead to cell stiffening without alteration of viscosity.

However, the Young's modulus increase on MK and Taxol treated cells was more significant (even for a low dosage of 2 μM) than that for DSF treated cells (at the same dose). One possible explanation may be the iron chelating effect of DSF. Earlier study showed that DSF

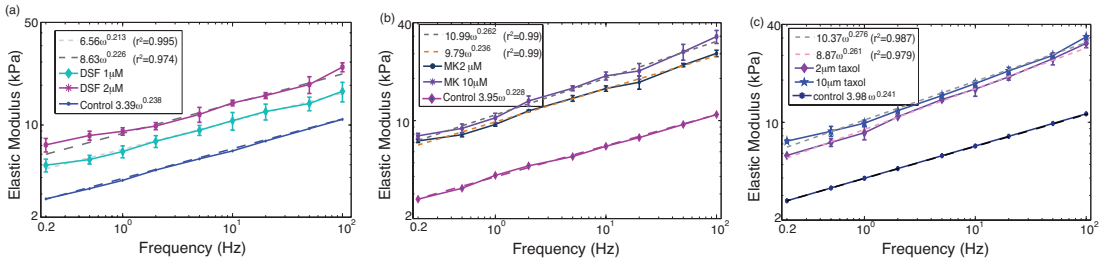

Figure A.3: Young's modulus of PC-3 cells treated by: (a) DSF, (b) MK, and (c) Taxol, respectively.

facilitated intracellular Cu uptake [150]. It was found that MK and Taxol strongly inhibited activation of Akt [151, 152] while DSF had no inhibitory effect on activation of this protein [153]. Inactivation of Akt may contribute to the stronger effect of MK and Taxol as compared to DSF. The influence of DSF on iron homeostasis may be another possible explanation for the weaker effect of DSF (on the increase in Youngs modulus) than MK and Taxol.

A.3.2 Elevated Young's Modulus Accompanied by Dramatic Frequency-dependency Change

Strikingly different from the above three drugs, the other five drugs (Celebrex, BAY, Totamine, TPA, and VPA) tended to effect not only the elastic but also the viscous behavior of the PC-3 cells as both the elasticity scale factor, E_0 and the power law exponent, α, were increased significantly. This phenomenon indicates that the cell cytoskeleton change due to the treatment of these five drugs consists not only cytoskeleton stiffening but also change of degree of polymerization, which may involve an increased concentration of actin monomers and a reorganization of actin filaments. Moreover, it is noted that the standard deviation of the Young's modulus of the PC-3 cells treated by these five drugs are larger than that of those treated by the other three drugs (DSF, Taxol and MK). Since the standard deviation of the Young's modulus for all control remains much smaller for all the eight drugs, one possible explanation for the larger deviation is that the dynamic mechanical behavior of the cells treated by the five drugs (Celebrex, BAY, Totamine, TPA, and VPA) was more active.

It was known that celebrex, TPA and valproic acid induced cell differentiation [154, 155, 156]. As studies showed that cell differentiation leads to an increase of cell rigidity [107],

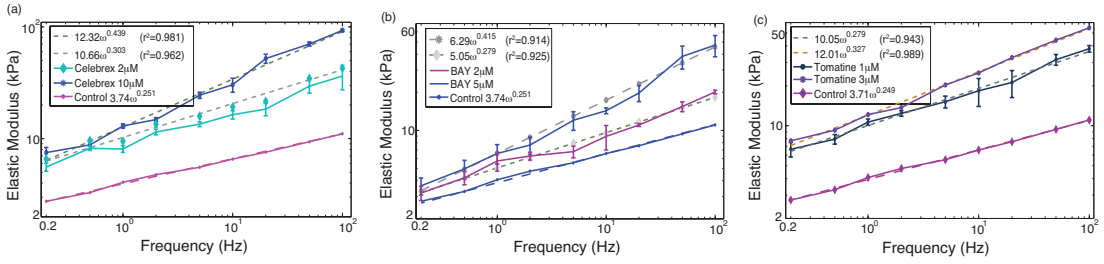

Figure A.4: Young's modulus of PC-3 cells treated by: (a) Celebrex, (b) BAY, and (c) Totamine, respectively.

increase in stiffness and viscosity of PC-3 cells treated with celebrex, TPA and valproic acid may be related to the differentiation of the cells. Although BAY11-7082 and Tomatine have not been shown to induce differentiation in epithelial cells, these drugs inhibit activation of NF-κB [157], and inhibition of NF-κB in some cells resulted in a more differentiated phenotype [158]. Thus, the effects of BAY11-7082 and Tomatine on stiffness and viscosity of PC-3 cells may relate to their inhibitory effect on activation of NF-κB.

Among the measurement results, the change of Young's modulus was most significant on the Celebrex treated cells. Since Celebrex causes loss of filopodia and lamellipodia in cells, and changes in actin network [159], these activities in addition to its differentiation inducing effects may result in a stronger effect on increasing stiffness and viscosity of PC-3 as compared to the other four drugs.

We further performed MTT test to investigate the correlation between the changes of mechanical properties and the inhibition of cell growth. As shown by the cell viability test results from the MTT assay in Fig. A.6, treatment of PC-3 cells with the eight anticancer drugs decreased the number of viable cells, particularly at high dosage, i.e., the effect was dose-dependent. Such an effect of the drugs (on decreasing cell viability) correlated well with their effect on changing the cell mechanical properties revealed in the above AFM tests, for all eight different drugs examined. Although the above AFM studies clearly revealed the two distinct patterns among the eight different drugs in changing the mechanical properties of PC-3 cells (DSF, MK and Taxol as one group, and Celebrex, Bay, Tomatine, TPA and Vaproic acid as the other group), the MTT assay failed to show any evident difference in cell viability changes

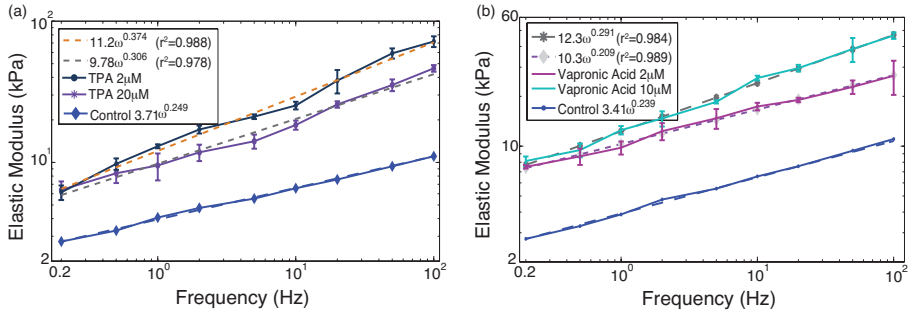

Figure A.5: Young's modulus of PC-3 cells treated by: (a) TPA, and (b) Vapronic-Acid, respectively.

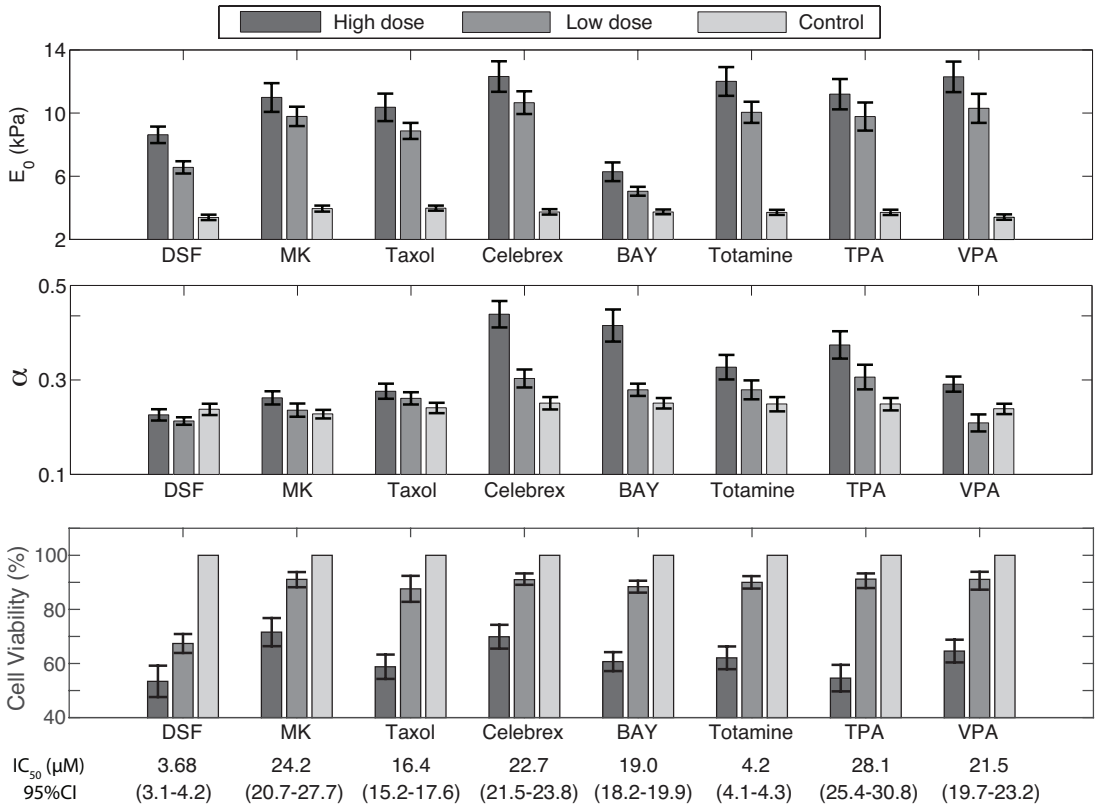

Figure A.6: Comparison of E_0 (kPa) and α in the power-law relation (Eq. A.4), and cell viability determined by the MTT assay for the eight drugs of both low and high dosages, compared to the corresponding controls.

between these two groups. This result suggests that the proposed AFM studies might have revealed new aspects of biological response of cancer cells to anticancer drug treatments, thereby, providing more information than the conventional MTT assay in responses of PC-3 cells to anticancer drug treatment. One possible explanation is that the changes in cytoskeleton and cell membrane may correlate with the ability of cancer cells to metastasize. Future studies with appropriate cancer cell metastasis model may help to explore the correlation between changes in mechanical properties and metastatic ability of cancer cells.

To further investigate the mechanisms behind the two patterns revealed by the AFM studies, immunofluorescence staining of β-actin was conducted to seek insights to the different responses in PC-3 cells to the drug treatments. MK and Celebrex were selected to represent the first and the second group of the eight drugs (as revealed by the AFM studies), respectively. The fluorescence imaging results obtained are shown in Fig. A.7. The morphology of β-actin

immunofluorescence staining was similar in cells treated with MK and those treated with Celebrex. This result suggests that the different responses in PC-3 cells to the two groups of drugs may involve more complex mechanisms in addition to the modification of the cell actin. Further studies on modification of other cytoskeleton components are needed to determine the mechanisms behind the two distinct types of response to the two groups of drugs tested.

The significance of the above studies is underscored by the importance of identifying new targets for inhibiting the growth and inducing apoptosis in cancer cells, which has become a major focus in the development of new generation of anticancer drugs. Physical properties of cancer cells such as elasticity and viscosity that associated with modification of cytoskeleton and plasma membrane may represent a unique class of novel target for development of anticancer drugs. Studies on alterations of physical properties in cancer cells treated with anticancer agents that have different mechanisms of action may provide insights to the identification of molecular targets causing lethal changes in physical properties of cells.

A.4 Conclusion

In this study, the drug effect on cancer cell nanomechanical property change was investigated using the recently proposed CNM protocol. The Young's modulus of PC-3 cells treated by eight different drugs was measured with force loading rates spanning three orders of magnitude, and compared to the values of the control. The results showed that the Young's modulus of PC-3 cells were significantly increased by the eight drugs test, and became substantially more pronounced as the force load rate increased. Moreover, two distinct trends were clearly presented, where with DSF, Taxol, and MK, the exponent coefficient of the frequency-modulus relation remained almost unchanged, while under the effect the other five drugs, the exponential rate

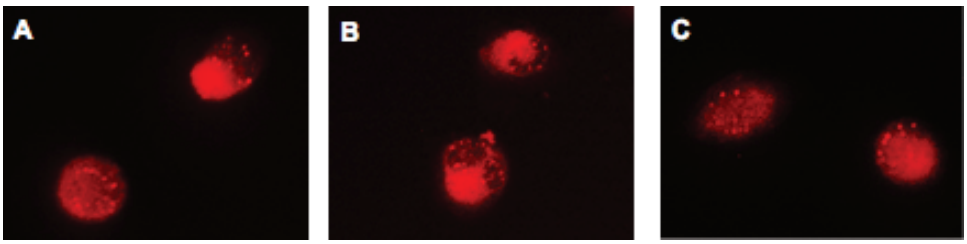

Figure A.7: Comparison of the immunofluorescence images of (a) control, (b) cells treated with MK, and (c) cells treated with Celebrex.

itself was substantially increased. These two trends pointed to the existence of two distinct mechanisms among these drugs in affecting the mechanical behavior of cancer cells, where the first group of drugs caused the cell cytoskeleton network reconstruction and might have led to the stiffening of the overall membrane protein structure (e.g., filament shortening and thickening), while the second group of drugs, in addition to causing the cytoskeleton network reconstruction, might have also changed the degree of polymerization of actin filaments inside the PC-3 cells. As a frequency-resolved Young's modulus measurement provides deep insights into the cellular dynamics in response to changes of the chemical and mechanical environment, the results presented in this study indicate that nanomechanical property changes may be used as a novel determinant for screening and developing new anticancer agents.

Appendix B

Study of Cholesterol Effect on Nanomechanical Properties of Human Umbilical Vein Endothelial Cell via Rapid Broadband Atomic Force Microscopy

Abstract

Abnormalities of blood cholesterol concentration are associated with increased risks for vascular disease, especially heart attacks and strokes. As one of the main lipid components of the plasma membrane in all mammalian cells, cholesterol has a major impact on the mechanical properties of the membrane of endothelial cells. Although the effect of cholesterol depletion on cell mechanical property alteration has been revealed, no results yet have been reported on quantitative investigation of cholesterol repletion effect. In this study, the effect of cholesterol repletion on the nanomechanical properties of human umbilical vein endothelial cell (EA.hy926) was investigated using a newly developed control-based nanoindentation measurement (CNM) protocol on atomic force microscope (AFM). By using the CNM protocol, the viscoelasticity of EA.hy926 cell was accurately measured over a large frequency range (1 Hz to 100 Hz) using both constant-rate excitation with different force load rates and a band-limited white-noise like excitation force. The viscoelasticity oscillation of the cell membranes under the cholesterol effect was also monitored in real-time. The experiment results showed that because of cholesterol repletion, the Young's modulus and the complex modulus of EA.hy926 cell were both increased over 30%. The real-time monitoring of both the Young's modulus and the complex modulus showed an oscillation period of 200 sec with varying amplitudes. Moreover, the oscillation amplitude of the cholesterol enriched cell was over 70% higher than that of the control.

B.1 Introduction

Lipid disorders—abnormalities of blood cholesterol concentration—are associated with increased risks for vascular disease, especially heart attacks and strokes. Studies of the correlation between high cholesterol level and chemical and/or mechanical properties of vascular cell provide fundamental insights to vascular disease prevention and treatment. Cholesterol is one of the main lipid components of the plasma membrane in all mammalian cells where phospholipids/cholesterol molar ratio may be as high as 1:1 [160, 161]. It is well known that mechanical properties of membrane in live cells depends strongly on submembrane cytoskeleton underlying the plasma membrane [162, 163], and changes of the cholesterol level of plasma membrane have a major impact on the submembrane cytoskeleton, and thereby, the physical properties of the cell [164, 165, 161]. The effect of cholesterol depletion on mechanical properties of endothelial cells was reported previously [161, 166]. However, due to the limitations of existing measurement techniques, the effect of cholesterol repletion was not quantitatively investigated. In this study, we investigate the effect of cholesterol repletion on the nanomechanical properties of human vein endothelial cell using a recently-developed control-based nanoindentation measurement (CNM) protocol for atomic force microscope (AFM) [133, 167].

Current studies of cholesterol effect on the mechanics aspects of endothelial cells are constrained by the limits of the measurement techniques employed. Previous studies have investigated the mechanical properties of endothelial cells with different cholesterol contents [161, 166], and it was found that cholesterol depletion may increase the stiffness of aortic endothelial cells by reducing the membrane deformability [161, 166]. However, due to the limits of the measurement techniques employed, these studies failed to detect the cholesterol repletion caused mechanical variation of cells, and more importantly, to quantify the local mechanical properties (i.e., nanomechanical properties) of the cells. Specifically, the experiments performed using micropipette aspiration [161] and traction force microscopy [166] were only capable of measuring the bulk mechanical properties of the cells. The spatial resolution of these techniques [161, 166] at μm level— comparable to the size of endothelial cells (at most tens of μm)—not only is too coarse to detect the nanomechanical properties of these cells, but also further induces substrate effect into the measured data. No results of cholesterol repletion effect

on the nanomechanical properties of endothelial cells have been reported. Such force/spatial resolution related limits can be largely alleviated via AFM technology as AFM is capable of applying force stimuli and then, measuring the response at specific locations in a physiologically friendly environment with piconewton force and nanometer spatial resolutions [112, 114, 168].

In this study, a newly developed control-based nanoindentation measurement (CNM) protocol [133, 167] on AFM is utilized to investigate the effect of cholesterol repletion on the nanomechanical properties of human umbilical vein endothelial cell (EA.hy926). The CNM protocol [133] overcomes the limits of existing methods for in-liquid indentation measurement of soft samples on AFM, as currently measurements of frequency-dependent biomechanical properties of live cells are rather erroneous and prone to measurement uncertainties, particularly when the measurement frequency range and excitation force amplitude increase. In these measurements [1, 31], the probe acceleration (with respect to the fixed-end of the cantilever) is ignored and the initial contact point can be largely uncertain [1, 133], whereas the probe acceleration is pronounced and becomes the dominant adverse effect when the measurement frequency increases [133]. The CNM protocol removes the cantilever acceleration effect without complicated parameter calibrations, and substantially reduces the hydrodynamic force effect involved, even when the force amplitude and the measurement frequency range become large (broadband) [133]. Therefore, the CNM protocol can be a powerful tool to study the cholesterol effect on nanomechanical properties of cells.

In this work, the Young's modulus and complex modulus of cholesterol enriched EA.hy926 cell were quantified and real-time monitored using the CNM protocol. The rate-dependent Young's modulus was quantified by varying the load/unload rate of a triangle excitation from 0.1 Hz to 20 Hz, and real-time monitored by continuously repeating such a force-curve measurement at the load rate of 1 Hz for 800 sec. A twenty-second long broadband excitation with frequencies ranging from 2 Hz to 100 Hz was applied to measure the complex modulus of the cells, and then continuously repeated 60 times to monitor the viscoelasticity oscillation in real-time. The experimental results showed that cholesterol repletion increased the Young's modulus and the complex modulus of EA.hy926 cell over 30%. Real-time monitoring of the Young's modulus and complex modulus showed that both the elasticity and viscosity measured presented a periodic oscillation with the period around 200 sec and varying amplitudes.

With the cholesterol treatment, the oscillation amplitudes of both the elasticity and the viscosity were increased over 70%. These results revealed that cholesterol repletion may reinforce the coupling of F-actin to the plasma membrane by increasing actin stability, and cholesterol might have modified the submembrane cytoskeletal organization of EA.hy926 cell by causing involvement of the motor protein nonmuscle myosin II.

B.2 Materials and Methods

B.2.1 Cell culture and treatment

Human umbilical vein endothelial (EA.hy926) cells were maintained in RPMI culture medium containing 10% FBS that was supplemented with penicillin (100 units/ml)-streptomycin (100 μg/ml) and L-glutamine (300 μg/ml). Cultured cells were grown at $37^{\circ}\mathrm{C}$ in a humidified atmosphere of 5% CO_2 and were passaged twice a week. To accommodate the AFM measurements, the EA.hy926 cells were seeded at a density of 0.2×10^5 cells/ml in 60 mm tissue culture dishes (5 ml/dish) and incubated for 24 h to allow the cells to attach to the dishes (day 0). The cells were then treated with cholesterol at day 0, 2 and 4. At day 5, the cells were subjected for AFM experiments.

B.2.2 Chemicals

EA.hy926 cells were obtained from the American Type Culture Collection (ATCC, Rockville, MD, USA). Cholesterol was purchased from Sigma-Aldrich (St. Louis, MO). RPMI-1640 tissue culture medium, penicillin-streptomycin, L-glutamine and fetal bovine serum (FBS) were from Gibco (Grand Island, NY).

B.2.3 Control-based Nanomechnical Property Measurements

The recently-developed CNM protocol [133, 136, 140, 167] was employed to measure the rate-dependent Young's modulus and frequency-dependent complex modulus of EA.hy926 cells. The central issue is to accurately measure the indentation in the live cell, particularly, during high-speed and/or broadband nanomechanical measurements. Based on the analysis of the cantilever dynamics during the nanoindentation measurement, the CNM protocol obtains the

indentation in the live cell, $\Delta_z(t)$, as the difference of the displacement of the cantilever base (i.e., the fixed end of the cantilever) on the cell, $z_{bs}(t)$, and that on a hard reference sample (e.g., a silicon sample), $z_{bh}(t)$,

$$\Delta_z(t) = z_{bs}(t) - z_{bh}(t), \tag{B.1}$$

under the condition that the *same* excitation force profile (i.e., the same cantilever deflection trajectory) is tracked accurately on both the samples. See a brief description of the CNM protocol in **Chapter 5** for details.

To ensure precision tracking of the same excitation force profile on both the live cell and the hard reference, the CNM protocol utilizes iterative learning control techniques, for example, the modeling-free inversion-based iterative learning control (MIIC) technique [32]. Specifically, the control input applied to drive the AFM z-axis piezo actuator is obtained through iterations as follow,

$$\begin{aligned} u_1(j\omega) &= \alpha d_d(j\omega), \qquad\qquad k = 1, \\ u_{k+1}(j\omega) &= \begin{cases} \dfrac{u_k(j\omega)}{d_k(j\omega)} d_d(j\omega), & \text{when } d_k(j\omega) \neq 0 \text{ and } d_d(j\omega) \neq 0,\ k \geq 1, \\ 0, & \text{otherwise} \end{cases} \end{aligned} \tag{B.2}$$

where'$j\omega$' denotes the Fourier transform, $d_d(\cdot)$ is the desired cantilever deflection, α is a constant, and $u_k(\cdot)$ and $d_k(\cdot)$ are the input voltage applied to the AFM piezo actuator and the cantilever deflection measured in the k^{th} iteration, respectively. Note the control input $u_k(t)$ is obtained by taking the Fourier transform of the input and the output signals and applying the MIIC algorithm Eq. B.2, and then the inverse Fourier transform afterwards. The MIIC algorithm has also been utilized to obtain rapid broadband nanomechanical measurement on polymers in air recently [141, 142]. In this experiment, to minimize the deformation of the cell membrane, the excitation force exerted (i.e., the cantilever deflection) on the live cell was measured and regarded as the desired excitation force profile to be tracked on the hard reference. Then the MIIC algorithm was applied to track such a desired excitation force profile on the reference sample.

B.2.4 Nanomechanical Property Quantification

Based on the above measured indentation, $\Delta_z(t)$, the Young's modulus of the cells for constant force load rate is quantified using Hertz contact model [1, 129],

$$F_z = \frac{4}{3}\frac{E\sqrt{R\Delta_z^3}}{1-\nu^2}, \tag{B.3}$$

where R is the probe radius, and E and ν are the Young's modulus and the Poisson ratio of the live cell (ν =0.5 [1, 129]), respectively. The probe-sample interaction force is quantified as $F_z = k_{eqv}d_s$ (with cantilever deflection (d_s)) [1].

When an oscillatory excitation force load is applied, the complex modulus $E^*(j\omega)$ of EA.hy926 cells is quantifies using the applied force and the indentation measured as [91, 92]

$$E^*(j\omega) = \frac{(1-\nu^2)F_z(j\omega)}{2R\Delta_z(j\omega)}. \tag{B.4}$$

We note that other contact mechanics models [1, 129] have been proposed recently for cell mechanics measurement. The use of the above CNM method can be equally applied along with these contact mechanics model as well.

Atomic force microscope

The modulus of the EA.hy926 cells was measured in the cell culture medium using a Dimension Icon AFM (Bruker, Santa Barbara, CA) equipped with a fluid cell. A soft cantilever (MLCT-C, Bruker, USA) with nominal spring constant 0.01 N/m was chosen for the measurements. The probe radius of 28 nm and the cantilever spring constant of 0.012 N/m were calibrated through imaging a tip-radius calibration sample and the thermal tuning process, respectively. A silicon sample was chosen as the hard reference sample. The AFM system was thermally equilibrated at $\sim 37^{\circ}\mathrm{C}$ for 40-60 mins prior to all measurements to minimize the cantilever drift.

To measure the rate-dependent Young's modulus, triangle voltage profiles were applied to the z-axis piezo actuator of the AFM system, and eight different force load rates were tested: 0.1 Hz, 0.2 Hz, 0.5 Hz, 1 Hz, 2 Hz, 5 Hz, 10 Hz, and 20 Hz. The drive inputs were applied successively from low to high rates, separated by a dwelling time of 3 min—to allow the cell to fully recover from the preceding force stimuli. The measurements were repeatedly performed on five difference cells of the control first, then on five treated cells. Furthermore, to monitor

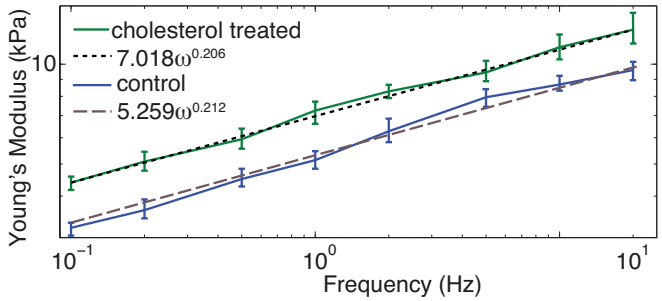

Figure B.1: Frequency-dependent Young's modulus of cholesterol treated EA.hy926 cell and control.

the Young's modulus oscillation of both the treated cells and the control, the triangle force profile was continuously collected 800 sec continuously when the force load rate was set at 1 Hz.

To measure the complex modulus, a band-limited white-noise-like (frequency range: 2 Hz to 100 Hz) excitation force of 20 sec was applied to measure the complex modulus of the cells. The measurement was repeated sixty times continuously to measure the oscillations of the viscoelasticity of the cell membranes in real-time.

In the above experiments, the excitation force profile (i.e., the cantilever deflection) measured on the cell was treated as the desired force profile to be tracked on the silicon sample, and then the MIIC algorithm was applied to achieve precision tracking of such an excitation force trajectory, with the RMS tracking below 1.5%.

B.3 Results and Discussion

B.3.1 Rate-dependent Young's modulus

The Young's modulus of the control (i.e., untreated) and the cholesterol treated EA.hy926 cells is compared in Fig. B.1, where the Young's modulus vs. the force load rate is plotted in logarithmic scale, and the curve-fitting of the data to the following power law is also shown,

$$E = E_0 \omega^{\alpha}, \tag{B.5}$$

where E_0 is the power law constant that characterizes the elasticity scale factor of cells, and α is the power law exponent that captures the viscosity of the cell membrane [105, 110].

The experimental results showed that the measured Young's modulus vs. frequency relation of both the treated cells and the control followed the power law—the widely recognized

"universal" viscoelastic behavior of live human cells [105, 110]. The results shown in Fig. B.1 suggest that the viscoelastic behavior of the treated cells and the control are quite similar as the power law exponent α remained almost unchanged (the difference was around 3%). Such a similarity indicates that the cholesterol repletion in human umbilical vein endothelial cell does not initiate actin polymerization as it is known that actin polymerization changes cell viscoelastic behavior by creating more F-actin fibers [161, 146]. This observation agrees with the previous study that cholesterol repletion had no effect on the intensity of F-actin-specific staining or F-actin cellular distribution [161]. However, unlike the previous studies that failed to observe any changes of Young's modulus in cholesterol enriched cells [161, 166], the results in Fig. B.1 also clearly show a significant increase of the elasticity scale factor E_0 under cholesterol repletion—E_0 of the treated cells was increased substantially by 33.5%. The increase in E_0 might be caused by alterations of the integrity of plasma membrane due to cholesterol repletion. One possible explanation is that the cholesterol repletion may reinforce the coupling of F-actin to the plasma membrane by increasing actin stability. This observation–cholesterol repletion causes Young's modulus increase of the human umbilical cord vein endothelial cell–provides new insights to how cholesterol alters endothelial cell behaviors.

B.3.2 Real-time monitoring of Young's modulus

Real-time monitoring of the Young's modulus of the cells measured with a triangle excitation force profile at the rate of 1 Hz for 800 sec is presented in Fig. B.2. Agreeing with Fig. B.1, the continous monitoring of the Young's modulus shows that the averaged Young's modulus (over the whole 800 sec measurement) of the cholesterol treated cells was over 39% higher than that of the control (compared to a 36.5% increase in Fig. B.1 at 1Hz). Furthermore, the oscillatory behavior of the elasticity was evident for both the treated cells and the control, with a rather consistent period around 200 sec (see Fig. B.2)—measured by the period between two successive major peaks. The 200 sec oscillation period is close to the previous results measured on bronchial epithelial cells [129]. Moreover, the amplitude of the Young's modulus oscillation varied and became much more so after the cholesterol treatment (see Fig. B.2), the peak-to peak variation of the oscillation amplitude was increased over 70%. As previous studies have shown that the elasticity oscillation of endothelial cells is closely related to myosin activity

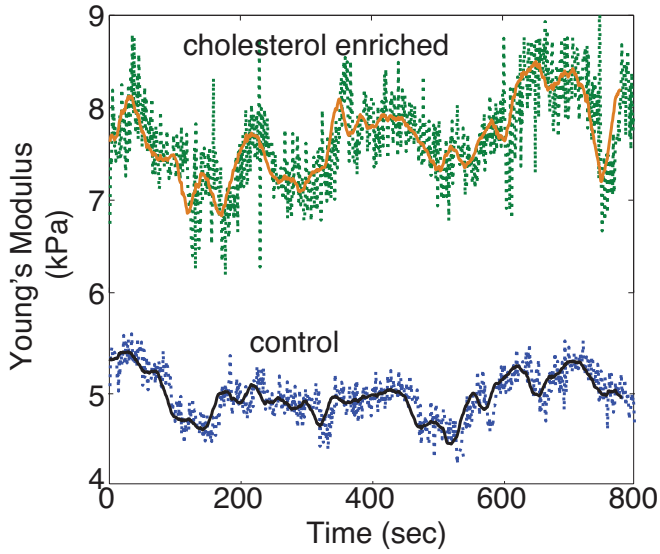

Figure B.2: Real-time monitoring of the Young's modulus of the cholesterol treated EA.hy926 cell with force load rate at 1 Hz for 800 sec. Adjacent-averaging with a 20-points window (the solid line) is shown to highlight periodic elasticity oscillations.

[129], such a large elasticity oscillations suggests that cholesterol might have modified the submembrane cytoskeletal organization of EA.hy926 cell by causing involvement of the motor protein nonmuscle myosin II.

B.3.3 Real-time monitoring of complex modulus

Real-time monitoring of the complex modulus (the magnitude of the complex modulus) shown in Fig. B.3 combines the findings in both Figs. B.1 and B.2—the power law relation and elasticity oscillation, respectively. In particular, the complex modulus of the cells during each broadband measurement followed the power law, and the averaged power law exponents were close to the results in Fig. B.1—0.197 vs. 0.206 for cholesterol treated cell, and 0.208 vs. 0.212 for control, respectively. Also, at the same frequency, the complex modulus of cholesterol treated cell was 37.4% higher than that of control—compared with 33.5% increase in Fig. B.1. Furthermore, Fig. B.3 also presents the viscosity oscillation of EA.hy926 cell as the real-time oscillation of the power law exponent, α was monitored by repetitively applying the frequency-rich excitation force (the broadband signal), and α varied from 0.168 to 0.267 for the cholesterol treated cell and 0.187 to 0.231 for control, respectively (as shown in Fig. B.4). The complex modulus in Fig. B.3 showed an oscillation period about 200 sec, and the oscillation

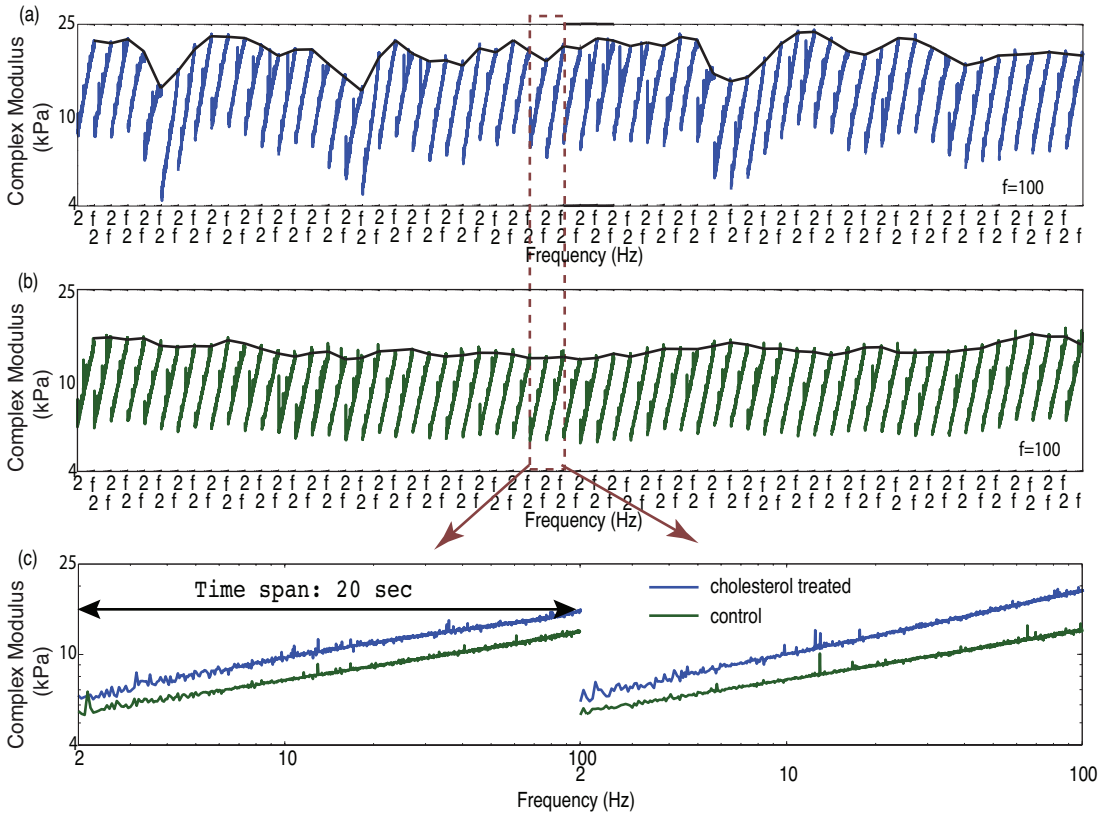

Figure B.3: Real-time monitoring of complex modulus of cholesterol treated EA.hy926 cell and control for 1200 sec (by consecutively applying 20 sec long broadband excitation (with frequency range 2–100 Hz) 60 times): (a) real-time monitoring of complex modulus of cholesterol treated EA.hy926 cell; (b) real-time monitoring of complex modulus of control; (c) zoomed-in view of two consecutive broadband measurements on the cholesterol treated cells and the control.

amplitude was inconsistent for neither the cholesterol treated cell, nor the control. However, it was quite clear that the oscillation amplitude of the cholesterol treated cell was at least 80% higher than that of the control—this also agrees with the result presented in Fig. B.2. It is noteworthy that the CNM is the only technique reported which is able to provide results on real-time monitoring of the viscoelastic behavior of live cells.

B.4 Conclusion

In this study, the effect of cholesterol repletion on nanomechanical property change of human umbilical cord vein endothelial cell was invested using the recently proposed CNM protocol on AFM. The Young's modulus of cholesterol enriched EA.hy926 cell was measured at eight

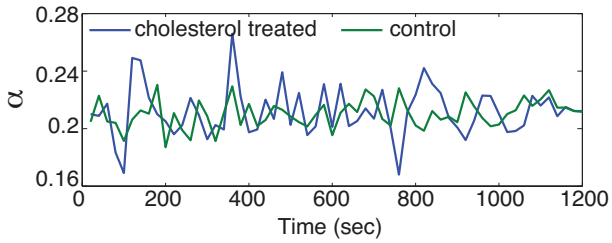

Figure B.4: Oscillation of the power exponent α.

different force loading rates, and monitored in real-time for 800 sec. The Young's modulus of cholesterol enriched cell was significantly increased, and the real-time monitored Young's modulus oscillation was more pronounced under the cholesterol repletion effect. The results reveal that cholesterol repletion may increase the Young's modulus of EA.hy926 cell by altering the integrity of plasma membrane, and intensifies the viscoelastisity oscillation amplitude without altering the oscillation period through affecting myosin activity of the cell. The real-time monitoring complex modulus of cholesterol treated cells presented the similar trends of increases. It is noteworthy that the real-time monitoring of the viscoelastic behavior of EA.hy926 cell can only be achieved using the CNM protocol, and it provides more insights on how cholesterol repletion affects the nanomechanical behavior of endothelial cells.